3-2006

Passive Ranging Using Atmospheric Oxygen Absorption Spectra

Michael R. Hawks

www.manaraa.com

Passive Ranging Using Atmospheric Oxygen Absorption Spectra

DISSERTATION

Michael R. Hawks, Major, USAF

AFIT/DS/ENP/06-02

DEPARTMENT OF THE AIR FORCE
AIR UNIVERSITY

AIR FORCE INSTITUTE OF TECHNOLOGY

Wright-Patterson Air Force Base, Ohio

The views expressed in this dissertation are those of the author and do not reflect the official policy or position of the United States Air Force, Department of Defense, or the United States Government.

AFIT/DS/ENP/06-02

Passive Ranging Using Atmospheric Oxygen Absorption Spectra

DISSERTATION

Presented to the Faculty

Graduate School of Engineering and Management

Air Force Institute of Technology

Air University

Air Education and Training Command

In Partial Fulfillment of the Requirements for the

Degree of Doctor of Philosophy

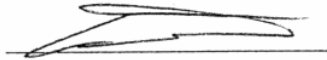Michael R. Hawks, B.S., M.S.

Major, USAF

January, 2006

APPROVED FOR PUBLIC RELEASE; DISTRIBUTION UNLIMITED

PASSIVE RANGING USING ATMOSPHERIC OXYGEN ABSORPTION SPECTRA

Michael R. Hawks, B.S., M.S.

Major, USAF
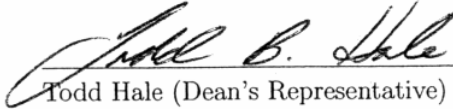
Approved: Date:
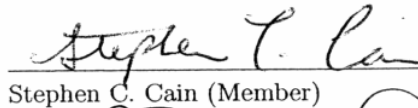
_____   26 Jan 06

Glen P. Perram (Chairman)

_____   1 FEB 06

Todd Hale (Dean's Representative)

_____   26 Jan 06

Stephen C. Cain (Member)

_____   25 Jan 06

Michael A. Marciniak (Member)

_____   25 JAN 06

Ronald F. Tuttle (Member)

_____   26 Jan 06

Edward A. Watson (Member)

Accepted:

_____   10 Feb 06

M. U. Thomas   Date

Dean, Graduate School of Engineering and Management

Abstract

The depth of absorption bands in observed spectra of distant, bright sources can be used to estimate range to the source. Previous efforts in this area have relied on measuring infrared CO_2 bands, with disappointing results. A novel approac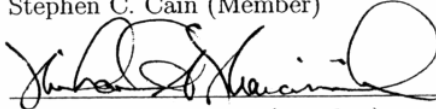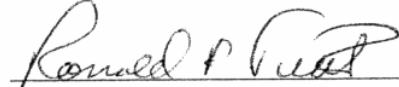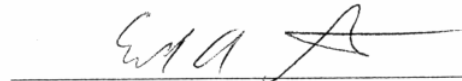h is presented here and demonstrated using observations of the O_2 absorption band near 762 nm. Oxygen was chosen because its concentration is more stable and predictable than CO_2 or H_2O, and this band is spectrally isolated from other atmospheric bands, which enables direct estimation of absorption.

Range is estimated by comparing observed values of band-average absorption, $\bar{A}$, against curves derived from either historical data or model predictions. Curves are based on fitting a random band model to the data, which reduces average range error by 67% compared to the Beer's Law model used in previous work. An original model is presented based on a traditional random band model, modified to account for variations in absorber concentration over long, inhomogeneous paths. This modification further reduces error by over 50% in short-range experiments, and can be used in conjunction with any band model.

A static rocket motor test was observed using a Bomem MR-254 Fourier transform spectrometer at a range of 2.8 km. In this case, observed values of $\bar{A}$ were compared against data simulated using FASCODE, a validated atmospheric transport model. Detailed atmospheric soundings were not required; a standard atmosphere was used, and a simple correction, based on published meteorology data, is presented. The resulting range estimate was accurate to within 0.5% (14 m). Similar accuracy was also achieved at shorter ranges using a lamp as a surrogate target.

Long-range performance is predicted by using FASCODE and theoretical models to extrapolate observed short-range performance. Range error of 5% or less is predicted at ranges up to 400 km for a representative target.

Acknowledgements

This research could never have taken place without the advice, support and assistance of a huge number of people, all of whom I cannot possibly list here.

Everyone thanks their family, advisor and sponsor ... and I will too. My family has endured a lot during the last few months of this program, and I am deeply grateful for their patience. I would also like to thank Dr. Perram and my entire committee for their advice and patience, and John Florio (NASIC/DEM) for sponsorship, ideas, and boundless enthusiasm.

There are many more people whose help I would like to specifically acknowledge: Tom Smith, 2Lt Jim Parker, Jamie Malak and all the other *great* people in the Propulsion Directorate of AFRL for making the field experiment happen; AFIT technicians Greg Smith and Mike Rant for doing their *almost* thankless jobs so well; Marken Houle for always finding the answers to the great bureaucratic mysteries of life; Gordon Scriven and Nahum Gat (OKSI), the developers of AD-MODTRAN; Jim Chetwynd (AFRL/VS) and Gail Anderson (NOAA) for their help learning about atmospheric transport; Lt Col Stephen Fiorino (AFIT) for teaching me everything in Appendix B; and the Vance's, my "adopted" family.

Table of Contents

List of Figures

List of Tables

List of Symbols

List of Abbreviations

Passive Ranging Using Atmospheric Oxygen Absorption Spectra

I.   Introduction

There are many surveillance, targeting and tracking applications where range information is necessary or desirable. Traditional ranging sensors rely on active emission of acoustic or electromagnetic radiation, but present Air Force operations are becoming increasingly reliant on stealth. Passive sensors are not only covert, but often are smaller, cheaper, and easier to integrate onto aircraft than active systems.

For example, passive sensors typically require much less prime power from the vehicle, making them desirable for use on small unmanned aerial vehicles (UAV). A ranging sensor could be employed on a UAV for target tracking and designation or to pinpoint the location of a missile launch or bomb impact.

Range sensors could also be used on manned aircraft as part of an integrated defensive system. Several existing countermeasure options would be more effective given the ability to employ them at the right time during the engagement. Even a crude ranging sensor would be accurate enough to enable such a system. To date this technique has never been employed operationally because active ranging systems require emission (incompatible with low-observable aircraft) as well as some form of beam pointing/steering device. Beam directors will increase drag, radar cross-section or cost compared to passive sensors that can be integrated behind a conformal window.

The most significant advantage of a passive sensor is in its inherent covertness. Any active sensor runs the risk of alerting the target or enemy air defenses, increasing risk and degrading mission effectiveness.

Of these applications, the one of primary focus in this project is ballistic missile tracking. This mission was chosen not only for its military significance, but also

1

because it is one of the most technically stressing applications. An airborne missile-tracking sensor might regularly be required to operate at ranges over 100 km at angles near horizontal (and through the most dense portion of the atmosphere). Range estimation of boost-phase theater ballistic missiles (TBM) would enable rapid launch point location to find and target mobile launchers.

One example application for TBM tracking is the Airborne Laser (ABL) program. The ABL must find, fix, track and target the missile during boost-phase. While ABL is hardly covert, passive sensors still offer some benefits. For example, most types of passive sensor would be simpler to integrate on the airframe and into the fire control system than an active sensor. Many scenarios presented here are chosen to resemble ABL-like missions.

1.1 Related Work

Several approaches to passive ranging have been previously attempted, but few are suited to the demands of a ballistic missile tracking mission.

Many, such as image growth [4], wavefront curvature sensing [15], and binocular imaging [25], are intended for short ranges applications such as autonomous navigation. There are many different algorithms [6, 26, 38] to infer range from angle rates in optical, radar or acoustic receivers. These methods typically require some *a priori* knowledge of target motion (such as direction, velocity or acceleration) and will generally be unsuitable unless used in conjunction with other techniques. Triangulation shows potential for longer ranges if the application allows placement of two or more sensors in optimal locations [34], which is a significant challenge for an airborne sensor platform.

1.1.1 Differential Absorption. Range estimates based on atmospheric absorption offer numerous advantages over other techniques, particularly at long ranges. First, they do not rely on any image information, so can be used against distant point sources as well as closer objects. They can operate on stationary or moving platforms,

2

without requiring any advanced knowledge of target motion. Absorption-based techniques require an emissive target, so are well suited to tracking boost-phase missiles.

The majority of past work in this area focused on using differential absorption (comparing the absorption in two or more frequency bands), primarily in the Mid-Wave Infrared (MWIR, or 2-5 μm region). The first published experimental work in this area was conducted by Leonpacher [29] at AFIT. Rather than truly estimating range, this research treated ranging as a classification problem and attempted only to classify range into one of a few discrete range bins. The bands tested experimentally were optimized for short range experiments (up to 5 km), and are unsuited to TBM tracking.

1.1.2 Monocular Passive Ranging. The largest research program to use differential absorption for ranging is known as Monocular Passive Ranging (MPR), developed by Draper, *et al.* [8, 9, 23, 30–32]. The MPR program used MWIR filters at various frequencies within the CO_2 band. Section 2.6 will analyze the details of the MPR technique, but the basic concept relied on solving Beer's Law for range. The ratio of the observed intensities at two different frequencies, according to their theory, should be exponential with range. There is also a proportionality constant that depends on the source spectrum and other losses (primarily aerosol scattering). These factors can be estimated in modelling, but during field experiments they are unknowns that introduce error in the range estimate. Actual field test performance was disappointing.

Other groups have also looked at differential absorption in the CO_2 band for ranging [19, 39], and some have even discussed the O_2 band presented here [20]. To date, however, none of the published work goes beyond a conceptual discussion of differential absorption.

1.1.3 Advanced MPR. Also worth noting is Advanced MPR [13], developed by OptoKnowledge Systems Inc (OKSI). Validated atmospheric transport codes such as MODTRAN can accurately predict the transmission for any given scenario. The

3

basis for Advanced MPR (or AMPR) is to iteratively apply MODTRAN until the spectrum predicted by the code matches the observations. The model inputs (including range) are then assumed to represent the physical situation. AMPR finds the set of inputs with the least error by using a sophisticated optimization scheme based on use of Automatic Differentiation MODTRAN (AD-MODTRAN). This program computes analytic derivatives of output variables (spectra) with respect to user-selected input variables. AMPR has one immediate advantage over other approaches in that it makes use of the entire spectrum rather than just two points.

While this method is both sophisticated and powerful, one must be careful to properly constrain the optimization. The software will find an optimal solution, but there are multiple combinations of input factors for which the output differs by less than the measurement error. When used improperly, the solution with the least error may not be the one that best describes the physical reality. OKSI is developing techniques to intelligently constrain the problem using Bayesian estimation. Until this approach can be thoroughly field tested, it may be wise to consider alternate approaches. Although this technique is applicable to any spectral band and resolution, the only funded tests to date all rely on the same MWIR filter bands selected for MPR.

1.1.4 Differential Refraction.   One other interesting approach is a technique called REDAR (Range Estimation by Differential Atmospheric Refraction), developed by Gibson [14], now at the Johns Hopkins University Applied Physics Lab. While not based on absorption, this method shares all the advantages described above for differential absorption techniques.

The vertical density gradient of the atmosphere causes a similar gradient in index of refraction that acts like a lens and refracts light as it travels near the Earth. In addition, the index is frequency dependent, causing the higher frequencies to be refracted more than lower ones. The result is a spreading of light from a point-like source into a vertical spectrum. If light from a distant source is observed through

4

two or more filters, the separation between the resulting points at the detector is proportional to range.

This separation between points will generally be quite small, so the precision required to make these measurements can be a technical challenge. The requirements are less demanding at longer ranges and lower altitudes (where the dispersion is greater). Absorption-based techniques, on the other hand, will suffer more from noise at long ranges (because the nature of this approach requires observations in an absorption band, where signal is lower). A combination of both methods may be advised.

1.2 Present Work

The work presented here further explores the possibility of absorption-based techniques, similar to MPR. Rather than MWIR bands, however, this work examines the utility of the near infrared (NIR) absorption band of molecular oxygen. This band offers several advantages over those chosen in previous MPR work (or any other MWIR absorber).

1. Oxygen is mixed more uniformly in the atmosphere and is less dependent on weather conditions than CO_2 [24].

2. The rotational structure of the transition is relatively easy to resolve compared to other molecular bands. The relative strengths of the individual rotational lines can be used to estimate air temperature, which can in turn be used to refine range estimates.

3. The O_2 band of choice around 762 nm is easily measured with non-cryogenic detectors, making integration onto a tactical aircraft more feasible.

4. There are no other absorption bands in this spectral region. This spectral isolation enables direct estimation of transmission (as will be demonstrated below).

5

5. Rocket exhaust plumes can contain hot CO_2 or H_2O, which will emit in the band and complicate estimates of absorption. Unburned O_2, on the other hand, is very uncommon in exhaust plumes.

6. This band is associated with a very weak transition, so it will not saturate (*i.e.* absorb all light in the band) even at ranges of several hundred of km.

7. There is also a second band around 690 nm that is even weaker and could be used if saturation does become an issue, or simply as an additional estimate (to reduce error).

While the thermal emission from hot sources will be brighter in the MWIR than this NIR band, the above advantages may allow for more accurate range estimation in spite of the weaker signal.

In addition to the choice of bands, this project also develops different techniques to estimate range from the spectra. First, this work explores the advantages of high spectral resolution measurements. Also, previous works on differential absorption all relied on Beer's Law as a basis for estimating range. To more appropriately characterize actual observations (which will always be made over some finite bandwidth), the present work makes use of existing band models [17] that are the core of complex atmospheric transport codes such as MODTRAN.

1.3   Summary

The real problem is not whether range can be estimated from observations. The question is *how accurately* it can be done. The answer will depend on many factors. The observed spectrum will depend on the source properties, as well as the temperature, pressure, concentration and aerosol content of the intervening air. The task is to find a method for dealing with this complexity. This is done in several steps. First, Chapter II hypothesizes a technique, based on band-average absorption and band models, that will, theoretically, be insensitive to most of these factors. Second, Chapter IV develops the appropriate form of the band model, based on a combination of established models and a novel modification for inhomogeneous paths.

6

Third, Chapter V uses short range experiments to verify the technique and establish performance bounds. Finally, Chapter VI uses analytic derivatives of this band model as a basis to predict accuracy at long ranges. In so doing, this paper will demonstrate a new range estimation technique and show that it provides a significant improvement in range accuracy compared to previous methods.

II. Theory

Electromagnetic waves are always perturbed by propagation through the atmosphere. The degree by which the signal is changed is proportional to the range from target to sensor. In typical detection problems, this is a nuisance that complicates the estimation of the original signal. In the proposed experiment, however, the amount by which the signal is changed will be used to deduce the range. This approach requires some *a priori* knowledge of the original signal (before propagation through the atmosphere) in order to find the changes in that signal. This project focuses on self-emission from hot sources where the source spectrum can be assumed to approximate a Plankian distribution. In practice, any broadband emitter (or more specifically, an emitter whose spectrum is slowly varying in the region of the absorption band of interest) will suffice.

There are numerous effects which alter the signal as it propagates. For spectroscopic measurements, the most significant factors are absorption and scattering. Absorption is a strong function of wavelength; it is dominant when the photon energy is near resonance with an atomic or molecular transition. Scattering, on the other hand, is a weak function of wavelength over the bandwidths of interest. This chapter, therefore, focuses primarily on the molecular absorption. Sections 2.1-2.3 present a review of the general physics that determines the absorption spectrum. Section 2.4 addresses the issues particular to estimating range from absorption measurements. Section 2.5 reviews the theory of band models. Finally, section 2.6 analyzes the differences between the present work and MPR.

2.1 O_2 X→b Spectrum

Figure 2.1 shows the potential energy curves for the ground $(^3\Sigma_g^-)$ and 2nd excited $(^1\Sigma_g^+)$ electronic states of molecular oxygen, commonly designated X and b, respectively. Both electronic states dissociate to two ground state oxygen atoms. Absorption of photons with wavelengths near 762 nm results in transition between the lowest vibrational levels of the two electronic states, or $X(v''=0) \rightarrow b(v'=0)$.

8
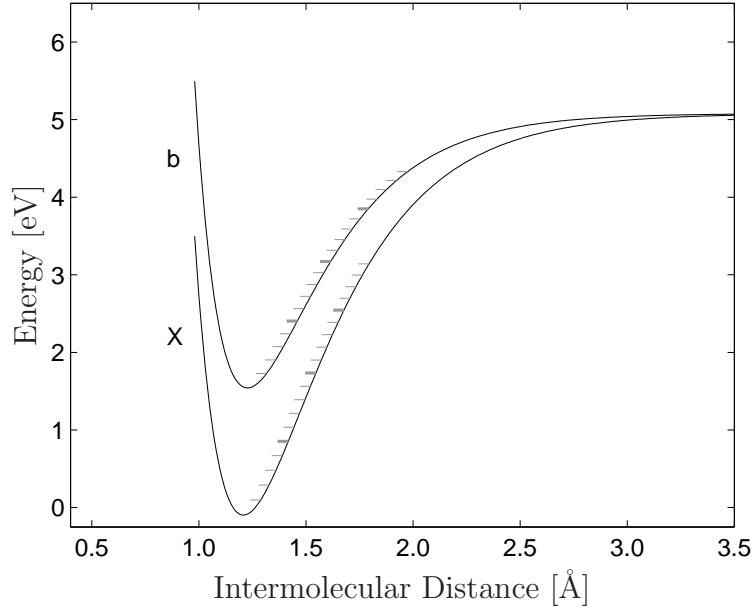
Figure 2.1: O_2 potential energy curves for the X and b electronic states. Horizontal lines indicate the vibrational levels [21].

The two potential energy curves exhibit a very small shift in equilibrium internuclear separation, establishing a strong preference for $\Delta v = 0$ transitions. The $v'' = 0 \to v' = 1$ band around 690 nm is also observed in the data, although it is much weaker.

By normal electric dipole selection rules, a transition from triplet to singlet states is forbidden, as is the transition from + to - symmetry in a homonuclear molecule. Instead, this is a magnetic dipole transition, making it much weaker than electric dipole transitions. As was discussed above, a weak transition is desirable for this application, particularly at longer ranges.

Magnetic dipole transitions also have different selection rules [21] with regard to changes in J, the rotational quantum number, and K, the spin-removed angular momentum. First, only transitions between symmetric states are allowed in a homonuclear molecule. The lower triplet state in O_2 is symmetric only for odd values of K, while the upper singlet state is symmetric only for even K. Secondly, the ΔJ can only be 0 or 1 (and the $J''=0$ to $J'=0$ transition is not allowed). These rules result in four distinct branches traditionally designated PP, RR, QP and QR, as is shown in schematically in Figure 2.2.

9
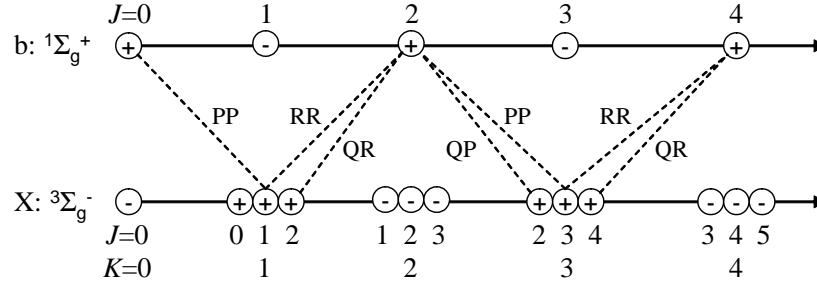
Figure 2.2: Magnetic dipole transition rules for homonuclear molecules [37]. Dotted lines indicate allowed transitions.

Two of these branches can be seen in Figure 2.3, a high-resolution spectrum of atmospheric attenuation in the region of the P-branch of the $O_2(b \leftarrow X)$ transition. This plot shows the spectrum as predicted by FASCODE, a detailed atmospheric model that will be described later. This model also includes the less abundant $O^{16}{:}O^{18}$ isotope. This is not a homonuclear molecule, so transitions between anti-symmetric states are also allowed, resulting in more lines for the fainter isotope spectrum. These fainter lines may be useful at longer ranges where the primary lines become saturated.

2.2 Structure of the Atmosphere

In order to understand how the spectrum evolves over a long path, it will be necessary to have some basic understanding of the structure of the atmosphere. Atmospheric conditions vary greatly in time and space, but the U.S. Standard Atmosphere (1976) [10] is a useful model to understand the structure of the atmosphere under typical conditions. This section will briefly summarize some of this information; more detail is available in references [10] and [24].

For altitudes up to 86 km, turbulent mixing is assumed to keep the relative makeup of the atmosphere uniform. The equations of this section are only valid up to that altitude. Above 86 km computations are much more complex, but for this project the air above that boundary is too thin to be of any real use in ranging.

To compute the structure of the atmosphere, begin with the temperature profile. This is computed by dividing the atmosphere up into different layers. Over each layer,

10
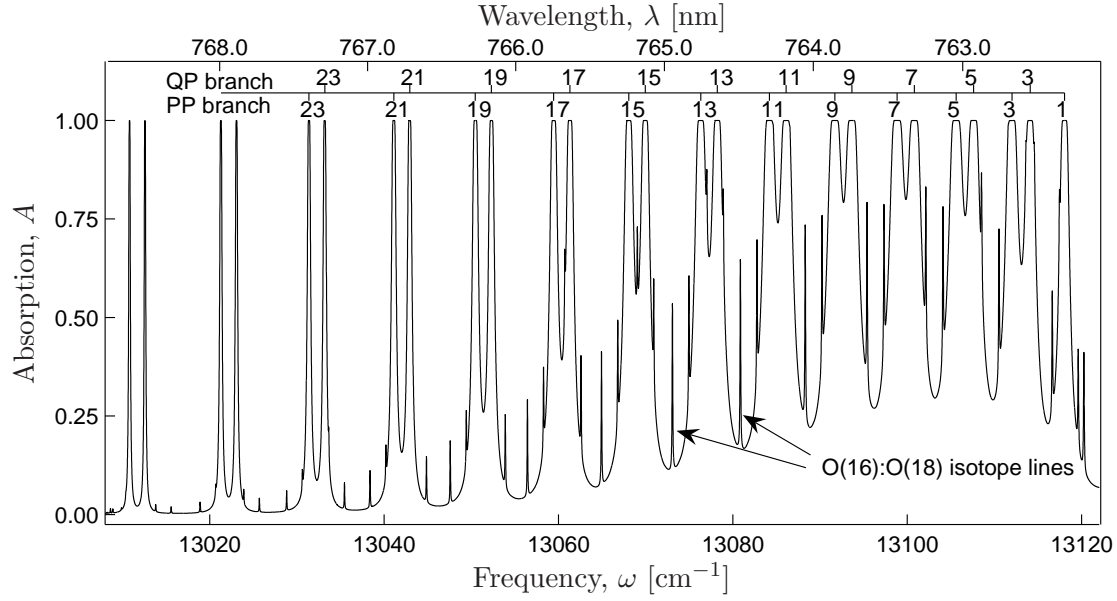
Figure 2.3: Modelled high-resolution absorption spectrum (calculated by FASCODE for 25km horizontal path with sensor located 5km above sea-level) showing the QP and PP branches. The line labels represent the rotational quantum number of the absorbing molecule, J''. The finer, unlabelled lines are absorption by the less abundant isotope [2].

the temperature, t, is assumed to be linear with altitude, z. The rate of change, also known as the lapse rate, $\varphi \equiv dt/dz$, is constant over each layer, so

$$t(z) = t_b + (z - z_b)\varphi, \tag{2.1}$$

where t_b and z_b are the temperature and altitude at the bottom boundary of the present layer. The boundaries and lapse rates for each layer are provided in Table 2.1.

Table 2.1: *Boundaries defined in US Standard Atmosphere.*

Altitude [km]	Lapse Rate, φ [K/km]	Altitude [km]	Lapse Rate, φ [K/km]
0-11	-6.5	47-51	0.0
11-20	0.0	51-71	-2.8
20-32	1.0	71-86	-2.0
32-47	2.8	>86	non-linear

The pressure profile is defined by the differential equation,

$$\frac{dP}{P} = -\frac{a_o}{t}dz, \tag{2.2}$$

where P is pressure and a_o=34.18 K/km. In regions where t is constant (φ=0), the solution is straightforward. If t is also a function of z, the differential equation can be solved by multiplying both sides of the equation by the integrating factor $\xi = \exp\left(\int a_o/t(z)dz\right)$, which results in

$$\frac{P}{P_b} = \begin{cases} \exp\left[-a_o(z-z_b)/t\right], & \varphi=0; \\ \left(t_b/t(z)\right)^{(a_o/\varphi)}, & \text{otherwise.} \end{cases} \tag{2.3}$$

Temperature and pressure are calculated from the ground up, starting with the standard sea-level pressure of P_o=101.325 kPa and temperature $t_o = 288.15$ K. Scaling rules (2.1) and (2.3) are used to find the conditions at the top of the first layer, which are then used as the P_b and t_b for the next layer. This process is repeated for each layer up to 86 km.

Once the temperature and pressure are computed for each altitude, the ideal gas law is used to find the total number density. The concentration of molecular oxygen is then assumed to be 20.95% of the total concentration (after humidity is removed–see Appendix B). The results of all these computations are shown in Figure 2.4. Note that the pressure and concentration profiles are still well approximated by an exponential.

There are also other standard atmospheres defined in FASCODE using similar rules to represent typical atmospheric conditions in environments from arctic to tropical. All of these standard atmospheres represent clear blue sky with no major weather activity.
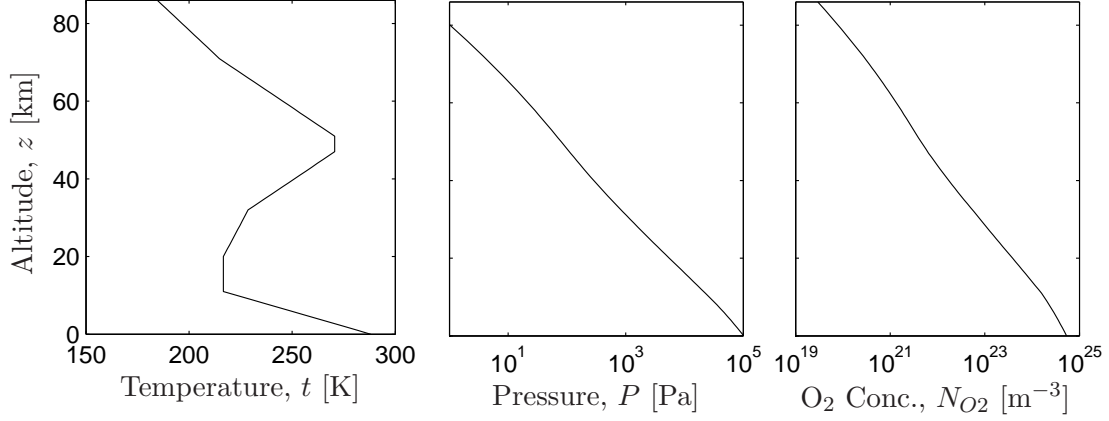
Figure 2.4: Temperature, Pressure and Concentration profiles of the US Standard Atmosphere.

2.3 Beer's Absorption Law

Absorption is assumed to follow Beer's Law:

$$dI = -\kappa I d\ell, \tag{2.4}$$

where I is the intensity of light incident on a incremental path length $d\ell$ and κ is an attenuation coefficient. The attenuation coefficient for light at frequency ω due to absorption on a transition from state i to state j is

$$\kappa_{ij}(\omega) = \sigma_{ij} f(\omega - \omega_{ij}) \left[N_i - \frac{g_i}{g_j} N_j \right], \tag{2.5}$$

where σ is the transition cross-section, N is the number density of particles in a given quantum state, g is the degeneracy factor, and $f(\omega)$ is the lineshape function. For the temperatures and energy spacings of interest for this problem, the upper state population, N_j, will be negligible, so this can be simplified to

$$\kappa_{ij}(\omega) = \kappa_i(\omega) = \sigma_i f(\omega - \omega_i) N_i. \tag{2.6}$$

13

The total attenuation at a given frequency, ω, will generally contain a contribution from several transitions, as well as scattering, so

$$\kappa(\omega) = \sum_i \kappa_i(\omega) + \kappa' = \kappa' + \sum_i \sigma_i f(\omega - \omega_i) N_i, \tag{2.7}$$

where κ' is the attenuation coefficient for aerosol scattering. Here, it has been assumed that all transitions will have approximately the same lineshape, f, and that the sum is over all transitions (*i.e.* i now indexes transition lines, not lower states). In actuality, the pressure broadening coefficient is a weak function of the rotational quantum number, J, so the lineshapes will not be identical. This effect is small compared to the Doppler broadening term and is neglected here.

For the spectral region of interest in this project, there will only be one absorbing species, so the notation can be simplified by using $\sigma_\omega = \sigma f(\omega)$ as the total frequency-dependent cross-section, or

$$\kappa(\omega) = \kappa' + \sigma_\omega N. \tag{2.8}$$

If κ is constant with respect to ℓ, then equation (2.4) can be directly integrated to yield the more familiar form of Beer's Law, $I = I_o e^{-\kappa L}$, where I_o is the initial intensity and L is the total path length.

For the cases of interest here, the atmosphere will not be homogeneous in general, so κ cannot be assumed constant. To solve the differential equation with variable N [5], multiply both sides of equation (2.4) by an integrating factor, $\chi(\ell) = \exp\left[\int_0^\ell \kappa(\ell) d\ell\right]$, where ℓ is a dummy variable of integration over path length. This makes an equation in exact form,

$$\chi \frac{dI}{d\ell} + I\kappa\chi = \frac{d(\chi I)}{d\ell} = 0 \tag{2.9}$$

$$\chi I = \text{constant.} \tag{2.10}$$

The constant can be determined by noting that $\chi(0) = 1$ and defining $I(0) = I_o$. This gives

$$I(L) = \frac{I_o}{\chi(L)} = I_o \exp\left[-\int_0^L \kappa(\ell)\,d\ell\right]. \qquad (2.11)$$

If transmission, T, is defined as the ratio of the intensity at the receiver to the intensity at the source,

$$T(\omega, L) \equiv \frac{I(\omega, L)}{I_o(\omega)} = e^{-\kappa'L} \exp\left(-\int_0^L \sigma(\omega, \ell)N(\ell)d\ell\right). \qquad (2.12)$$

Here, the attenuation has been split into two terms; one for aerosol scattering and one for molecular absorption. The integral over the path for the aerosol term, κ', has been neglected because the distribution of aerosols in the atmosphere is not generally predictable or even straightforward to measure. Section 2.4.1 below will describe the proposed method for estimating the effects of aerosols without having to be concerned with integrating a detailed profile of aerosol concentrations.

The integral in equation (2.12) is also often defined as the optical depth, τ:

$$\tau_\omega \equiv \int_0^L \sigma(\omega, \ell)N(\ell)d\ell. \qquad (2.13)$$

For the case of a homogeneous atmosphere, σ will be constant with respect to ℓ, so it can be removed from the integral and the optical depth τ becomes a simple product of cross-section, σ, with the concentration length, $m = \int N d\ell$.

2.4 Inverse Problems

In order to understand the difficulties of range extraction, it is convenient to assume a homogeneous atmosphere in order to use the simpler version of Beer's Law;

$$T_\omega = \exp\left[-\sigma_\omega N L\right]. \qquad (2.14)$$

15

The absorber concentration can be found from pressure and temperature using the ideal gas law, so if atmospheric transmission can be estimated, equation (2.14) can be used to determine range.

Of course, the atmosphere is not homogeneous, so equation (2.12) must be used, which complicates solving for range. In addition, there are other issues with this idea. First, direct measurement of transmission is only possible if the source spectrum is known. Second, Beer's Law (Equations (2.12) and (2.14)) describes the *monochromatic* transmission, while actual instruments will measure the average transmission in some band. Unless the observation bandwidth is small compared to the transition linewidth, the data will not obey the simple exponential of Beer's Law. The subsections that follow will address these issues and outline the proposed solution.

2.4.1 Measuring Transmission. Transmission is defined as the ratio of the transmitted signal, I_t, to the original signal (at the source), I_o,

$$T_\omega = \frac{I_t(\omega)}{I_o(\omega)}. \tag{2.15}$$

The measured signal is attenuated by both molecular absorption and aerosol scattering, so the total transmission, T_ω, can be written as a product of individual species transmissions according to Lambert's law. Additionally, any measurement will also be affected by the spectral response of the detection system, $\mathcal{R}(\omega)$, so that the measured signal is

$$I_m(\omega) = I_t D(\omega) = I_o(\omega) T_{\text{scat}}(\omega) T_{O2}(\omega) \mathcal{R}(\omega). \tag{2.16}$$

Note that the true measured signal would also involve a convolution with the instrumental lineshape which has been omitted for clarity in this equation.

Ideally, one would like to develop a ranging method that depends only on T_{O2}, which is much more predictable and more strongly correlated to range than the other components of I_m. If the baseline intensity, $I_b(\omega)$, is defined as the product of these

16

unwanted terms, then

$$I_m(\omega) = T_{O2}(\omega)I_b(\omega). \tag{2.17}$$

For measurements outside the absorption band, $T_{O2} \simeq 1$, so

$$I_m(\text{out of band}) = I_b(\omega). \tag{2.18}$$

In other words, the out-of-band measurements are direct estimates of the baseline. As long as all the terms in I_b are slowly varying compared to the oxygen spectrum, the out-of-band values can be used to interpolate a value of the baseline within the O_2 band. An example of this interpolated baseline is shown in Figure 2.5. If $\tilde{I}_b$ is used to denote this interpolated value (estimated from the out-of-band data), the oxygen spectrum can be estimated by a simple ratio of the observed values to the computed value of the baseline;

$$T_{O2}(\omega) \simeq \frac{I_m(\omega)}{\tilde{I}_b(\omega)}. \tag{2.19}$$

In practice, the baseline, $\tilde{I}_b$, is calculated by fitting a quadratic polynomial through the data from 12,700-12,900 cm^{-1} and 13,200-13,400 cm^{-1}. The choice of band limits is somewhat arbitrary; wider limits are more tolerant of noise, but care should be taken before setting the limits too wide–the information closest to the absorption band is the most relevant. There are also other absorption bands that ultimately limit the choice of frequencies. These bands will be discussed in more detail below. In experimental data, small changes ($\pm$ 50 cm^{-1}) in the limits of these bands and use of higher order polynomials in fitting are found to have very little effect on the final answer.

The baseline computed in this manner is a good estimate of all factors that are slowly varying over the measurement bandwidth. One potential complication that will not in general be slowly varying is the background scene. Scattered sunlight (either off background scenery or in a blue-sky) will also undergo absorption by the O_2 band, so the effects of this contribution are not reflected in the baseline. The degree to which

17
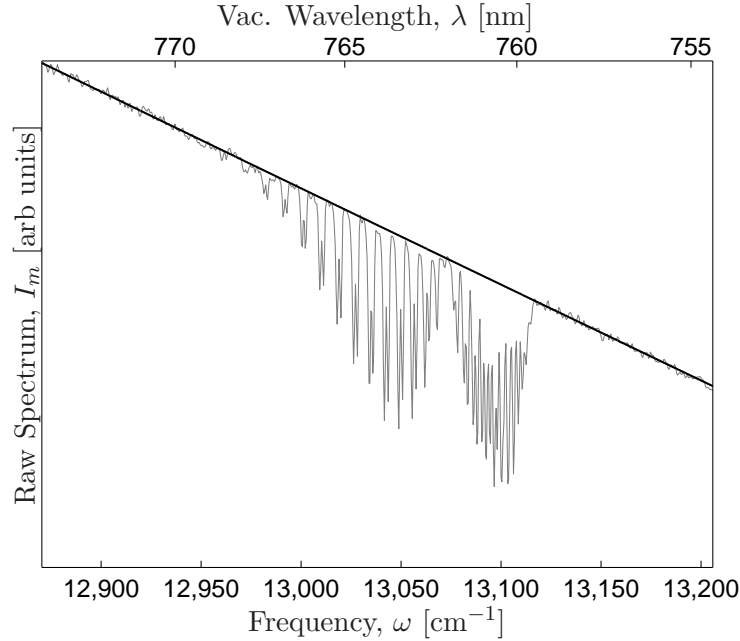
Figure 2.5: Raw spectrum (gray line) of 500 W halogen lamp observed through 41 m atmospheric path showing the calculated value of the baseline (black line) inferred from out-of-band data. Data was acquired with the ABB-Bomem MR254 FTIR at 1 cm^{-1} resolution as described in Chapter III.

this might be a problem depends a great deal on the field of view, as well as sensor altitude and zenith angle. There are a variety of background subtraction techniques that could be used to mitigate the effects. Examples will be shown in Chapter III. The background issues in the MWIR bands are simpler; if a spectrally isolated band (in a species with stable and predictable concentrations) could be identified, the techniques of this paper would be applicable to that band as well.

2.4.2 Band-Averaged Transmission. Even for uniform N, Beer's Law does not accurately reflect measurements taken at moderate spectral resolution [7, 11, 16, 17, 22, 24, 33, 36, 43]. Actual spectral measurements will be an average over some spectral band. For available instruments (and certainly for the filters used in MPR), this bandwidth will be too large to be considered monochromatic.

The band-averaged transmission is defined as

$$\bar{T}(\omega) \equiv \frac{1}{\Delta\omega} \int T_\omega d\omega = \frac{1}{\Delta\omega} \int \exp\left(-\tau_\omega\right) d\omega, \tag{2.20}$$

where T_ω denotes the monochromatic transmission, while $\bar{T}(\omega)$ is the average transmission in some band centered about ω. In contrast, applying Beer's Law to band-averaged observations implies that $\ln(\bar{T})$ is linear with some band-averaged optical depth, which is equivalent to saying that $\int \exp(\tau_\omega)d\omega = \exp(\int \tau_\omega d\omega)$ [1]. As a result, plots of $\ln(\bar{T})$ as a function of range are not linear, as was often assumed in previous MPR work.

This makes sense intuitively if one considers averaging over a band that includes both line peaks (frequencies near resonance) and wings of the line shape (frequencies far off resonance). At short ranges, the absorption in the wings is near zero, so the average will be dominated by the strong absorption of the peaks. As range increases, these lines increase in strength rapidly until they begin to saturate (*i.e.* absorb all the available light at that frequency). Once the line centers are saturated, however, they cannot absorb any more and any changes in $\bar{T}$ are now governed by the wings of the lineshape. Now it takes a much larger increase in range to cause the same change in $\bar{T}$. In other words, $|d\bar{T}/dl|$ is always decreasing with range. This effect is illustrated in Figures 2.6 and 2.7.

Although this picture of saturated lines is helpful in understanding why the plots of $\ln(\bar{T})$ as a function of range should be curved, some degree of curvature will still be present in the absence of true saturation.

2.4.3 Metric-based approach. The preceding sections discuss the issues that complicate the idea of solving Beer's Law for range. This type of problem is known as an inverse problem, where the task is essentially to "undo" an integral.

One method of approaching this sort of problem is shown schematically in Figure 2.8. A metric (or possibly a set of metrics) is computed from observed spectra

19
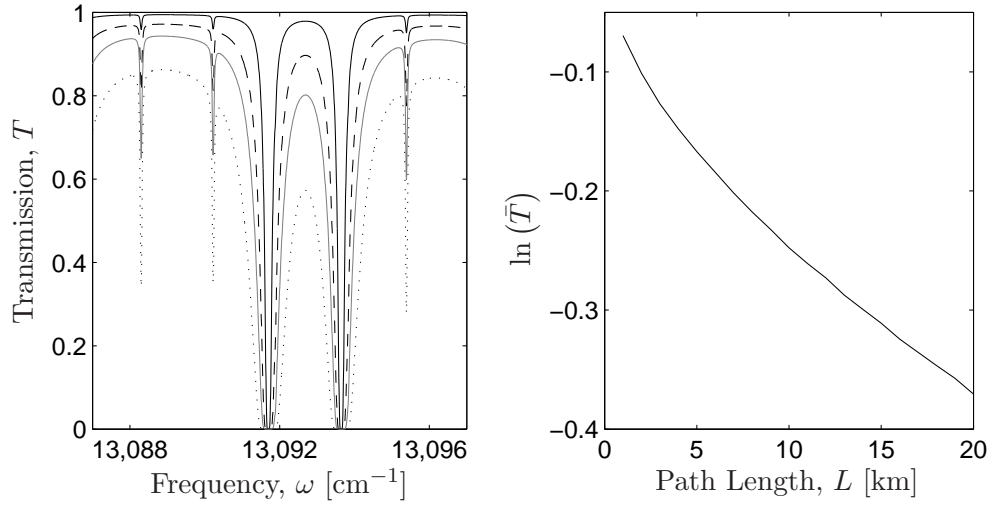
Figure 2.6: *Left*: FASCODE-predicted spectra (about the J=9 doublet) at ranges of 1, 5, 10 and 25 km, for a horizontal (homogeneous) path. *Right*: natural log of average transmission ($\ln \bar{T}$) over the band shown at left.
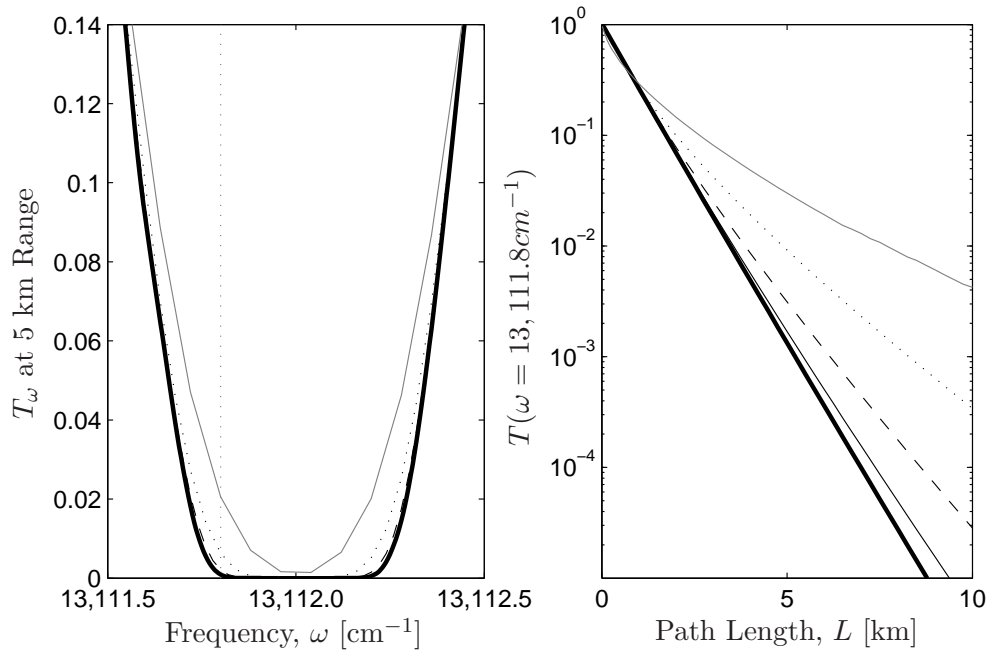
Figure 2.7: *Left*: FASCODE-predicted spectra at several different instrument linewidths for a homogeneous path. The spectral region shown here is about the center of the PP(J=1) line. *Right*: The transmission value at $\omega = 13111.8$ cm^{-1} calculated for each value of linewidth. In both plots, the lines represent resolutions of 0.01, 0.02, 0.04, 0.08 and 0.16 cm^{-1} (from bottom to top).

20
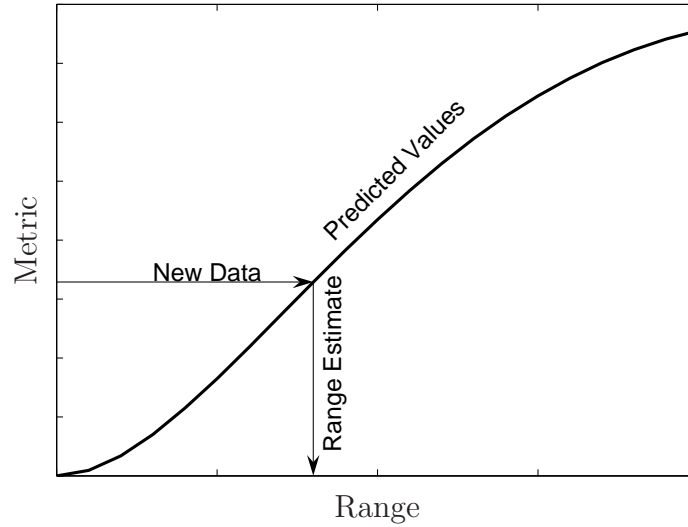
Figure 2.8: A hypothetical plot of metric value vs. range to illustrate the metric-based approach to range estimation

in order to reduce the dimensionality of the problem. Plots of the metric value(s) as a function of range are prepared from historical data, computer models, or band-model theory (which will be presented below in section 2.5). When new observations become available, they are plotted on this curve. The value of range at which the curve matches the new observation is the range estimate.

There are many metrics that one could compute from measured spectra. An ideal metric would be:

1) insensitive to differences in target spectrum, aerosol scattering and instrument,
2) dependent only on quantities that are readily measured,
3) predictable and repeatable,
4) a strong function of range,
5) monotonic with range (single-valued).

2.4.3.1 Intensity Ratios. One method that has seen extensive use is differential absorption, in which the metric is the ratio of intensities observed at two different frequencies. Choosing the frequencies to use in the intensity ratio is important to range accuracy. Typically, frequencies are chosen so that one frequency is near resonance with a molecular transition, while the second is as far off resonance as possible. The off-resonance measurement is weakly dependent on the amount of

21

the absorbing species, while the on-resonance measurement is strongly dependent. This ratio is, therefore, assumed to be a strong function of range and single valued.

For this to be independent of source properties and aerosols, the off-resonance measurement must be a good estimate of the baseline value as discussed in section 2.4.1. This frequency must be chosen as close as possible to the frequency of the on-resonance line (because the baseline is not constant), and yet still be several half-widths away from the nearest absorption line. Frequency selection can, therefore, be quite challenging.

Samples of this sort of ratio are shown in Figure 2.9. These are ratios of transmission values at two frequencies, rather than ratio of intensities. If the source spectrum, aerosol scattering and system spectral response properties are assumed to be constant with range, then the curves below can be multiplied by ratio of source intensity at the same frequencies to produce plots of expected intensity as a function of concentration length.

In principle, this works well, but has two drawbacks. First, the ratio will be strongly dependent on instrument resolution. Secondly, since only two of all the available data points are used, this tends to be somewhat susceptible to noise. Metrics that make use of more data will benefit from some amount of noise averaging to minimize errors.

2.4.3.2 Band-Average Metrics. One simple way to make use of more of the available information is to average over the entire band. If the observed intensity is averaged over the entire band, the noise should average to near zero (for a sufficiently large number of spectral channels). This straight average of observed data, however, also includes estimates of the source spectrum, aerosol, and system response, so the ratio of the observed data to the calculated baseline is used instead. The metric recommended for this research is the band-averaged absorption, $\bar{A}$, defined as

$$\bar{A} \equiv 1 - \bar{T} = \sum_{\Delta\omega} \left(1 - \frac{I_m(\omega)}{\tilde{I}_b(\omega)} \right), \tag{2.21}$$

22
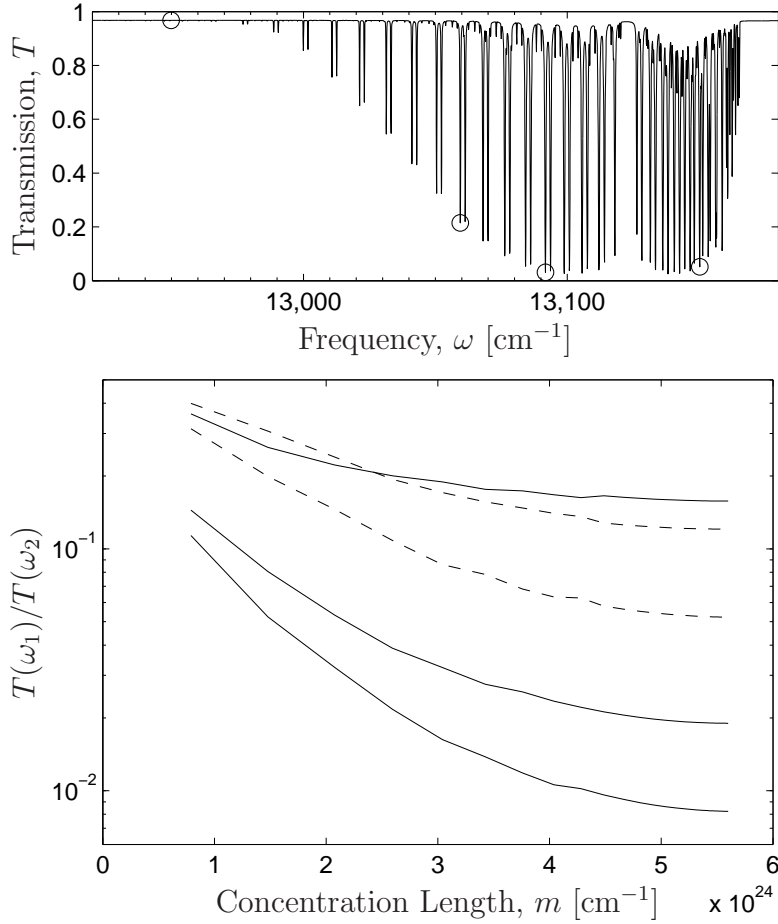
Figure 2.9: Ratio of the FASCODE-predicted Transmission at two frequencies. *Top* : FASCODE spectrum. (∘) indicates the frequencies used to generate the bottom plot. *Bottom* : Solid lines are ratio of absorption lines vs. the out-of-band baseline (T at 12,950 cm^{-1}); dashed lines are ratios of two absorption lines.

where the average is over the entire absorption band (about 12,900-13,170 cm^{-1}), or over the R-Branch alone (13,121-13,170 cm^{-1}). The choice of bands will be discussed in more detail in section 4.4. Note that the same metric can be computed from FASCODE-predicted transmission spectra, where transmission values are used rather than intensities. By computing the ratio of total transmission to the baseline, the affects of aerosol scattering are removed, so the ratio depends only on molecular absorption, as before. Examples of the band-average absorption metric and comparison against frequency ratios computed from measured data will be shown in Chapter III.

2.5 Band Models

Line-by-line models like FASCODE [40–42] compute equation (2.12) numerically, and can be very accurate (when given accurate inputs). For this project, however, it will be useful to have a functional form that describes the curves of $\bar{A}$ as a function of L. This will be useful for fitting to the data to generate metric curves, and will be essential in understanding what limits the accuracy of this technique. For this, one must investigate band-models that were developed to approximate the behavior of $\bar{A}$ before advances in computing power made line-by-line calculations practical. These band models are the heart of the lower resolution atmospheric transport codes like MODTRAN and LOWTRAN [27].

With some simplifying assumptions about the nature of σ_ω, equation (2.20) can be integrated. There are a variety of assumptions that could be made, each of which leads to a different functional form, or band model. Goody and Yung [17] present an excellent review of the different models that could be used. It is worth noting that a representation of σ_ω need not necessarily bear a strong resemblance to the actual form of the band in order to be a good model; it need only behave the same *on average*.

Presented below is a brief summary of the origins and resulting equations for some of the models evaluated. A more detailed look at a few of the key models is available in Appendix A.

First, in keeping with the common notation in the literature, a few new quantities must be defined:

$$x = \omega/\delta \qquad y = \alpha/\delta \qquad u = Sm/2\pi\alpha, \qquad (2.22)$$

where α is the linewidth, δ is the average line spacing and S is the line strength, such that $\sigma_\omega = Sf(\omega - \omega_o)$. Note that for a Lorentzian lineshape (normalized to unit area), $f(\omega = \omega_o) = 1/\pi\alpha$, so u is equivalent to $\tau/2$ at line center. The parameters x and y are simply normalized (unitless) frequency and linewidth.

24

2.5.1 Isolated Line Models.   The simplest of models examine the behavior of the average absorption in a band that contains a single absorption line. One might also suppose that a collection of lines (like a molecular band) might, when spectrally averaged, behave similarly to the average over a band containing a single line of some arbitrary line strength and width. Any lineshape may be assumed here, but Lorentzian and Doppler profiles are the most common:

$$\text{Lorentzian} \qquad \bar{A} = 2\pi y \mathcal{L}(u) \tag{2.23}$$

$$\text{Doppler} \qquad \bar{A} = \frac{\alpha}{\delta} \int_{-\infty}^{\infty} 1 - \exp\left[-u e^{-x^2}\right] dx. \tag{2.24}$$

Here, $\mathcal{L}(u)$ is known as the Ladenburg-Reiche function [28]. It describes the equivalent width of a Lorentzian lineshape, and is defined in terms of the Bessel functions of imaginary arguments, I_j,

$$\mathcal{L}(\xi) = \xi \exp(-\xi) \left[I_0(\xi) + I_1(\xi)\right]. \tag{2.25}$$

2.5.2 Regular (Elsasser) Models.   Regular models assume that σ can be represented as a uniform array of lines. While not quite uniformly spaced, the lines of the O_2 P-branch are quite regular, suggesting that this might not be a bad model. In the case of the Elsasser model, the most commonly used regular model, the lines are assumed to be equal-strength and have a Lorentzian line shape. With this assumption, equation (2.20) can be solved exactly. The resulting solution can be simplified further by making additional assumptions about the band. The equations used here are the exact solution and an approximate solution for the case of well-separated lines (*i.e.*, the linewidth, α, is much less than the spacing, δ):

$$\text{Elsasser (exact)} \qquad \bar{A} = 1 - \int_{-\infty}^{\infty} \exp\left[\frac{-2\pi u y \sinh 2\pi y}{\cosh 2\pi y - \cos 2\pi x}\right] dx, \tag{2.26}$$

$$\text{Sparse Limit } (y \ll 1) \qquad \bar{A} \simeq \text{erf}[\pi^{3/2} y \mathcal{L}(u)]. \tag{2.27}$$

25

2.5.3 Distribution Models.   Distribution models are based on assuming the position of the lines within the band is not significant; only the relative strengths of the different lines. A distribution function is used to describe the relative probability of a given line strength. Rather than integrating over a spectral band, $d\omega$, the distribution is integrated over a range of line strengths, dS.

In general, the absorption is given by

$$\bar{A} = \frac{1}{\delta} \int\limits_{0}^{\infty} p(S) \int\limits_{-\infty}^{\infty} 1 - \exp\left[-Smf(\omega)\right] d\omega dS, \qquad (2.28)$$

where the first integral (over ω) represents the contribution from a single line of strength S, and $p(S)$ represents the probability of having a line of that strength.

As with the other models, one could use a variety of lineshapes here, as well as a functional form of $p(S)$. Some common choices are:

$$\text{Exponential} \qquad p(S) = \frac{1}{\bar{S}} \exp(-S/\bar{S}), \qquad (2.29)$$

$$\text{Godson} \qquad p(S) = \begin{cases} \bar{S}/SS_c, & S < S_c; \\ 0, & \text{otherwise,} \end{cases} \qquad (2.30)$$

$$\text{Malkmus} \qquad p(S) = \frac{1}{S} \exp\left(-S/\bar{S}\right), \qquad (2.31)$$

where $\bar{S}$ is the mean linestrength.

Equation (2.28) is integrable for any of these distributions if a Lorentzian lineshape is used. This gives:

$$\text{Exponential} \qquad \bar{A} = \frac{2\pi y \bar{u}}{\sqrt{1 + 2\bar{u}}}, \qquad (2.32)$$

$$\text{Godson} \qquad \bar{A} = 2\pi y (\bar{S}/S_c) \left[I_0(\bar{u}) \exp(-\bar{u}) + 2\mathcal{L}(\bar{u}) - 1\right], \qquad (2.33)$$

$$\text{Malkmus} \qquad \bar{A} = \frac{\pi y}{2} \left[\sqrt{1 + 8\bar{u}} - 1\right]. \qquad (2.34)$$

26

2.5.4 Random Models. The line spacings do, of course, follow a distinct pattern, but the pattern can be so complex that it appears random. Assuming an array of randomly spaced but equal strength lines leads to the standard random model. The general random model results from assuming the line strength and position are both random. One could also assume that a band can be described as a random combination of several regular bands (for example, the four branches of the O_2 band described in section 2.1 might be represented as four independent regular arrays). This results in the random band model. Interestingly, the mathematical form of all three models is identical for a sufficiently large number of lines or bands. As with distribution models, any lineshape can be used within the random model, so

$$\text{Standard or General} \quad \bar{A}(\text{band}) = 1 - \exp(-\bar{A}(\text{isolated line})), \quad (2.35)$$

$$\text{Random Bands} \quad \bar{A}(\text{band}) = 1 - \exp(-\bar{A}(\text{regular band})). \quad (2.36)$$

Here, the $\bar{A}$ terms on the right hand side of the above equations can be computed using any of the equations from sections 2.5.1 or 2.5.2.

Figure 2.10 shows hypothetical examples of some of these models.

2.6 Comparison with MPR

With this theoretical basis established, it is now appropriate to examine the approach used by the MPR program and discuss the differences used in the present work.

There have been several papers published relating to MPR [8,9,12,20,23,30–32], each of which makes a slightly different variation, but the general theme begins with Beer's Law and the ratio of intensity at two different frequencies. The observed intensity at some frequency, ω, will depend on the source intensity and the atmospheric transmission at that frequency,

$$I(\omega) = I_s(\omega) \exp\left(-\int_0^L \sigma N d\ell\right). \quad (2.37)$$

27
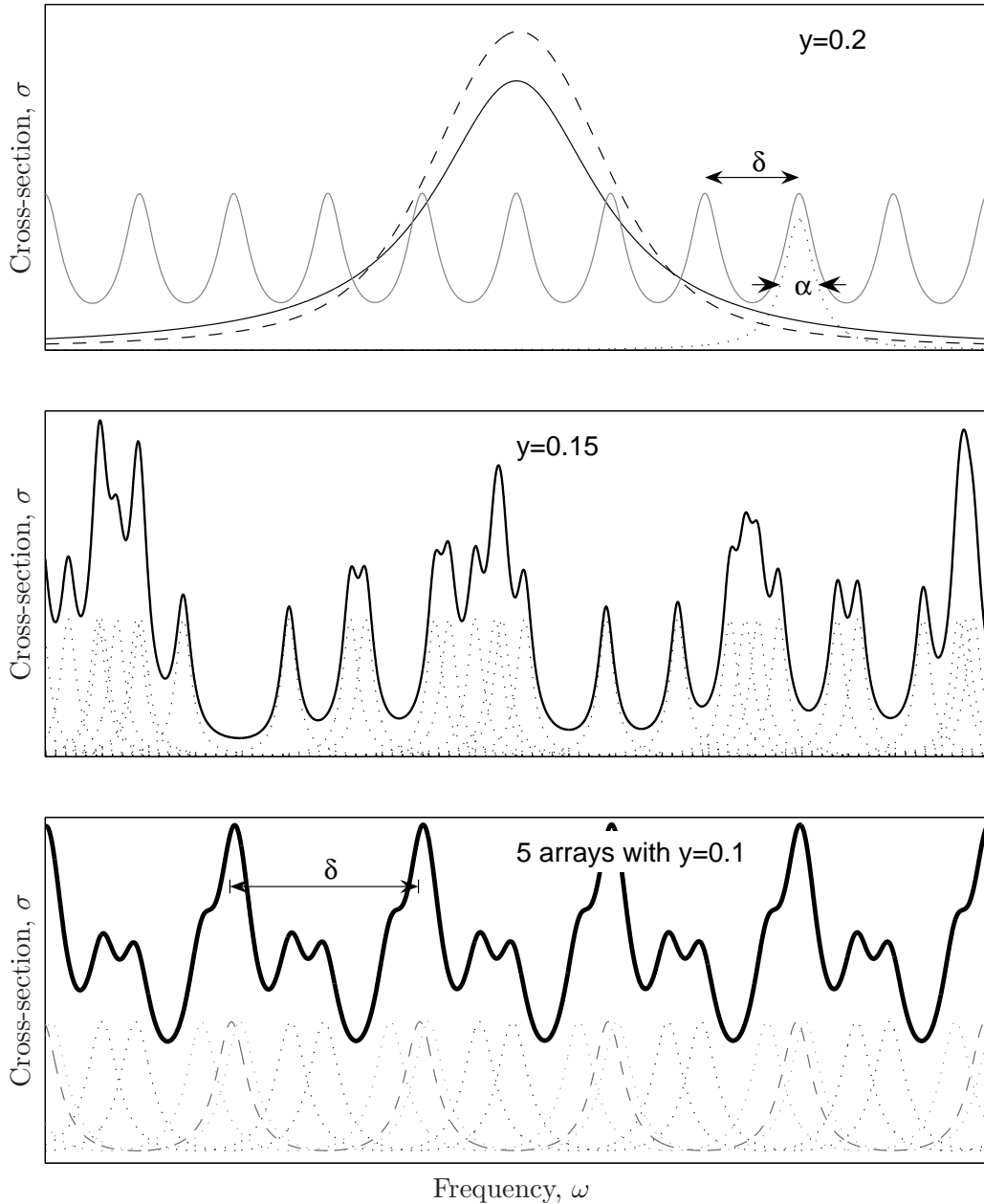
Figure 2.10: Example spectra for various band models. Top : Isolated Lorentzian (–) and Doppler (- -) lines (normalized to equal area) and an Elsasser band. The dotted line ($\cdots$) shows one of the component lines of the Elsasser array. $Middle$: Standard Random Model–a collection of randomly placed identical Lorentzian lines $Bottom$: Random band model–superposition of five randomly located but otherwise identical Elsasser bands.

28

The ratio of intensities measured at two different frequencies is then

$$\frac{I(\omega_1)}{I(\omega_2)} = \frac{I_s(\omega_1)}{I_s(\omega_2)} \exp\left(-(\sigma_2 - \sigma_1)\int_0^L N d\ell\right). \tag{2.38}$$

Here, the papers generally assume the ratio of source intensities and the difference in absorption cross-sections will both be known. This allows one to directly solve for the path length, L.

There are several issues with this technique. First, knowing the ratio of source intensities can often require that the target be identified (or at least classified). Reliable spectral data on missile exhaust plumes (their primary target) is not always readily available. Furthermore, the plume spectrum can even change with altitude [31] as the after-burning chemistry changes due to varying pressure and oxygen content of the ambient air. To accurately estimate the range using MPR one would need to first know the altitude. But the altitude of a rocket is easy to estimate from angle data *given range*.

Secondly, the difference in cross-sections is actually quite complicated. It is fair to assume that the cross-sections for CO_2 are well known for each frequency and temperature. But the total attenuation coefficient depends also on aerosol scattering, extinction due to propagation through clouds [31], and (for some frequencies) absorption by other molecules. In addition, changes in temperature along the line-of-sight will affect the cross-section for CO_2 since the number of absorbers in a given state, N_i, is temperature dependent.

Both of the above issues are appropriately identified in past work, and attempts are made to compensate the data to correct for these effects. For the most part, however, all that can be done is to attempt to model these effects. Each assumption in this process will introduce error. This is an issue inherent in using intensity ratios. In contrast, the present work uses the band-average absorption rather than the ratio of two intensities. Because the baseline can be inferred from the data (as discussed in section 2.4.1), the metric used here should not depend on the source spectrum. By

29

averaging over the entire band, all rotational transitions are included, so the thermal population of various states does not affect the metric. The number of absorbers in the path, N, will change with temperature, but the cross-section will not.

One issue that is not addressed in published MPR work is the application of Beer's Law to broadband observations. The ratio of observed intensities in equation (2.38) would be more appropriately written as

$$\frac{I(\omega_1)}{I(\omega_2)} = \frac{\int_{\Delta\omega_1} I_s(\omega) \exp(-\tau) \, d\omega}{\int_{\Delta\omega_2} I_s(\omega) \exp(-\tau) \, d\omega}. \tag{2.39}$$

The source intensities can be assumed slowly varying over the band and taken outside the integral, but σ_ω is certainly not. As a result, the equation used as a basis for range estimation is inaccurate.

There are some fortuitous frequency pairs for which Beer's Law is a good estimate of the ratio [23]. Figure 2.11 shows intensity ratios computed for one such frequency pair used in MPR. The information in the literature is insufficient to reproduce their results, but this example illustrates the difficulty of selecting filter bands that follow Beer's Law. The present work is more concerned with the general case. In the oxygen band of choice, plots of intensity ratio ($\ln[I(\omega_1/I(\omega_2)]$) or of absorption ($\ln(\bar{A})$) are found to have significant curvature that Beer's Law does not adequately describe.

Some papers [23] in this field also suggest using approximations (typically flat Earth and exponential atmosphere) for the structure of $N(L)$ to directly invert equation (2.12) for L. The assumptions needed to derive this analytic solution introduce error. The present work also uses approximate equations for $N(L)$ (derived for a curved-Earth), but not to directly solve L. Rather, it will be used to refine the theoretical form of the fitting equations, as will be discussed further in Chapter IV.
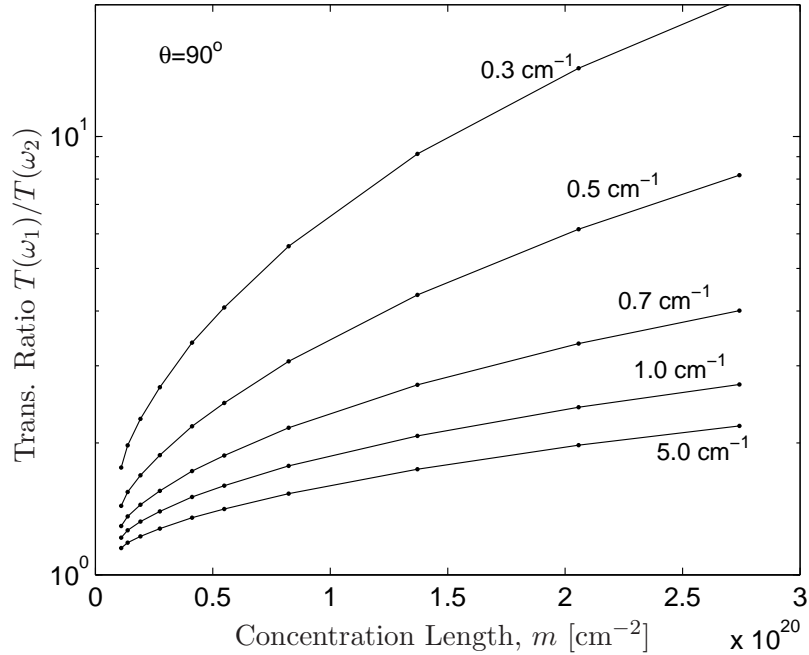
Figure 2.11: Transmission ratios computed from MODTRAN for a horizontal path, using the frequencies identified in [23]. Labels indicate the filter bandwidth.

2.7 Summary

This chapter shows measurements of the O_2 (X→b) band offer several advantages compared to IR bands for range estimation. Section 2.4 presents a range estimation method that is, in theory, insensitive to many of the factors that degrade accuracy in MPR. The chapters that follow will discuss the details of how this method is applied. First, Chapter III will describe the experiments that were conducted to verify these theories. Then Chapter IV will show how the band models of section 2.5 are modified and applied to these measurements.

31

III. Experiments

Several experiments were conducted to verify the theory presented in Chapter II. Due to the limitations of the hardware and the availability of large sources against which to test, experiments were limited to short ranges (up to 2.8 km). These short range experiments were intended to demonstrate the validity of the model, which is then used to extrapolate the results to longer ranges of operational interest. This chapter describes the equipment used, and outlines the tests that were conducted. Some of the raw data and simple results are also provided here; more detailed analysis will be presented in Chapter V.

3.1 *Instrument*

The instrument used for experimental verification was an ABB-Bomem MR-254 Fourier transform spectrometer, pictured in Fig 3.1. Some salient features of this instrument are:

– Spectral resolution is user selectable in steps of 2^n cm^{-1} (*i.e.*, 1, 2, 4, 8 ... cm^{-1}).

– This instrument has three different input telescopes and field stops to control field of view (FOV). Most of the data presented here used the narrow field-of-view (NFOV) telescope with no field stop for a full-angle FOV of 4.9 mrad.

– There is a standard video camera bore-sighted through the same input telescope to visually monitor instrument pointing and focus.

– Acquisition (scan) times depend on the resolution. For example: 10.2 scans/sec at 1 cm^{-1} or 64.6 scans/sec at 16 cm^{-1}.

– Preamplifier gain in the detectors can be set from 1-64 (in powers of 2) in software.

– Each interferogram (the data from one full scan of the interferometer) can be recorded individually, or multiple scans be digitally added to reduce noise and ease memory/data throughput requirements.

– The net throughput of the optical system is 27%.

32

– This instrument has two independent output channels that could mount a choice of three different detectors: Si, from 8,500-15,000 cm^{-1}; InGaAs from 5,800-10,000 cm^{-1}; or InSb from 1,800-7,800 cm^{-1}.

Figure 3.1:   Two photos of the Bomem MR-254 Fourier Transform Spectrometer with the NFOV telescope at Edwards AFB, CA (see section 3.3). Also visible: the Cannon XL-2 video camera used to document tests (left) and AFIT technician Greg Smith (right).

The Si detector was used for all experiments presented here. The overall performance of the system was poor in the visible band due to a combination of modulation efficiency and detector performance. Very bright sources were needed in order to acquire a useable signal level, which placed some limits on the experiments that could be conducted.

For example, in one experiment, a thermal source (approximating a blackbody) at 807°C filled the instrument FOV. The measured spectrum in this experiment had a signal-to-noise ratio (SNR) of about 0.9 (methods for estimating SNR from data will be discussed in more detail in section 5.1.2). This implies that the noise equivalent irradiance (NEI) is on the order of 10 mW/m^2. For comparison, the NEI of off-the-shelf thermal imagers is often on the order of 10 pW/m^2. The value of $\bar{A}$ computed from this noisy spectrum was actually negative, which is clearly non-physical.

While this sensor does place some limits on the experiments that could be performed, it is important to note that this is a limit of the sensor, not the technique. Chapter II showed that this technique should be applicable to any sensor. Section 5.1.2

33

Table 3.1:   *Summary of experiments with QTH lamp.*

Experiment	Location	Conditions	Parameters Tested
Hallway I	Building 194	Indoor	initial checkout
Hallway II	Building 194	Indoor	resolution dependence of metrics
Hallway III	Building 194	Indoor	test ranging & noise
Hallway IV	Building 194	Indoor	resolution dependence of noise
Hillside	WPAFB	Outdoor, evening/night, looking downhill	ambient light uncontrolled atmosphere
Hillside II	Edwards AFB	Outdoor, bright sun, looking uphill	instrument checkout blue sky background

will discuss how measurement accuracy (in the spectrum) affects accuracy of the range estimate, independent of the choice of instruments used to make the measurement.

3.2   *Experiments with Halogen Lamp Target*

Testing against rocket motors presents some logistical problems. The majority of the experiments in this project use electric lights as a source. While not necessarily representing a realistic target, this has the advantage of being highly repeatable for quick and easy verification of proposed techniques. As discussed in Chapter II, the techniques applied here should apply to any broadband emissive source (provided it is slowly varying over the absorption band).

The light used for these experiments (see Figure 3.6) is a 500 W Quartz-Tungsten-Halogen lamp (QTH). It is a standard commercial work light with 75 mm long element and a crude metallic reflector behind to direct the light into a solid angle of roughly 2-2.5 steradians. Table 3.1 provides a brief summary of the tests performed with the QTH lamp. Detailed descriptions of each are presented below.

3.2.1   Hallway-I Experiment (3 Sep 2004).   The goal of the first hallway experiment was simply to verify that the instrument functioned as expected and that the electronic data could be output in a form readable by MatLab. Spectra were acquired under the same conditions using different integration times, different input

telescopes (FOV) and different focus settings on the telescope. As expected, the spectra did not change other than the overall magnitude. When normalized, the differences in the spectra were negligible as long as the focus was set close enough that the source could be recognized visually on the monitor. Poor focus could allow more background light to fall on the detector.

3.2.2 *Hallway-II Experiment (16 Sep 2004).*   The next step was to experimentally verify the behavior of the metrics described in §2.4.3. Specifically, to verify the dependence of band-average absorption and intensity ratios on both range and resolution. To test this, the target was placed at seven different locations at ranges from 15.6 to 52.4 m away from the instrument pupil. At each location, spectra were acquired at instrument resolutions of 1, 2, 4, 8, 16 and 32 cm^{-1}. For each range and resolution, the recorded spectrum is an average over 1,000 scans of the interferometer arm.

Data from this experiment is shown in Figures 3.2 and 3.3. Figure 3.2 shows intensity ratios computed from this data, which shows that the ratios are dependent on resolution. The area under the absorption curve is constant, so lines measured at lower resolution will be low and wide compared to higher resolution measurements. Assuming the baseline value is independent of resolution, higher resolution measurements should be expected to yield higher ratio values. Figure 3.3 shows that $\bar{A}$ is independent of resolution, except possibly for the lower resolution data. At 32 cm^{-1} resolution, the absorption will be smeared out over such a broad spectral region that some measurable portion of it could be expected to extend beyond the frequency limits chosen for the integral. The integration band could be adjusted to account for this to appropriately measure $\bar{A}$ at any resolution, but for consistency, the same limits were applied in all cases here.

3.2.3 *Hallway-III Experiment (22 Sep 2004).*   The goal of the third experiment was to verify the idea of estimating range from metric curves (plots of $\bar{A}$ vs L). The old data taken on 16 Sep was used to derive a metric curve. New data, taken on

35
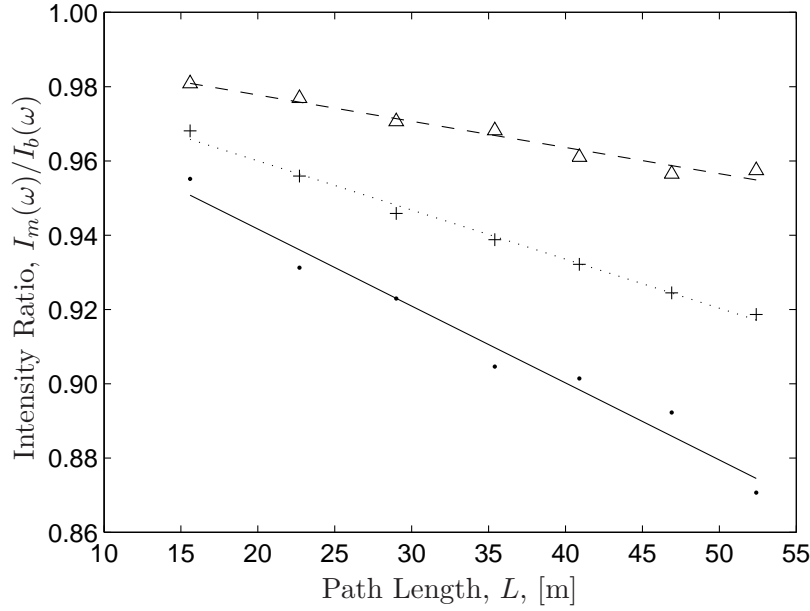
Figure 3.2: Intensity ratio as a function of range from the Hallway II experiment. The ratio used is the observed intensity at 13,093 cm^{-1} over the computed baseline value at the same frequency. Solid line (—) is 1 cm^{-1} resolution; dotted ($\cdots$) is 2 cm^{-1}; dashed (- - -) is 4 cm^{-1}.

a different day with different air pressure and temperature, was plotted against this curve to estimate range. In addition, measurements were repeated multiple times to help develop repeatability and error statistics. All measurements were taken using the same QTH lamp at a range of 36.6 m using the narrow FOV telescope (and no field stop). Preamplifier gain was set at 64 for all measurements.

3.2.4 Hillside Experiment (30 Sep 2004). The primary goal of the next experiment was to verify that this metric was repeatable in a different environment. The Bomem spectrometer and QTH lamp were taken outside, and the process was repeated at ranges up to 200 m to verify that observations of $\bar{A}$ would obey a similar curve. Results of this are shown in Figure 3.4.

The secondary goal was to qualitatively assess the importance of the background. Measurements were repeated several times at a constant range over roughly a one hour span beginning in late evening and continuing into full darkness. While the background was too dim for accurate direct background measurements with this

36
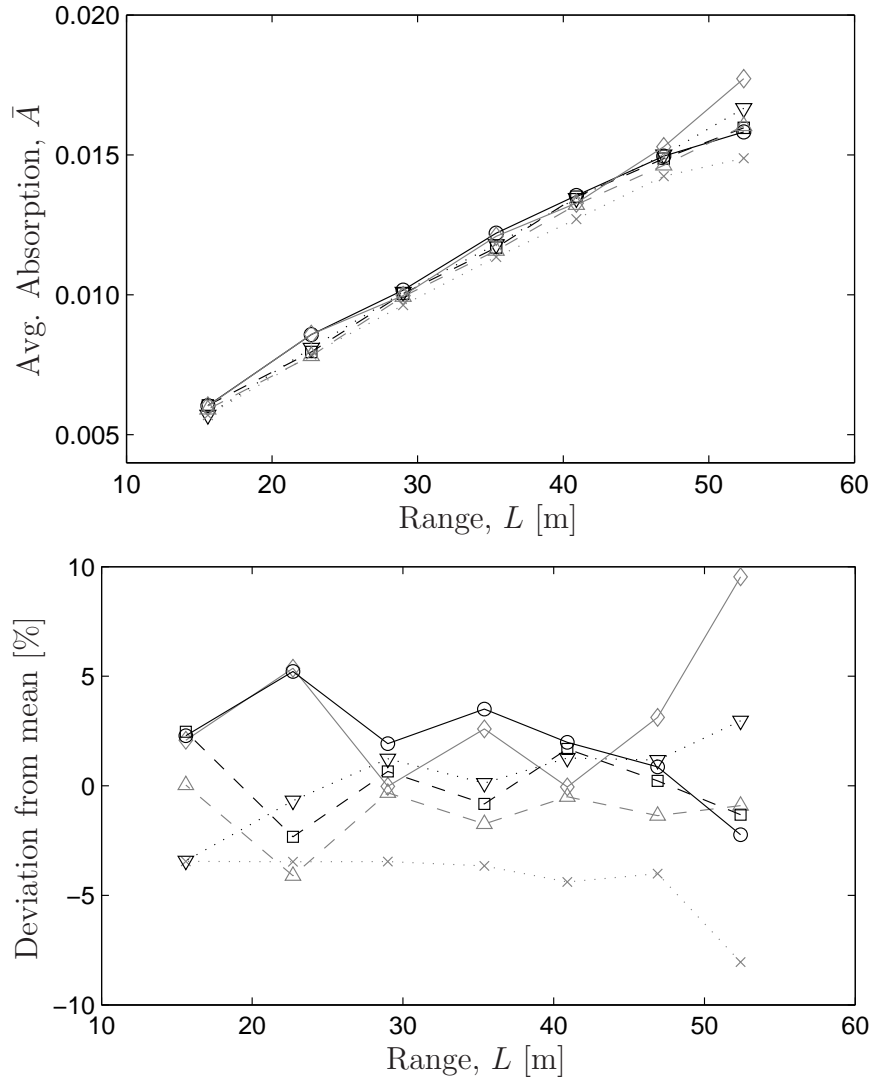
Figure 3.3: *Top* : $\bar{A}$ as a function of range computed from Hallway II experiment data. *Bottom* : Residual error compared to the average value (as a percent of average). In both plots, (○) represents 1 cm^{-1} resolution data; (□) is 2 cm^{-1}; (▽) is 4 cm^{-1}; (◇) is 8 cm^{-1}; (△) is 16 cm^{-1}; and (×) is 32 cm^{-1}.
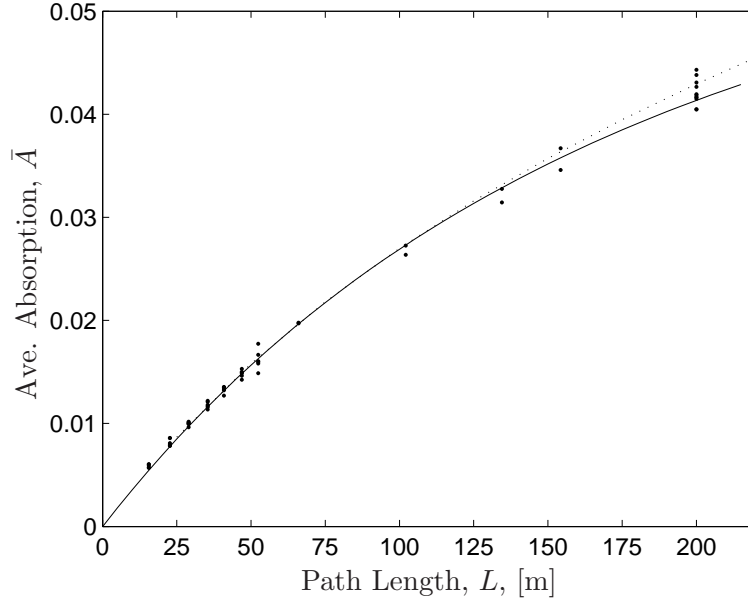
Figure 3.4:   Average absorption as a function of range for Hallway II
and Hillside experiments ($\cdot$). Data are well correlated with FASCODE
predictions ($\cdots$), and a single curve (—) can be fit to both data sets.

instrument, it was hypothesized that a changing background might still produce mea-
surable changes in the scene. The results in Figure 3.5 do not support this hypothesis,
although brighter background scenes might still have an impact.

3.2.5 Hallway-IV Experiment (08 Mar 2005).   In preparing to deploy the
instrument to Edwards AFB for the field test (to be described in the next section),
another experiment was conducted to help establish the best instrument settings. The
primary question was the impact of instrument resolution on the standard deviation of
$\bar{A}$. At lower resolution, there are fewer spectral sample points for noise averaging, so
one might expect more noise. On the other hand, there are more photons per spectral
channel at low resolution, indicating less noise. For an event of fixed duration (like a
motor burn), lower resolution on the Bomem instrument allows for more scans in the
same amount of time.

To settle this experimentally, 15 measurements were taken at each of two differ-
ent resolution settings (1 and 4 cm^{-1}). The total acquisition time was held constant
at 30 seconds, so the number of scans per measurement was different for the two res-
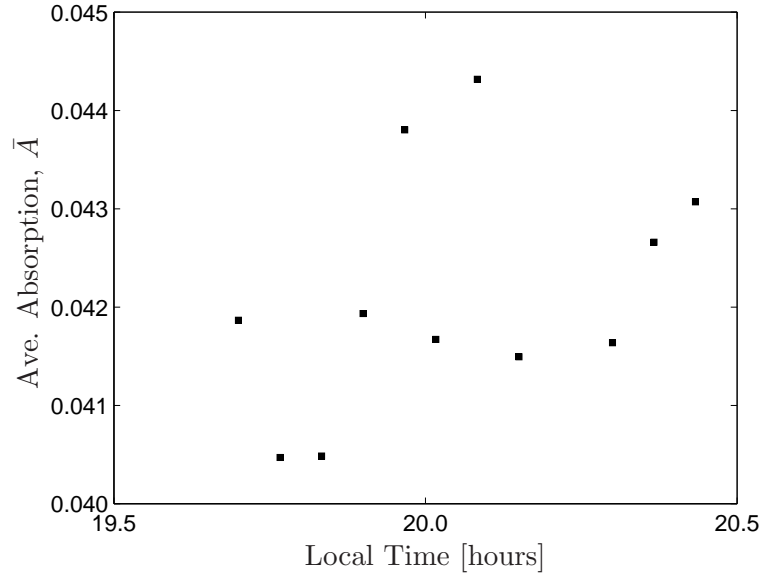
Figure 3.5: $\bar{A}$ as a function of time from Hillside-I experiment. Sun was setting during this time. Lack of correlation in this plot indicates that ambient light did not affect estimation of $\bar{A}$.

olutions (151 scans at 1 cm^{-1} and 522 at 4 cm^{-1}). The source was not moved and all other instrument settings were kept constant. The average value of $\bar{A}$ was the same for both settings, but the standard deviation of $\bar{A}$ computed from the high resolution spectra was over 2.5 times higher.

3.2.6   Hillside-II (29-30 Mar 2005).   Once the instrument was deployed to Edwards AFB for the field test (next section), observations of the QTH lamp, shown in Figure 3.6, were used to verify that the system was operating as expected.

This was the first opportunity to quantitatively test the impact of the background. As mentioned before, very bright sources were needed due to sensor limitations. The terrain available for experiments at Wright-Patterson AFB tended to place relatively dark vegetation and urban scenes in the background during lamp experiments. At Edwards AFB, it was possible to set up the lamp in such a way as to have significant amounts of bright blue sky in the background, as is shown in Figure 3.6. Not only is this relatively bright, but it also shows a strong O_2 absorption spectrum, as mentioned in section 2.4.1. Figure 3.7 shows sample spectra from this experiment

39

Figure 3.6: Photo of experimental setup for QTH observations at Edwards AFB, taken from the spectrometer location. Photo shows the QTH lamp and AFIT technician Greg Smith (right). Greg is not within the instrument FOV in this photo.

with the lamp on and off to compare the relative contribution of the background. Notice that the depth of the absorption band as a fraction of the baseline signal level is much greater in the background (as indicated by $\bar{A} = 0.29$ with the lamp off, compared to $\bar{A} = 0.08$ with the lamp on).
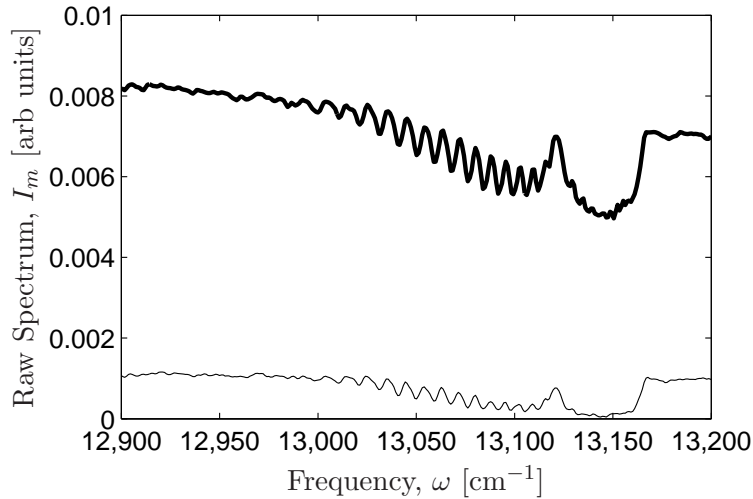
Figure 3.7: Sample data from the Hillside-II experiment with the QTH lamp on (—) and off (—) to show the relative contribution of the blue sky background. This data is at 2 cm^{-1} resolution. Note at this resolution the rotational lines are resolved, but the PP-QP doublets for each value of J are not.

Figure 3.8:   Photo of SRM test. The motor is laying horizontally with the nose pointed to the right in this view. The actual body of the motor is hidden from view by a protective berm. The black circle indicates the approximate FOV of the spectrometer.

3.3 Solid Rocket Motor Test (01 Apr 2005)

The Bomem instrument was not capable of tracking moving targets, so testing against representative targets was limited to static missile tests. AFIT had the opportunity to observe one such test at Edwards AFB. The source in this experiment was a large solid rocket motor (SRM) developed for satellite launch. Sensors were placed on top of a hill overlooking the motor at a distance (slant path length) of 2.82 km and at an aspect angle of roughly 75° off-nose. The motor was laid out horizontally and surrounded on three sides by a protective berm. The sensor was above the rocket looking down at an angle roughly $1.5°$ below horizontal, but portions of the plume were still obstructed by the berm and other equipment surrounding the test stand. A sample photo of the rocket burn is shown in Figure 3.8.

The rocket motor burned for approximately 90 sec. The instrument was set at 2 cm^{-1} resolution, so the scan rate was 9 scans per second. After ignition, gain was manually set (to 16) and then acquisition of ten measurements (at 80 scans per measurement) was initiated. The ten raw spectra are shown in Figure 3.9.

Note the two bright potassium emission lines present in this spectrum at about 767 and 770 nm. Potassium is a common contaminant in solid rocket propellants, so

41
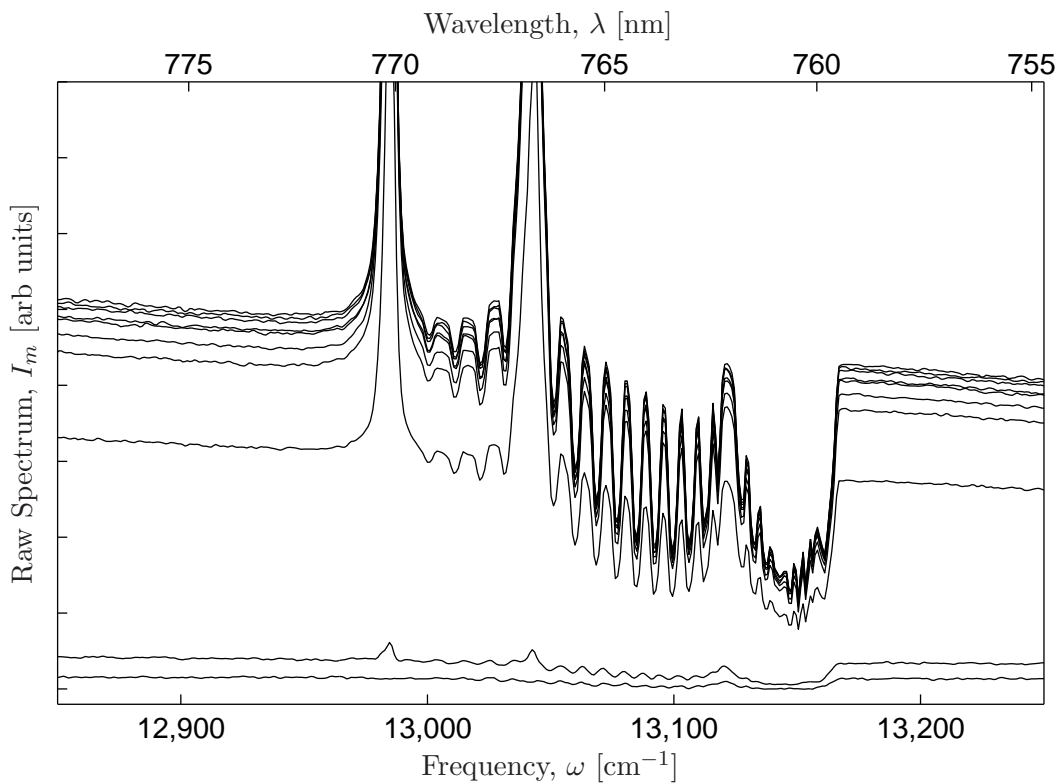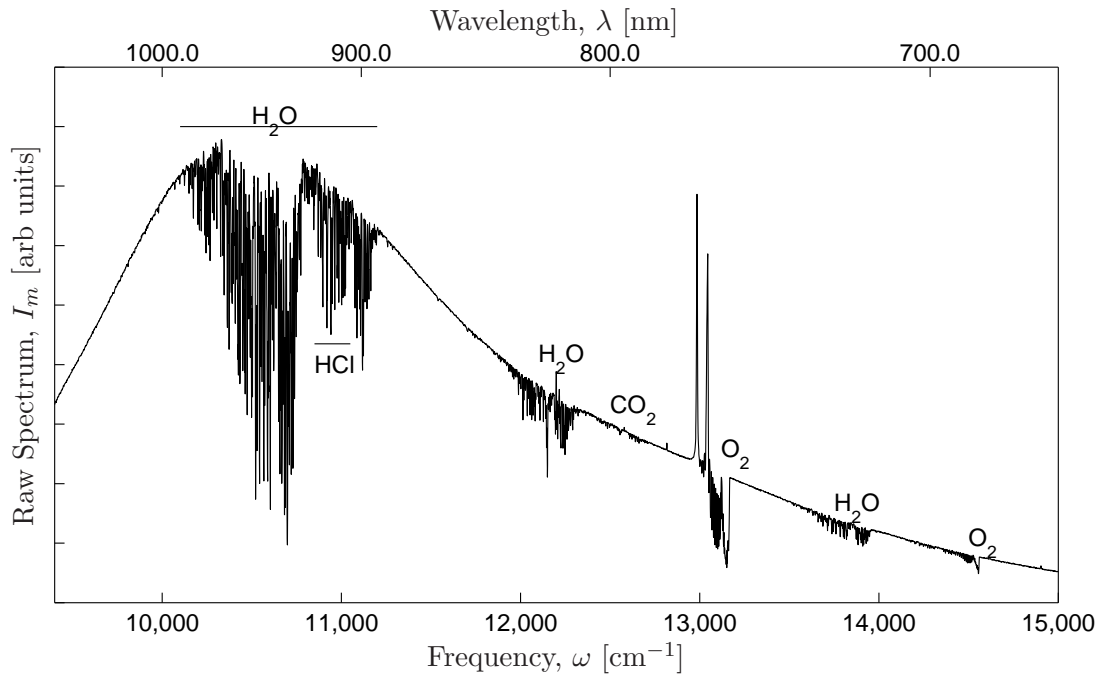
Figure 3.9: Top: single raw spectrum from SRM test, with major absorption bands identified. Bottom: the $O_2(0 \to 0)$ band region for all ten measurements, showing the large potassium emission doublet.

42
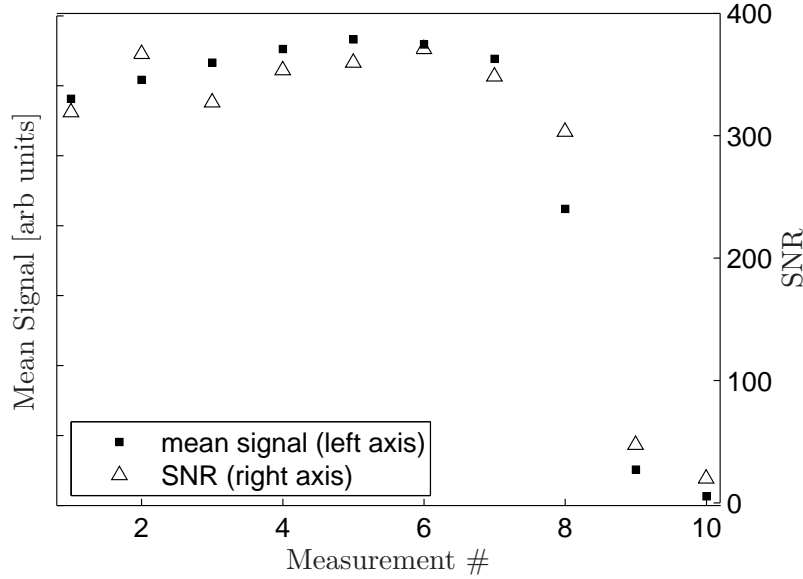
Figure 3.10: Average signal level ($\blacksquare$) and SNR ($\triangle$) of each measurement in SRM test. Average is over full spectrum (8,500-15,000 cm^{-1}).

techniques for estimating absorption in the presence of this emission will be discussed in Chapter IV. The other major absorption bands are also labelled in this plot. Note the second O$_2$ band (the $X(v'' = 0) \rightarrow b(v' = 1)$ band) around 14,500 cm^{-1} that might also be used in ranging. This band is weaker than the $v'' = 0 \rightarrow v' = 0$ band, which may be advantageous at extreme ranges to avoid saturation. The red end of this band does overlap slightly with a weak H$_2$O absorption band that is not noticeable on the scale of this plot, which would complicate analysis.

Figure 3.10 shows the time variation of the overall signal level and the SNR (computed as before). From the signal level, it would appear that motor burnout may have occurred during the integration time of the 8th measurement, but the SNR of the eighth measurement is still quite high. When normalized by the mean signal level, the first eight spectra are nearly identical; the differences are most likely noise driven. It is therefore assumed that these eight are independent realizations of the same signal. The last two measurements however are post-burnout and will not be used in the processing that follows.

43

3.4   Summary

The results of these experiments will be presented in Chapter V. Before the details of range estimation can be discussed, however, more information about how the metric curves are computed from the data must be presented in Chapter IV.

IV. Models

Section 2.5 presented a review of band models from a theoretical standpoint. This chapter now presents in detail the model that will be used to represent the O$_2$(X→b) band. First, section 1 will present a proposed extension of the existing theory developed for this project. Section 2 then describes the details of the process used to select the best model. Section 3 discusses the results of the band model evaluations and the equation that will be used to fit the data. Finally, Section 4 discusses some alterations to the technique needed for some targets.

4.1   Extending Band Models to inhomogeneous paths

The band models in section 2.5 are written to describe the shape of $\bar{A}$ vs u curves, but curves of $\bar{A}$ vs path length, L, would be more useful. In order to do that, it is necessary to first develop an equation for $u(L)$. Because altitude z is the most important factor in determining concentration, the first step is to develop an expression for $z(L)$, altitude as a function of distance along the line of sight. This is then combined with an exponential atmosphere to arrive at an equation for $u(L)$.

4.1.1   Height above ground.   Many approximations presented in the literature assume a flat Earth to simplify computations [32]. For many applications the error induced by neglecting Earth curvature is negligible. For example, the error is less than 0.1% for zenith angles up to 70°, for aircraft of any altitude. In ballistic missile tracking scenarios, however, the minimum height often occurs at a tangent point between the sensor and target. This is illustrated in Figure 4.1. For these long, nearly-horizontal paths, a solution that includes the effects of Earth curvature will be necessary.

Height above ground, z, as a function of distance along the line of sight, ℓ, can be found exactly from the Law of Cosines as

$$z(\ell) = \sqrt{\ell^2 + r_o^2 - 2\ell(r_o)\cos(\pi - \theta)} - R_E, \tag{4.1}$$

45
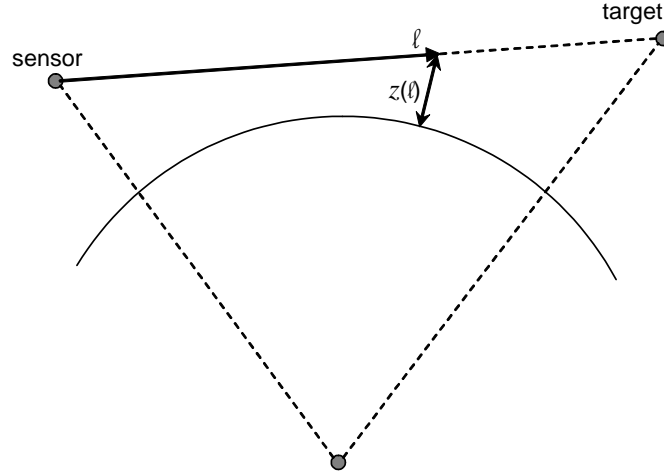
Figure 4.1:   Height above ground as a function of distance along the line of sight, $z(\ell)$.

where R_E is the radius of the Earth, θ is the zenith angle, and r_o is the height of the sensor relative to Earth center ($r_o = z_o + R_E$) as depicted in Figure 4.2.

This solution is exact but inconvenient. It is tempting to use small-angle approximations or series expansions to find a simpler approximate solution, but in the end, these simplify to the same result as assuming a flat-Earth, $z(\ell) \simeq z_o + \ell \cos\theta$.

An original alternative that preserves the effect of a curved Earth was developed for this project. To begin, define the target/Earth-center/sensor angle, β,

$$\tan\beta = \frac{\ell\sin\theta}{r_o + \ell\cos\theta}. \tag{4.2}$$

Since β will be less than about $4°$ for all cases of operational interest and $r_o \gg \ell\cos\theta$, this can be written as

$$\beta \simeq \frac{\ell\sin\theta}{r_o}. \tag{4.3}$$

Now the height above the Earth (assuming a spherical Earth) can be found by defining the segments $z(\ell) = \overline{CD} + \overline{DE} = \overline{OD} - \overline{OC} + \overline{DE}$.

$$\overline{OD} = R_E/\cos\beta \qquad \overline{OC} = R_E \qquad \overline{DE} = (z_o + \ell\cos\theta)/\cos\beta. \tag{4.4}$$

46
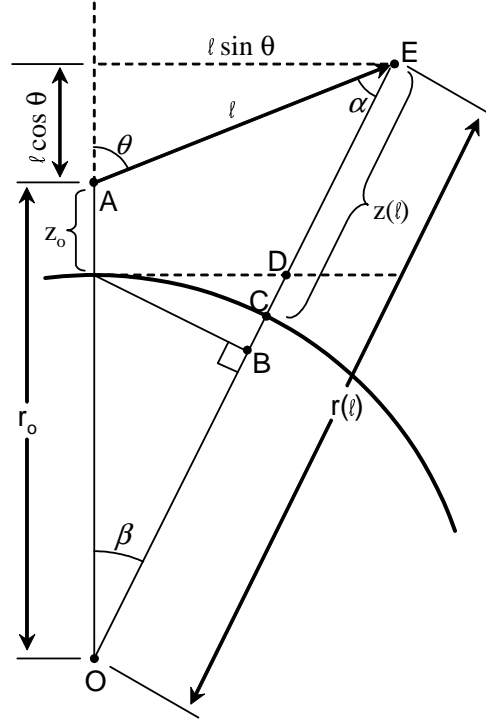
Figure 4.2: Engagement geometry used to account for effects of Earth curvature. The sensor is at Point A and the source at Point E.

So

$$z(\ell) = R_E \left(\frac{1}{\cos \beta} - 1 \right) + \frac{z_o + \ell \cos \theta}{\cos \beta}. \tag{4.5}$$

Note that for small angles,

$$\frac{1 - \cos x}{\cos x} \simeq \frac{1}{2} x^2, \tag{4.6}$$

and $\cos x \simeq 1$, so

$$z(\ell) \simeq z_o + \ell \cos \theta + \frac{1}{2} R_E \beta^2 \simeq z_o + \ell \cos \theta + \frac{(\ell \sin \theta)^2}{2 R_E}. \tag{4.7}$$

This result was numerically compared with the exact solution (from eqn 4.1). An example is shown in Figure 4.3. The errors induced by the approximations in this development are found to generally be less than the errors inherent to assuming the Earth is a perfect sphere.

47
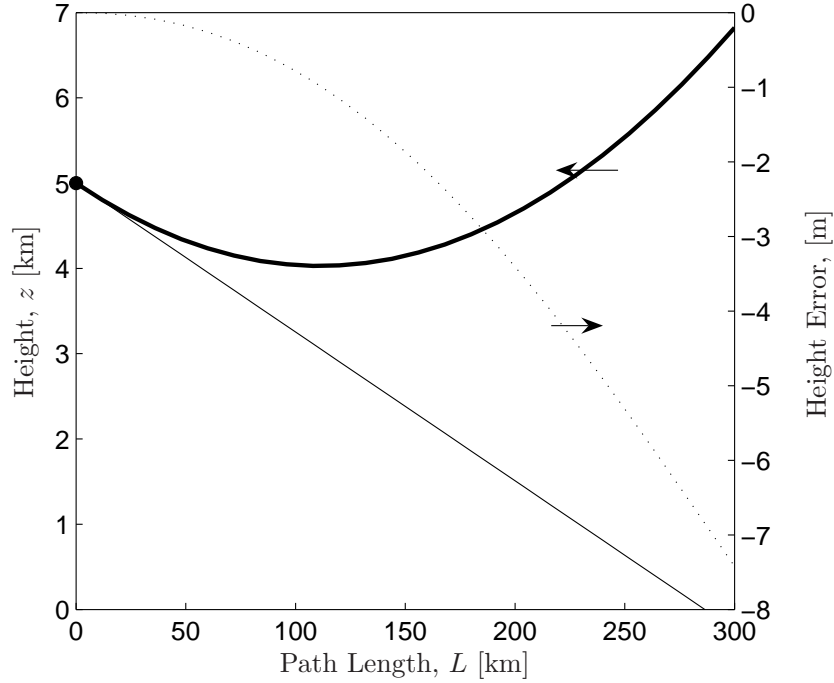
Figure 4.3:   Height above ground as a function of distance along LOS for a sensor at altitude 5 km looking at a zenith angle of 91°. The heavy line (—) shows the height calculated by equation (4.7). For comparison, the height calculated using a flat-Earth assumption is also shown (–), and the height error (relative to the solution from eqn (4.1)) is plotted on the right side axis (⋯).

4.1.2   Concentration as a function of distance along LOS.   The exact atmospheric profile can be very complicated and difficult to describe mathematically. An exponential atmosphere, however, is very simple and a decent approximation. Begin by assuming that concentration of oxygen molecules decays exponentially with height,

$$N(z) = N_o \exp\left(-\frac{z}{H}\right), \tag{4.8}$$

where H is the scale height of the atmosphere and N_o is the sea-level concentration. Note that using an exponential profile with a constant scale height is equivalent to assuming a constant temperature, and the scale height $H = a_o t$. This is common practice in computing band-models for non-homogeneous paths [17, 22].

48

Using equation 4.7 for $z(\ell)$, the total concentration length is

$$m = \int_0^L N(\ell)d\ell = N_o \int_0^L \exp\left[-\frac{1}{H}\left(z_o + \ell\cos\theta + \frac{(\ell\sin\theta)^2}{2R_E}\right)\right]d\ell. \qquad (4.9)$$

By analogy with the homogeneous case where $m = NL$, this equation can be written as a product of sea-level concentration, N_o, with an equivalent path length, Λ, defined as

$$\Lambda = e^{-z_o/H}\int_0^L \exp\left[-\left(a^2\ell^2 + b\ell\right)\right]d\ell, \qquad (4.10)$$

where $a = \sin\theta/\sqrt{2HR_E}$ and $b = \cos\theta/H$. The series expansion of e^{x^2} is used to rewrite this as

$$\begin{aligned}
\Lambda &= e^{-z_o/H}\int_0^L e^{-b\ell}\sum_{k=0}^{\infty}(-1)^k\frac{(a\ell)^{2k}}{k!}d\ell \qquad (4.11)\\
&= e^{-z_o/H}\sum_{k=0}^{\infty}\left[\frac{(-1)^k}{k!}\int_0^L e^{-b\ell}(a\ell)^{2k}d\ell\right].
\end{aligned}$$

Now let $\xi = b\ell$, so that

$$\Lambda = e^{-z_o/H}\sum_{k=0}^{\infty}\left[\frac{(-1)^k}{k!}\frac{a^{2k}}{b^{2k+1}}\int_0^{bL}e^{-\xi}\xi^{2k}d\xi\right]. \qquad (4.12)$$

This can be abbreviated by recognizing the integral as an incomplete gamma function, γ [3, 18], or

$$\Lambda = e^{-z_o/H}\sum_{k=0}^{\infty}\left[\frac{(-1)^k}{k!}\frac{a^{2k}}{b^{2k+1}}\gamma(2k+1, bL)\right]. \qquad (4.13)$$

This form of the equation may appear more cumbersome than equation (4.10), but is better suited to numerical solution. In addition, for many scenarios, the first term of the sum is all that is needed. For $k = 0$,

$$\gamma(1, x) = \int_0^x e^{-\xi}\xi^0 d\xi = 1 - e^{-x}, \qquad (4.14)$$

49

so equation (4.13) (and equation (4.9)) is well approximated by

$$m = N_o e^{-z_o/H} \left(\frac{1 - e^{-bL}}{b} \right) \qquad (4.15)$$

for low zenith angles or short paths.

For scenarios with longer ranges or higher angles, more terms will be needed. A practical limit of 500 km was assumed to be the longest range of interest, error can be kept below 0.1% for all cases by using the first 11 terms in the series. An 11 term series lacks elegance, but numerically it is quick to compute and lends itself to optimization (for fitting to curves) better than the integral form of the expression. The conditions under which fewer terms can be used will be discussed in more detail below.

Equation (4.13) is based on several approximations of varying validity. It is important to point out that the intent here is not to get an exact description of the atmosphere. This equation will be used to introduce some information about how u varies along the path into the band model equations. By leaving parameters (such as H) as adjustable fit parameters, the values that *describe* the data will be found rather than attempting to *predict* it. As will be seen below, this information about the structure of the atmosphere does improve the quality of the fits.

4.2   Band Model Evaluation Methods

All of the band model equations presented in section 2.5 were evaluated based on their ability to describe the behavior of the O_2 band. This was done by preparing plots of $\bar{A}$ vs L from FASCODE predictions and fitting each equation to the plots.

Before discussing the results of these numerical evaluations, the subsections that follow first cover a few details about choices made in establishing a test methodology.

4.2.1   Range Sampling.   In order to ensure a fair comparison of all functions, it is important to first make sure the curves are properly prepared. In general, $\bar{A}$ should be sampled more closely in regions where it is changing rapidly (*i.e.*, in regions

50

where the air is most dense), but these regions occur at different ranges for each scenario. For example, at very low zenith angles, the line of sight quickly "leaves" the atmosphere, making $\bar{A}$ nearly constant at long ranges. For other cases (θ just slightly greater than 90°), the path can continue through relatively dense air for hundreds of kilometers. It was decided to choose the range sampling points (ranges at which FASCODE was executed and $\bar{A}$ computed to generate one point on the curve) based on the geometry of each different scenario, rather than sampling the same points for all cases. This section describes the process of assigning range sampling grids.

For each case (sensor altitude and zenith angle), a maximum range was selected. First, it was assumed that ranges greater than 500 km would not be practical due to signal limitations, and that the atmosphere becomes too thin to be useful for ranging at altitudes greater than 80 km (where N is roughly e^{-10} times the sea-level concentration). For up-looking cases ($\theta < 90°$), the maximum range was chosen as either 500 km or the range at which the height above ground exceeds 80 km, whichever is shorter. For down-looking cases, the maximum range was either 500 km or 90% of the geometric distance to the Earth's surface. The actual line of sight will be refracted, so the true path length will be less than the geometric distance. The factor of 0.9 was used as a "safety margin" to avoid modelling negative altitudes in FASCODE. Figure 4.4 shows the maximum ranges used.

Once the maximum range was selected, N range sample points were defined. Because the absorption changes more rapidly at short range, it is helpful to sample short ranges more closely than long ranges. Range points were defined as follows:

$$R_i = R_{i-1} + i\delta_R \qquad \delta_R = \frac{R_{max}}{\sum_{i=1}^{N} i}. \qquad (4.16)$$

The step size δ_R is defined such that $R_N = R_{max}$. For the basis of comparison, $N=30$ sample points was used for all cases. FASCODE was run at each of these 30 ranges, and $\bar{A}$ was computed from the predicted transmission curve (again using the
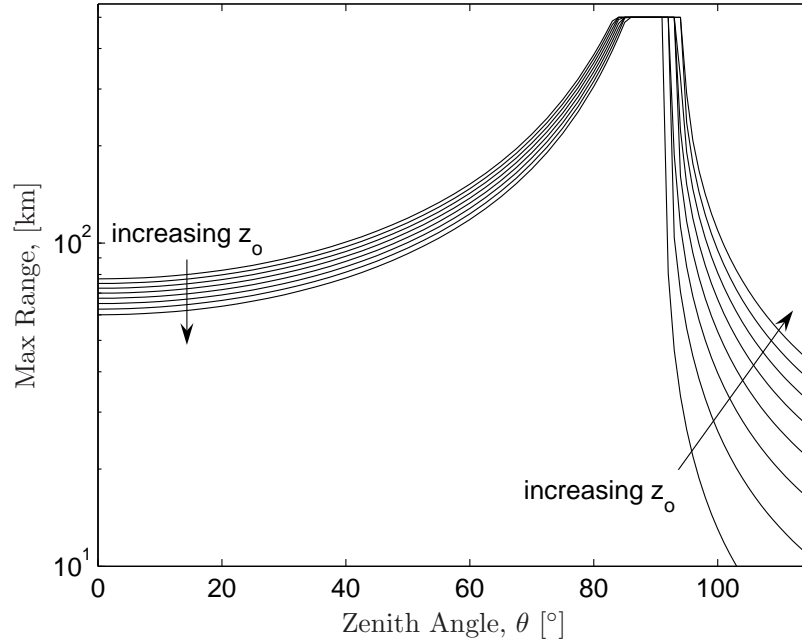
Figure 4.4: Maximum range used in FASCODE calculations as a function of zenith angle. Contours are for different values of sensor altitude from 2.5 km to 20 km in increments of 2.5 km.

band from 12,900-13,200 cm^{-1}) to establish a plot of $\bar{A}$ vs L. Figure 4.5 shows some representative curves defined in this manor.

4.2.2 Testing non-homogenous atmosphere extension. As previously discussed, the band model equations, as defined above, are intended to describe the shape of $\bar{A}$ vs u curves. To correct for this, equation (4.9) or (4.13) can be used. In order to assess the validity and utility of these equations, fits were performed using two different approaches. In using the functions as defined in section 2.5, the structure of the atmosphere is neglected, which is equivalent to assuming $u = (SN_o/2\pi\alpha)L$. Some of these functions were then used again with $u = (SN_o/2\pi\alpha)\Lambda$ where the atmospheric scale height, H (used in computing Λ) is treated as a free fit parameter.

While equations (4.9) and (4.13) are approximations, adding additional information about the structure of the atmosphere and about the engagement geometry (z_o and θ) should improve the quality of the fit. Of course, adding degrees of freedom will generally improve the quality of the fit, whether the equation is any better model

52
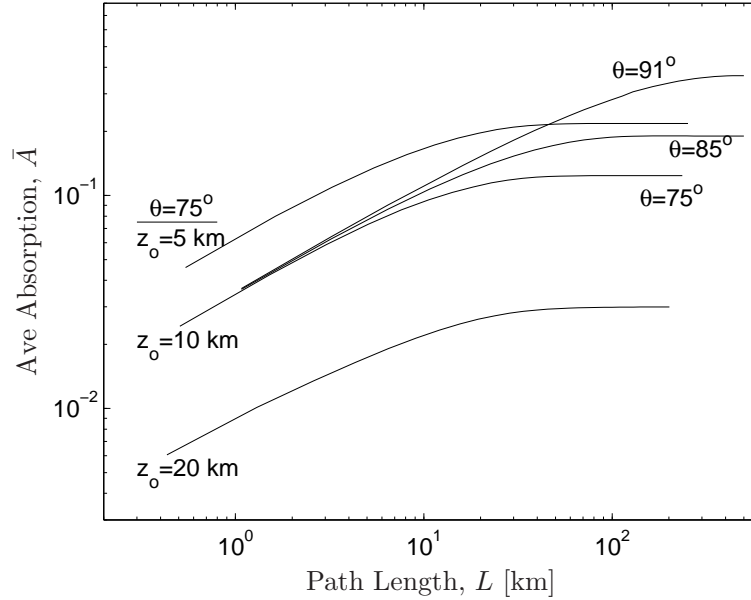
Figure 4.5: $\bar{A}$ as a function of L curves for the five cases used in evaluating fit functions in TableCurve.

or not. F-Stat, which accounts for the number of degrees of freedom, is ,therefore, used as the basis of comparison. An improvement in F-Stat can be interpreted as meaning the equation is a better model of reality.

4.2.3 Series Approximation in Λ.   Equation (4.13) calls for an infinite sum, which of course cannot be executed numerically. As previously noted, only the first 11 terms of the series are required to keep errors (between the truncated series of equation (4.13) and the full integral solution of equation (4.10)) below 0.1% for all cases below 500 km. The numerical evaluations also tested the possibility of speeding the computation time by using fewer terms where possible. This section describes the process by which the number of terms was selected for each case.

As mentioned before, the number of terms required in the series for equation (4.13) depends on the range, sensor altitude and the zenith angle. The error introduced by truncating the series is always greater at longer ranges, so the maximum range (see §4.2.1) is used to establish an upper limit on error as a function of zenith angle alone.

53
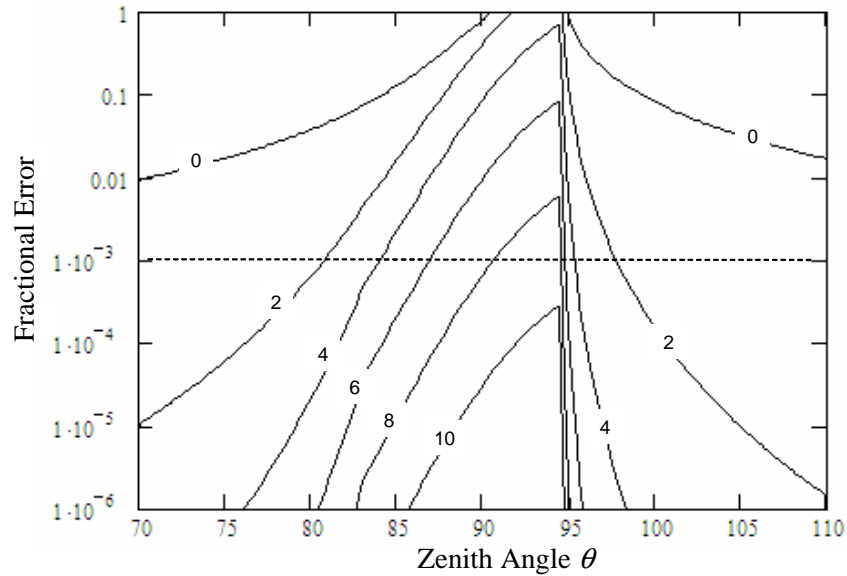
Figure 4.6:   Maximum fractional error in Λ caused by truncating the series (compared to integral form). Labels indicate the highest term included in the series.

Figure 4.6 shows the maximum fractional error in Λ introduced by truncating the series. Each curve is for a different number of terms. This plot was used to define regions over which a lower number of terms can be used without exceeding 0.1% error. These regions are listed in Table 4.1. Not surprisingly, more terms are needed for cases in which the sensor is pointed just below horizontal, where the paths are longer, denser, and more complicated than up-looking cases.

4.3   Band Model Selection

This section presents the results of the numerical evaluations described in the previous section. First, TableCurve was used to quickly compare a broad range of fit functions (based on the band models of Chapter II). The most promising models in this quick comparison were examined in more detail in MatLab to select the model that best describes the $O_2(X\rightarrow b)$ band over a broad range of conditions. Lastly, modifications to this model were explored. Each step in this process is discussed in the following subsections.

54

Table 4.1:   *Regions definitions to keep maximum fractional error below 0.1% (from Figure 4.6).*

For Zenith Angles:			Highest Term Needed:
$\theta < 40°$	or	$> 150°$	$k = 0$
$< 75°$	or	$> 105°$	1
$< 80°$	or	$> 98°$	2
$< 82.5°$	or	$> 96°$	3
$< 83.5°$	or	$> 95.5°$	4
$< 85.0°$	or	$> 95.0°$	5
$< 86.5°$	or	$> 94.8°$	6
$< 88.5°$	or	$> 94.7°$	7
$< 90.5°$	or	$> 94.6°$	8
$< 93.5°$	or	$> 94.5°$	9
otherwise			10

4.3.1   TableCurve Fit Results.   Initial evaluation was based on plots computed for the five different cases shown in Figure 4.5, all of which assumed a U.S. Standard Atmosphere. For one sensor altitude ($z_o = 10$ km), three different zenith angles were compared ($\theta = 75, 85, 91°$). Then for one zenith angle ($\theta = 75°$), three different altitudes were compared ($z_o = 5, 10, 20$ km). Table 4.2 summarizes the fit quality (F-Stat) for each case. A modified version of Beer's Law, $A = c_1(1 - \exp(-c_2 L))$, is included here as a baseline for comparison. Figure 4.7 shows one example FASCODE metric curve along with the best-fit curves generated by each function.

The fit quality is somewhat dependent upon the initial values for the first iteration of optimization. The starting values were adjusted somewhat from case to case, but are the same for all functions in each case. The fit parameters are

$$c_1 = SN_o/2\pi\alpha \qquad c_2 = \pi^{3/2}\alpha/\delta \qquad c_3 = C \qquad c_4 = H, \qquad (4.17)$$

where C is a simple scalar. The first two coefficients are common to all band models (although they have a different meaning for Beer's Law); parameters 3 and 4 are used as needed. The second column of Table 4.2 specifies the number of parameters for each function. The definitions of c_2 for some cases vary by a multiplicative constant as appropriate to the band model equations of Chapter II.

55

Table 4.2:   *Goodness of fits (F-Stat) from TableCurve. (-) indicates cases for which the optimization failed to converge.*

Equation	parameter count	Case (z_o and θ) 5 km 75°	10 km 75°	20 km 75°	10 km 85°	10 km 91°	Remarks
Beer's Law	2	648	726	458	657	581	$c_1(1-\exp(-c_2 x))$
Simple Models:							
2.23	2	-	-	-	-	56	isolated Lorentzian
2.24	2	-	-	-	-	-	isolated Doppler
2.26	2	-	-	-	-	72	Elsasser
2.27	2	-	-	-	-	72	Elsasser ($y \ll 1$)
2.32	2	-	-	-	-	56	Exponential Dist.
2.33	2	-	-	-	-	53	Godson Distribution
2.34	2	-	-	-	-	55	Malkmus Distribution
Models with multiplicative constant included:							
2.26xC	3	4.5E5	3.2E5	-	1.9E5	7.7E4	
2.27xC	3	4.5E5	3.2E5	-	1.9E5	7.7E4	much faster than 2.26
Random Models (2.35)/(2.36) with the following for $\bar{A}(line/band)$:							
2.23	2	-	-	-	-	-	
2.24	2	85	93	101	95	-	
2.23xC	3	1.9E3	1.8E3	-	1.7E3	3.0E3	
(2.26xC)	3	1.2E5	8.2E4	-	5.0E4	2.0E4	$1-\exp(-C\bar{A}(band))$
2.26xC	3	6.1E3	4.7E3	1.1E4	4.4E3	6.4E3	$C[1-\exp(-\bar{A}(band))]$
(2.27xC)	3	1.2E5	-	1.3E4	5.0E4	2.0E4	
Models with adjustable atmospheric parameters:							
2.23	3	-	621	-	1.1E3	154	
2.27	3	3.5E3	3.8E3	1.6E3	7.1E4	3.3E4	
2.27xC	4	2.1E5	1.2E5	2.4E4	2.4E4	5.5E4	
2.35/2.27xC	4	7.1E4	1.8E5	2.7E4	2.6E5	1.4E5	
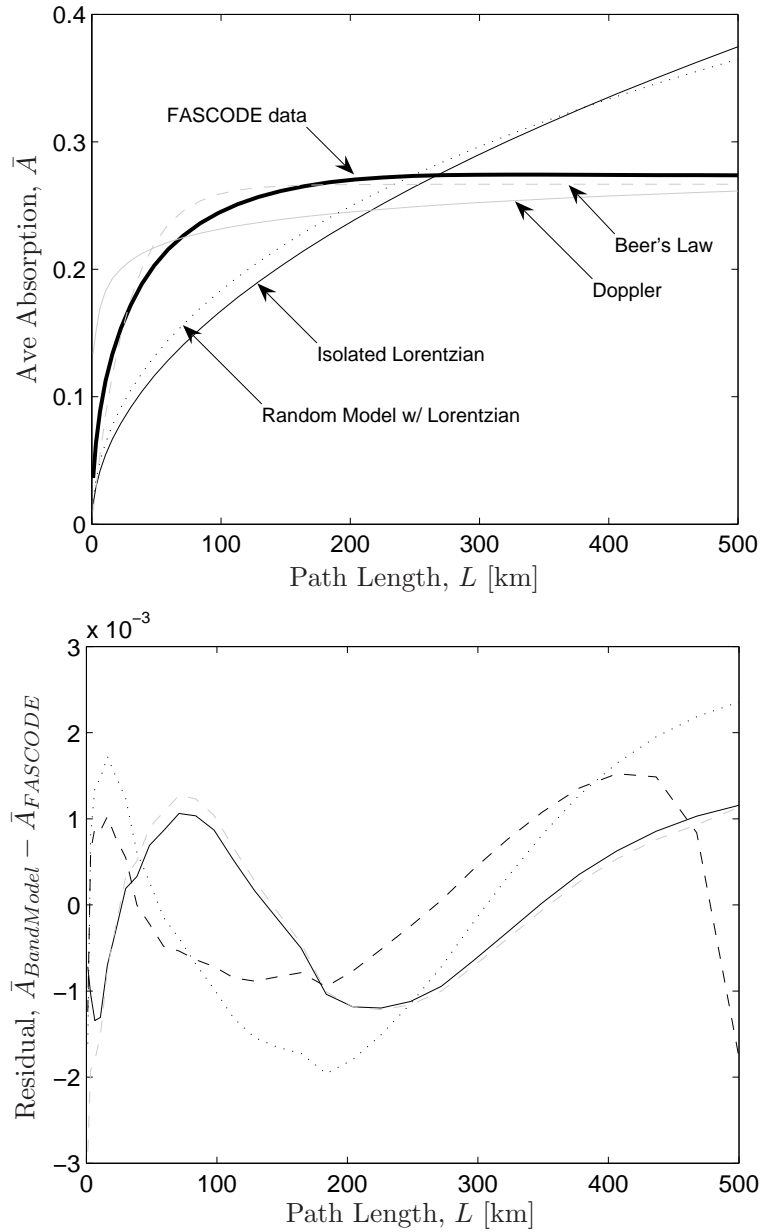
Figure 4.7: Sample best-fit curves, fit to FASCODE data for a sensor at 10km altitude and a zenith angle of 89°. *Top*: not shown here for clarity are the Random Doppler (which falls near the isolated Doppler); the Distribution Models and the unscaled Elsasser Models all fall between the two Lorentzian curves; the scaled Elsasser models fall within the width of the data line. *Bottom* : Residual error in between FASCODE data and the Elsasser model (——), Elsasser in sparse-line limit $(- - -)$, random Elsasser model $(\cdots)$ and random Elsasser using $\Lambda(L)$ modification (- - -). All models in lower plot are modified to include scaling constant C.

57

A few things in this table are worth comment. First, these results show that it is necessary to introduce the arbitrary constant, C, into most fit functions in order to get a good fit (or to converge to any solution at all). Examination of the band model equations shows that they all have possible values ranging from 0 to 1, as should be expected for models of absorption. The computed values for $\bar{A}$, however, do not approach one for most cases. One possible reason for this is related to the structure of the atmosphere. In order for $\bar{A}$ to reach 1, the entire band must saturate–even at frequencies between lines where the cross-section is quite low. This would require a very large number of absorbers. The curves computed for atmospheric paths level off at values that are determined more by the concentration length than by true saturation–as paths grow longer they leave the atmosphere before they saturate. As a result, the magnitude of the curves is artificially reduced even though the general shape is still very similar to the band model equations. The constant, c_3, compensates for this as well as any other effects that might prevent the band from truly saturating.

Secondly, many of these models are actually worse than Beer's Law in terms of being able to describe the data. This version of Beer's Law has a multiplicative constant added, which may explain part of that. Notice also that Beer's Law is mathematically equivalent to a random model where $\bar{A}$(isolatedline) is linear with L.

Thirdly, an examination of the last four rows shows that, as expected, adding information about the atmosphere does generally improve the quality of the fit. There are a few exceptions to this. Specifically, fits for equations with the arbitrary constant c_3 (equations (2.27) and (2.35)) are actually made worse in some cases by the "improvement" of using equation (4.9) to define $u(L)$. It should be noted, however, that these fits are better in terms of r^2 or mean error. The lower value of F-Stat indicates that the improvement in r^2 is less than one would expect if all of the parameters were independent. This is reasonable given the physical interpretation of c_3 hypothesized above.

Finally, the Elsasser band model (equations (2.26) and (2.27)) is consistently better than the alternatives, whether used as part of a random model, with a mul-

58

tiplicative constant, or on its own. This may be in part because of the extra fit coefficient, c_3, in these equations (it is redundant with c_2 in the other equations). Even without the free parameter, though, it still appears to fit better. Take, for example, the first two models in the bottom section of Table 4.2 or the few cases in the top section that converged to a solution. The difference between the results of the two Elsasser models is minor, but the separated-line limit version is much faster to compute. For cases where only one or the other of the two Elsasser models is shown on the table, the results for the other model are similar.

Based on the results in Table 4.2, the most promising functions for closer evaluation are:

$$\text{Elsasser Band Model}: \quad \bar{A} = c_3 \text{erf}[c_2 \mathcal{L}(c_1 L)] \tag{4.18}$$

$$\text{Random Band Model}: \quad \bar{A} = 1 - \exp\{-c_3 \text{erf}(c_2 \mathcal{L}(c_1 L))\} \tag{4.19}$$

$$\text{Random Band + inhom. atm.}: \quad \bar{A} = 1 - \exp\{-c_3 \text{erf}[c_2 \mathcal{L}(c_1 \Lambda)]\}, \tag{4.20}$$

where Λ is a function of the engagement geometry parameters, z_o and θ, which are assumed to be known, and the atmospheric scale height, H, which is an adjustable parameter. This can be computed using either equation (4.9) or (4.13), for a total of four different equations to compare in more detail using MatLab.

4.3.2 MatLab Fit Results. MatLab was used to compare fit quality (this time based on the mean squared error between FASCODE data and best fit line) for equations (4.18)-(4.20). At the same time, two different methods for computing Λ (equations (4.9) and (4.13)) for use in equation (4.20) were also compared. These functions were fit to a standard set of 21 different cases (seven zenith angles from 30 to 95° and three sensor altitudes from 5 to 20 km). For each case, plots of $\bar{A}$ vs L were prepared as discussed in the previous section. The same initial values of fit parameters, convergence criteria, maximum number of iterations, and other internal

59
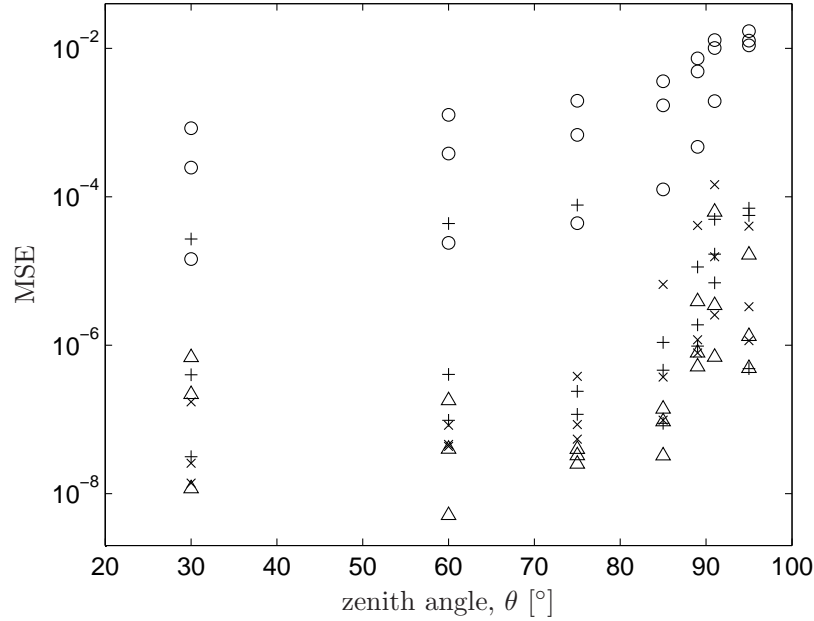
Figure 4.8: MatLab fit results for 21 different cases to compare equations. $\times$ = equation (4.18); $+$ = equation (4.19); $\circ$ = equations (4.20) and (4.9); $\triangle$ = equations (4.20) and (4.13).

optimization settings were used for all functions and all cases. The results are shown in Figure 4.8.

From Figure 4.8 it is clear that the combination of equation (4.20) with equation (4.13) to compute Λ is the lowest error in most cases used in this comparison. Of the cases in which a different equation was a better fit, this model was always at least a close second, and no pattern was evident to generalize or predict when another function might be better.

It is somewhat interesting that the series approximation (equation (4.13)) performs better than the integral form (equation (4.9)), which is exact. For a given set of parameters, the two algorithms compute the same concentration length to within 0.1%. In fitting, however, MatLab appears to have trouble optimizing the integral. This may be related to the sampling grid used in numeric evaluation of the integral.

4.3.3 Modifications.   With this band model chosen as the primary model to represent the $O_2(b \leftarrow X)$ band, its behavior should now be examined more closely.
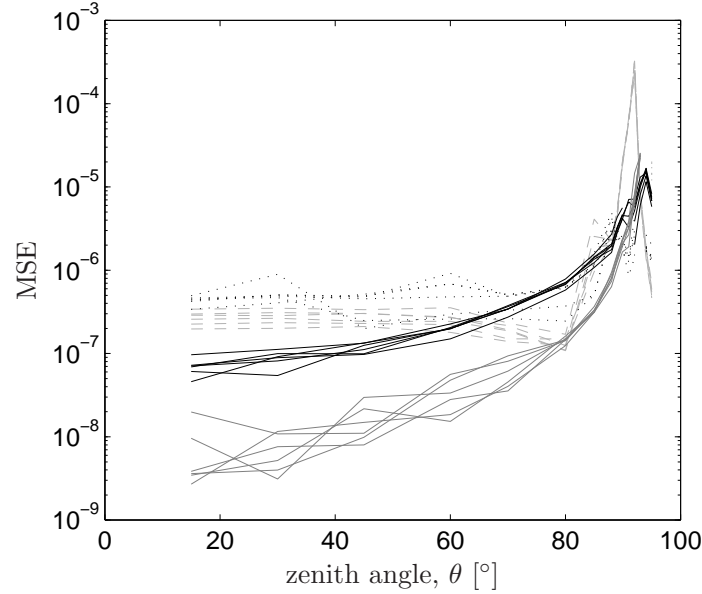
Figure 4.9:   Fit errors for the selected fit function (equations (4.20) and (4.13)) for more test cases. The dashed (- -) line is for $z_0 = 5$ km; dotted ($\cdots$) is for $z_o = 10$ km; solid black (–) is $z_0 = 15$ km; solid gray (–) is $z_o = 20$ km. The six lines of each style are computed for the six different standard atmospheres defined within FASCODE.

Figure 4.9 shows plots of MSE, similar to Figure 4.8, but for a broader range of cases. Figure 4.10 shows the optimized values of the fit parameters.

While the error is very low, the fit parameters are less well-behaved. For a physics-based model, one would expect the fit parameters to be smooth and pre-dictable functions. There are a few possible explanations why this is not the case. It is possible that by choosing the initial parameter values or the internal optimization settings (tolerance, number of iterations, etc) these plots could be cleaned up a bit. It is also possible that the problem is under-constrained. If the fit parameters are not independent, then there may be multiple sets of parameter values that are all equiv-alent, and the optimization stops as soon as it finds one of them–possibly a different one for each case.

A closer examination of the fit parameter definitions suggests that this may well be the case. Recall in the definitions of the fit parameters,

61
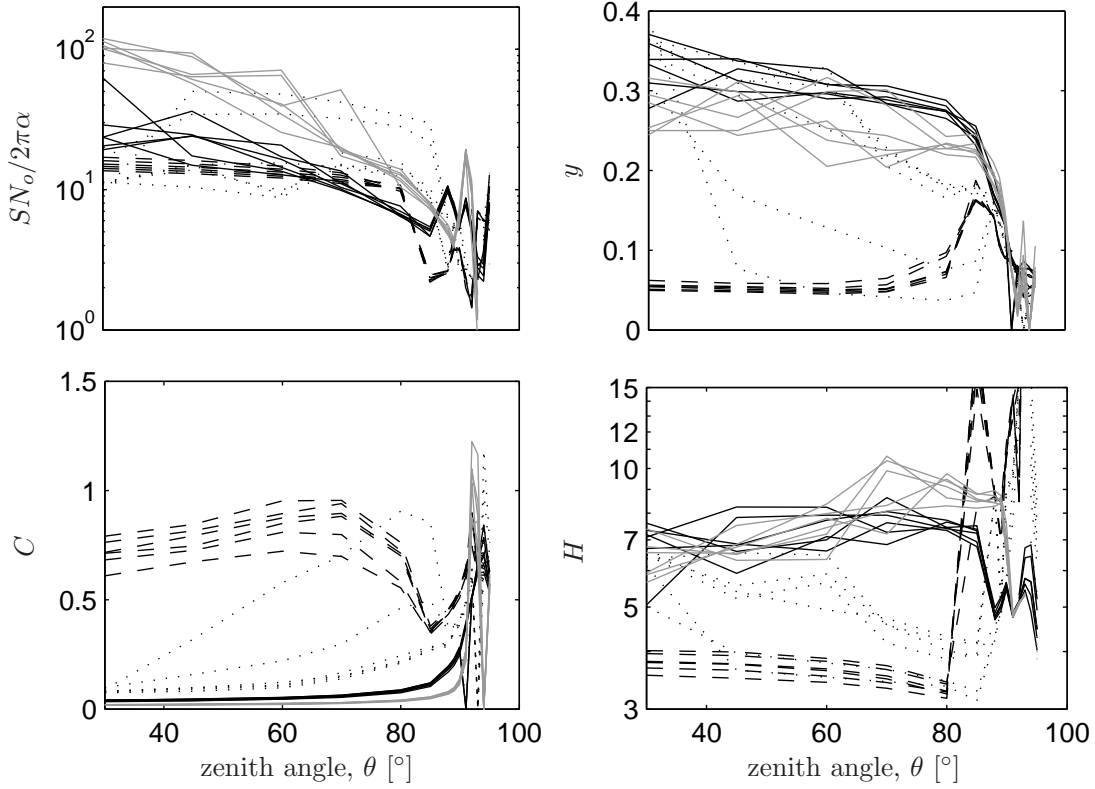
Figure 4.10:   Optimized fit coefficients for eqn (4.20) (with eqn (4.13)
for Λ). As in Figure 4.9, line styles indicate sensor altitude: $(- -) = 5$
km; $(\cdots) = 10$ km; $(-) =15$ km; $(-) =20$ km. The behavior of these
curves suggests the optimization may be under-constrained.

$$c_1 = \frac{SN_o}{2\pi\alpha} \qquad c_2 = \pi^{3/2}\frac{\alpha}{\delta}, \qquad\qquad [4.17]$$

the factor of α is common to both terms. Furthermore, the value of average line spac-
ing, δ, is not expected to change. It was initially left as a free parameter to find
the value that best describes the data (recall that the band *model* parameters are
not required to match the parameters for the actual band), but there is no reason
to expect δ to change from case to case. It is, therefore, reasonable to expect that
the first two fit parameters may not be independent. Similarly, the arbitrary scaling
parameter C may be redundant with the scale height H, if C is really only needed to
account for the effects of varying density along the path, as hypothesized above.

The band model was re-tested holding various combinations of parameters constant. The error in the resulting fits is shown in Figure 4.11. From this it is apparent that using four fit parameters is the lowest error, but some other versions are not bad. In particular, the error is only slightly larger (and actually smaller in some cases) if the scale height, H, is set equal to 8 km and y is fixed at 0.2, the approximate values at sea-level. The parameter values from this fit are quite well-behaved, as is shown in Figure 4.12.

From Figure 4.12, it is also apparent that zenith angle is the most important parameter, followed by sensor altitude. The six different standard atmosphere models used here represent cases ranging from arctic to tropical, and for temperate zones range from summer through winter. In short, the six different lines plotted here for each case represent a very broad range of conditions, and yet the six lines are clustered very tightly. This result indicates that weather conditions play only a minor role in the values of the fit parameters and therefore in the resulting curves. This supports the earlier assumption of constant temperature (for the sake of writing the exponential atmosphere).

With this result, the **final form of the band model** is

$$\bar{A} = 1 - \exp\left[-c_2 \text{erf}\left(0.2\mathcal{L}(c_1\Lambda)\right)\right],$$

$$\Lambda = \frac{He^{-z_o/H}}{\cos\theta} \sum_{k=0}^{n} \left[\frac{(-1)^k}{k!}(0.025\tan\theta)^{2k}\gamma(2k+1, L\cos\theta/H)\right], \quad (4.21)$$

where H=8km and n can be selected from the zenith angle (see §4.2.3).

The equivalent path length, Λ, can be computed from the engagement geometry factors, θ and z_o, which are assumed to be known quantities for any given set of measurements. The values of Λ at each value of L are then used to define the fitting function, equation (4.21). Because Λ no longer contains any adjustable fit parameters, it would be equivalent to use this equation for Λ to transform the axis of the plot and fit equation (4.21) directly to plots of $\bar{A}$ vs Λ.

63
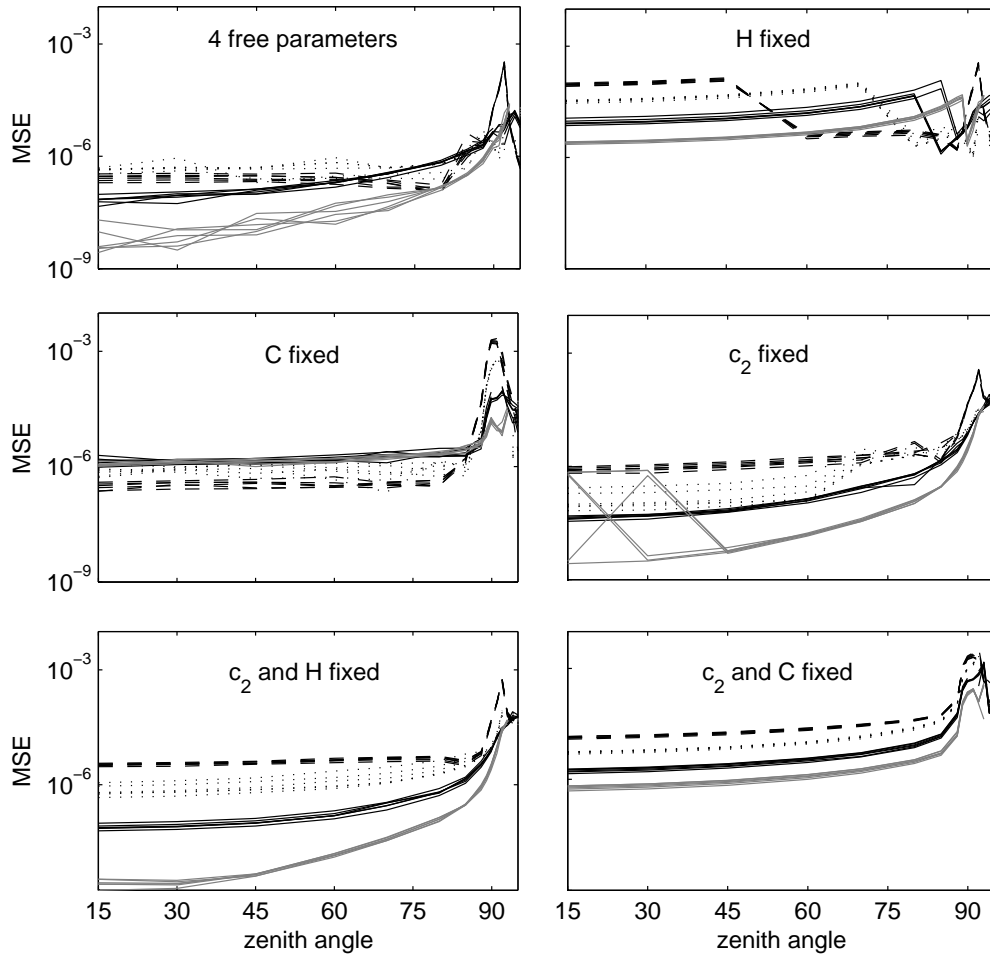
Figure 4.11: Fit error in equation (4.20) (with Λ from equation (4.13)) with different combinations of parameters held fixed. As in Figure 4.9, line styles indicate sensor altitude: $(\text{- -}) = 5$ km; $(\cdots) = 10$ km; $(-) = 15$ km; $(-) = 20$ km.

64
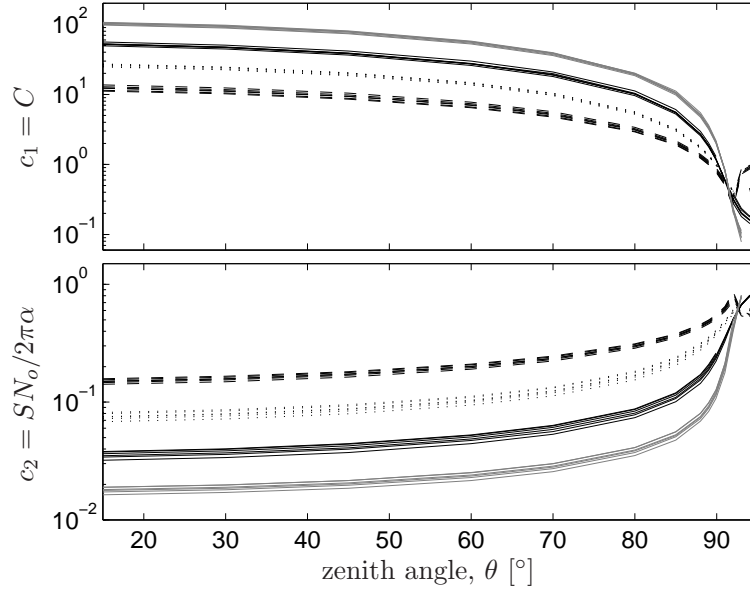
Figure 4.12: Fit coefficients for equation (4.20)+(4.13) with two parameters free and two fixed. As in Fig 4.9, line styles indicate sensor altitude: (- -) = 5 km; (···) = 10 km;(—) =15 km; (–) =20 km.

4.4 Fit Comparison for Modified Metric

One potential problem with using the entire band is the possible contamination of the spectrum by potassium emission, as was seen in Figure 3.9. Potassium is commonly found in solid rocket propellants and emits very strongly on a doublet that is located within the P-Branch of the $O_2(X{\rightarrow}b)$ band. Any emission in the band will confound estimates of absorption. This section presents a modification of the $\bar{A}$ metric that can be used to avoid this problem, and then verifies that the above band model still appropriately describes this new metric.

One could attempt to fit a Lorentzian line to the easily observed peaks of the emission and then subtract this estimated emission from the spectrum prior to averaging. Generally speaking, though, accurate estimation of the wings from observations of the peaks is challenging. Instead, initial results show computing the spectral average over only the R-Branch of the band (13,121 - 13,170 cm^{-1}) offers all the advantages of averaging the entire band, but simply ignores the region of the spectrum that is contaminated by the potassium emission. This is somewhat more susceptible

65

to noise; not only are there fewer channels, but the average absorption is higher in this region, meaning lower signal levels. Using the whole band is still recommended where possible, but for solid rocket motors use of the R-branch only will suffice.

When using only the R-branch, values of $\bar{A}$ are typically higher than for the whole band because the rotational lines are much more closely spaced in the R-branch. As a result, the curves will be different, depending on the choice of bandwidth. The difference is primarily in magnitude; the general shape of the curves are quite similar. Whenever it is necessary to distinguish between the two methods of computing $\bar{A}$, the average over the R-branch alone will be denoted by $\bar{A}_R$, and $\bar{A}_o$ will be used for averages over the entire band.

In addition to having two methods to compute $\bar{A}$, there are also two ways to look at path length: actual length, L, or equivalent length Λ. Figure 4.13 shows a comparison of all four combinations, computed from the same 21 cases (computed by FASCODE) used in section 4.3.2.
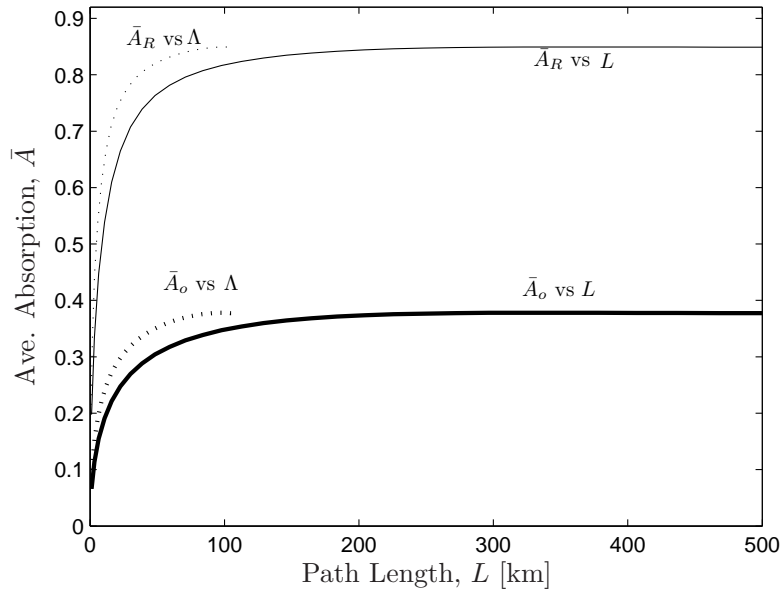
Figure 4.13:   Plots of average absorption as a function of path length for full-band $(\bar{A}_o)$ and half-band $(\bar{A}_R)$ averages. Plots vs equivalent length, Λ are also shown. Curves are from FASCODE data for a sensor at 5km altitude looking at a zenith angle of 89°.

66

Table 4.3:   *Comparison of fit error for the four different classes of curves shown in Figure 4.13. Bold face numbers highlight the best metric for each model.*

Fit Function	MSE Averaged over 21 cases used in fig 4.8			
	$\bar{A}_o$ vs L	$\bar{A}_R$ vs L	$\bar{A}_o$ vs Λ	$\bar{A}_R$ vs Λ
Beer's Law	1.02e-003	4.60e-003	**6.80e-004**	2.57e-003
2.23	2.50e-003	2.08e-002	**8.96e-004**	9.37e-003
2.24	1.64e-003	6.92e-003	**1.53e-003**	7.89e-003
2.33	2.78e-003	2.30e-002	**1.03e-003**	1.05e-002
2.32	2.49e-003	2.07e-002	**8.91e-004**	9.33e-003
2.34	2.50e-003	2.08e-002	**8.95e-004**	9.35e-003
2.26	2.26e-003	8.98e-003	**7.56e-004**	2.41e-003
2.26xC	**1.13e-005**	8.57e-005	1.55e-005	6.86e-005
2.27	2.27e-003	9.04e-003	**7.61e-004**	2.43e-003
2.27xC	**1.23e-005**	7.91e-005	1.41e-005	7.23e-005
2.35/2.23	1.77e-003	5.70e-003	**4.86e-004**	8.71e-004
2.35/2.24	**1.91e-003**	9.88e-003	4.07e-002	5.21e-002
2.35/2.32	1.76e-003	5.62e-003	**4.82e-004**	8.59e-004
2.36/2.26xC	**1.12e-005**	1.01e-004	3.53e-005	6.88e-005
2.36/2.27xC	**1.74e-005**	7.16e-003	3.71e-005	1.05e-004
2.36/2.27xC + 4.9	**4.24e-003**	2.08e-002	4.25e-003	2.08e-002
4.21(11 terms)	**4.36e-006**	1.88e-005	8.22e-006	4.55e-005
4.21(n terms)	**4.44e-006**	1.96e-005	8.22e-006	4.58e-005

Table 4.3 shows the results of fitting the band models introduced in Chapter IV against each of these four types of curves to see if any one version of the metric works better than others. A few things are apparent from this table. First, all models fit to plots of $\bar{A}_o$ better than $\bar{A}_R$. This may be due to some portion of the wings of the low-J lines of the R-branch extending beyond the band cutoff of 13,120 cm^{-1}.

Second, equation (4.21) is the best model, no matter which metric is used. Comparing the results for this equation, which is a modification of the random band model, against the unmodified model (eqns (2.36) and (2.27)) shows the use of Λ in place of L provides a 60% reduction in fit error, on average.

Finally, it is interesting to note which models fit better to plots vs Λ than L. One would expect that simple models that include no correction for atmospheric structure should fit best to plots vs Λ, where models that include that atmosphere

67

should fit plots vs L better. If that is the case, then this table once again supports the hypothesis that the scaling constant C is used to compensate for atmospheric effects, as discussed in section 4.3.1. Given the assumption that C is a correction for atmospheric structure, the only exception to the rule is the randomly spaced Doppler line model (equations (2.35) and (2.24)).

4.5   Summary

This chapter not only presents the details of how the band model was selected, but also develops a novel extension that can be applied to any band model. Comparing band model equations against FASCODE predictions shows the random band model to be more accurate than Beer's Law by almost two orders of magnitude (in terms of average fit error). Use of the modification presented in section 4.1.2 further reduces fit error by about 60%. This modified version of the random band model (eqn 4.21) is the most accurate representation of the O_2 band. This function will not only be used to compute the metric curves used for range extraction in Chapter V, but also to make long-range accuracy predictions in Chapter VI.

V. Experimental Results

With the band model chosen, all the tools are in place to examine the process of estimating range from measurements, as well as the results found from experimental data.

5.1 Range Estimation in Hallway Experiments

As was described in Chapter III, the goal of the third Hallway experiment was to verify the ranging methods described above. Historical data (observations of the same source, with the same instrument, taken on a different day) were used to derive a metric curve of $\bar{A}$ vs L. The new data was then compared with this curve.

The source for this experiment was the QTH lamp. The data used to create the metric curve were taken with the lamp at seven different ranges from about 15 to 50 m. The new observations were taken at a range of 36.6 m (measured from the lamp filament to the entrance pupil of the instrument).

5.1.1 Range Estimation Techniques.   Figure 5.1 shows the results of range estimation. Using raw data, the estimated range was 37.1 ± 2.1 m. The actual range is within the error bars, and the range error is 1.3%. Roughly half of the range uncertainty is caused by uncertainty in measurements of $\bar{A}$; the other half is caused by uncertainty in the best-fit line. Note that the 32 cm^{-1} resolution data was not included when finding the metric curve, for the reasons cited in Chapter III.

This estimate, based on the raw data from the two days, can be further improved by considering a couple of factors. First, the absorption depends on the actual air path length, but the distances reported are measured to the entrance pupil of the instrument. There is another 1.55 m of path length inside the instrument, plus roughly 1.1 m within the NFOV telescope (the exact number changes with focus adjustment). While this factor is common to the measurements from both days, it will cause a slight change in the shape of the metric curve. If a new curve is computed with this

69
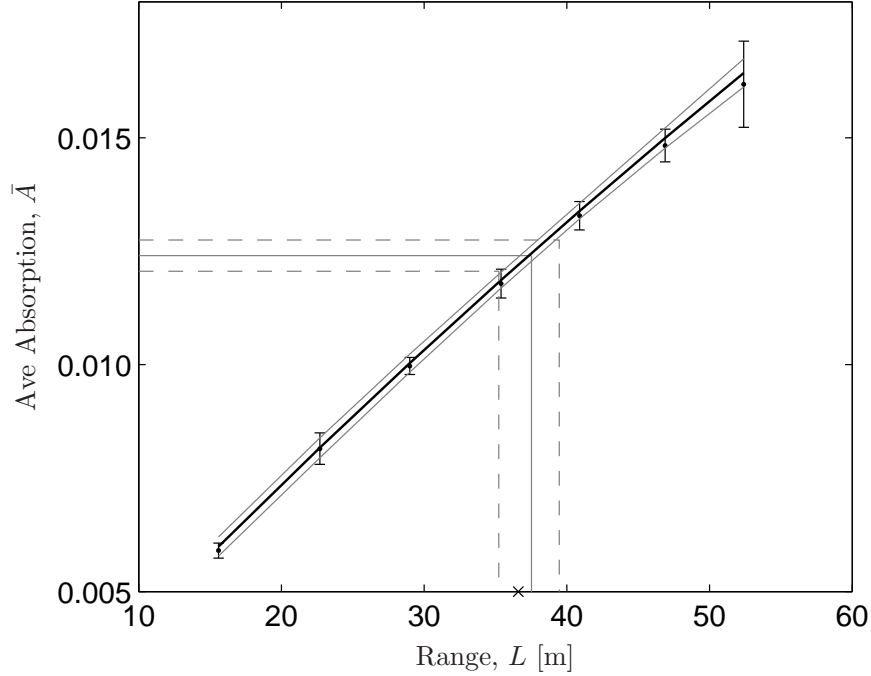
Figure 5.1:   Experimental range estimation results (in raw data). The
points are data from the 16 Sep 2005 experiment; the black line is the
best fit metric curve fit through those points (with 99% confidence
interval); the horizontal gray line is the new data from 22 Sep (mean
± standard deviation over 45 files); the vertical gray line is the range
estimated from the intersection of the new data with the metric curve;
and the × marks the true range to the source.

correction, the range estimate is 40.0±2.1 m. The actual path length must also have
the same adjustment applied, so the actual range is 39.3 m, for an error of 2.1%.

Secondly, the concentration length is more important than the physical dis-
tance. A simple correction can be applied by scaling the distances by a ratio of the
concentrations for the two days. In other words,

$$L' = \frac{N}{N'}L. \tag{5.1}$$

The oxygen concentration can be computed from standard meteorology data using
the ideal gas law (see Appendix B for details). Weather data was taken from Wright-
Patterson base operations, which is roughly 4 miles from where the experiments were
performed. The average oxygen concentration over the course of the data acquisition

70

was 5.09E24 and 5.21E24 molecules/m^3 for the two experiments, respectively. With this correction, the new range estimate is 39.1±2.1 m, or 0.4% error. It is interesting to note that the error here of 15 cm is comparable with the accuracy of the tape measure used to determine the "known" range.

Range estimation was also attempted using metric curves based on Beer's Law, and the random band model (eqn (4.19)). Results are summarized in Table 5.1. In this data, that band model is more accurate than Beer's Law (by about 10%), and use of the inhomogeneous atmosphere modification of section 4.1.2 further improves reduces error by about 50%.

In operational situations, one might not always have the luxury of relevant historical data from which to draw the metric curve. The same methods were applied using FASCODE runs in place of the 16 Sep data. FASCODE was run (with a standard atmosphere, not using the meteorology data) at 10 m intervals, and the metric curve is the best fit (of equation (4.21)) to the average absorption computed from the model output. This metric curve was used in the same way, with corrections for instrument path length and the ratio of concentrations. The resulting range estimate was 37.27±2.1 m, or 5% error.

The residual error in this experiment may indicate a systematic error inherent in using FASCODE to predict range. Range estimation was repeated using several metric curves based on a variety of settings in FASCODE to see which assumptions best replicated the data. While the changes to the model inputs produced significant differences in spectra and $\bar{A}$, the net change in the range estimate (after the N'/N correction) is minimal. Although this idea did not help in reducing the systematic error, the result is actually somewhat encouraging–it indicates the range estimation method is not sensitive to differences in atmospheric conditions.

For comparison, range estimation was also attempted using the two-color ratio metric discussed in Chapter II. The ratio used was the measured value at the peak of the PP(J=9) line over the baseline value at the same frequency. A metric curve was again computed using the same ratio metric applied to the previous data. The curve

Table 5.1:   *Summary of range accuracy from hallway data. Actual*
range was 39.25m (or 36.6m for the first two rows, where ranges are
measured from the entrance pupil).

Metric curve data source	Metric curve fit eqn	Corrections applied	Range Estimate	Range Error		Range Uncertainty
Historical Data (16Sep)	eqn(4.21)	none	37.09m	49cm	1.3%	2.1m
		L_{inst}	40.03	78	2.0	
		N'/N	36.22	38	1.0	
		both	39.10	15	0.4	
	eqn(4.19)	both	39.58	33	0.8	
	Beer's Law	both	39.62	37	0.9	
FASCODE	eqn(4.21)	both	37.25	200	5	1.20
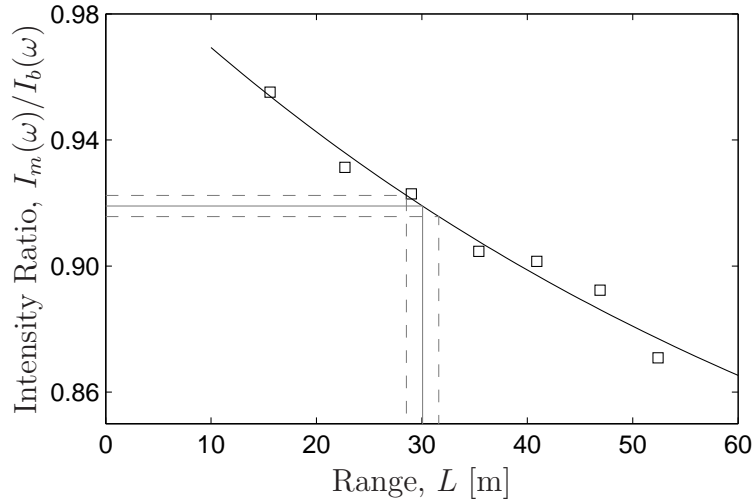
Figure 5.2:   Results of range estimation using an intensity
ratio metric.

used in this example is a simple exponential decay, $y = 1 - c_1(1 - e^{-c_2 x})$. The range
estimate from this metric was 30.1 ± 1.5m. This is shown in Figure 5.2.

One factor that contributes to the systematic error in this estimation is illus-
trated in Figure 5.2, which shows sample spectra from the Hallway-II and III experi-
ments. The spectral lines are shifted slightly from one day to the next. This could be
caused by changes in instrument calibration or even shifts in the index of refraction of
the air. The result is that the sample point used in the ratio falls on a different part of
the lineshape on each day. The total area within the line should be the same (assum-
ing the air temperature is nearly the same) regardless of lineshapes or sampling, so

72
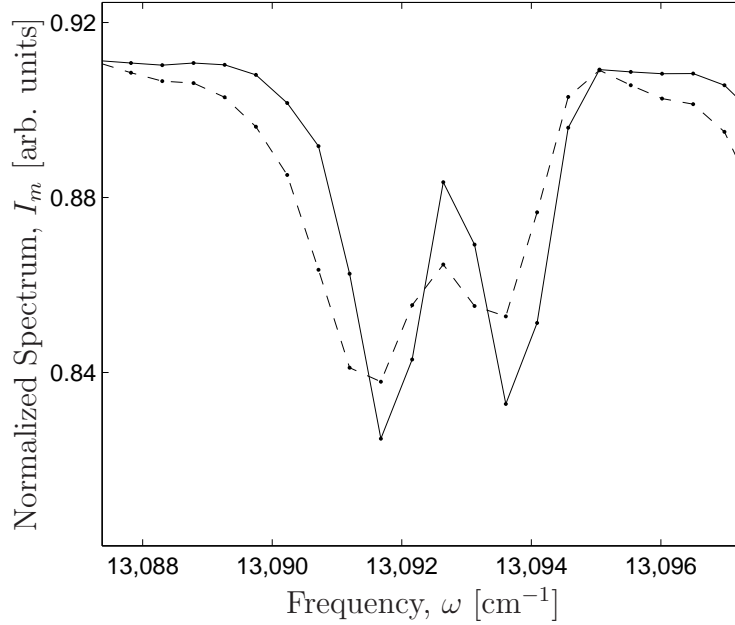
Figure 5.3:   Spectra from Hallway-II (—) and Hallway-III (- - -) to show the difference in sampling. The region shown here is about the $J=9$ doublet.

one could remove this systematic error by averaging the intensity over the entire $J=9$ doublet (13,087-13,095 cm^{-1}). The ratio of this intensity against baseline (averaged in the same region) is, of course, the band-averaged transmission, averaged over a much smaller band than the usual definition of $\bar{A}$. If this narrow-band average is used as before, the range estimate is 36.02±1.37 m, or 1.5% error (without corrections for instrument path length or concentration).

5.1.2   Noise Behavior.   Multiple measurements were taken of the same source to help characterize the noise behavior of the system. Data was acquired at two different resolutions, as well as two different integration times (number of scans per file).

As expected, changing the number of scans in the average had a significant effect on the noise, characterized by the standard deviation in calculations of $\bar{A}$, denoted s_A. The results of this noise comparison are shown in Table 5.2. The values of $\bar{A}$ agreed to within 1.5% for all three data sets.

73

Table 5.2: *A brief summary of how noise depends on instrument settings.*

Set Description	No. of Samples	StdDev, s_A
1 cm^{-1}, 50 scans/file	25	5.8E-4
1 cm^{-1}, 250 scans/file	45	3.8E-4
4 cm^{-1}, 250 scans/file	25	3.7E-4

To examine the behavior of noise vs integration time (or number of scans), multiple measurements are digitally added in post-processing to simulate longer and longer integration times. Each point in Figure 5.4 is the result of range estimation using one such averaged spectrum. The metric curve used for this was equation (4.21) fit to 16 Sep data as before. Each point on this plot is a range computed from a random combination of the raw data files from 22 Sep. The number of files used to make each point is a random variable (uniformly distributed), and the particular files used in each case are also random picks. This process was repeated 3,000 times to make this figure. The horizontal lines in this figure show the mean value of estimated range and the actual value. The difference between the two lines indicates 15 cm of systematic error, as was reported in Table 5.1.

The SNR values in this figure were computed as the ratio of the baseline value (signal) to the RMS variation about that line (noise). Only the spectral regions used in defining the baseline were included in this computation. This definition of signal, as opposed to using the *in-band* level, is useful in characterizing the noise behavior of the system. Photon noise, for example, occurs in the interferogram, so is determined by the total irradiance rather than the spectral irradiance in any one band. Alternatively, one could use the in-band signal level, which may be more appropriate for some types of performance predictions.

It will also useful to understand how the accuracy of $\bar{A}$ depends on the measurement noise. To calculate s_A as a function of SNR, one would ideally compute the standard deviation over a set of several independent realizations for each value of SNR. This is complicated by the fact that SNR is not an independent or continuous

74
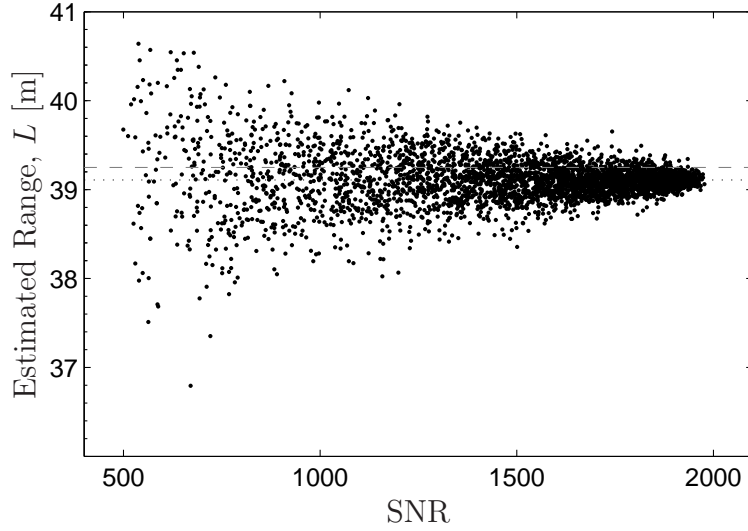
Figure 5.4:   Estimated range in Hallway III experiment as a function of SNR. SNR is controlled by digitally adding multiple files in post processing and repeating the range extraction as above using the averaged data.

variable, so it is approximated using the data in fig 5.4. These points are divided up into bins according to SNR value, using a bin width of 50. Then s_A is the standard deviation over the set of all points within the bin. To avoid a bias caused by repeating multiple realizations of the same case, points generated from a single file were excluded, as were points from 44 or 45 files (e.g. there is only one possible way to combine all 45 files, so in 3,000 random draws there is a good chance of counting this more than once). Also, sparsely populated SNR bins (containing fewer than 1% of the total number of samples) were considered to be invalid.

Figure 5.5 shows the resulting values of fractional uncertainty $(s_A/\bar{A})$ for each SNR bin, as well as a best fit line. The fit equation $y = (c_1/\sqrt{x})\exp(-x/c_2)$ was chosen empirically as the best fit that had appropriate asymptotic behavior (*i.e.*, $s_A \to \infty$ as SNR$\to$0 and $s_A \to$0 as SNR$\to \infty$). In this plot, c_1=73.3 and c_2=1,052. The form of this equation shows that at low values of SNR, the measurement error scales like $1/\sqrt{SNR}$, as is typical for Gaussian or Poisson distributed noise processes. As SNR increases, the exponential decay term becomes important, and the measurement error decays faster than $1/\sqrt{SNR}$.

75
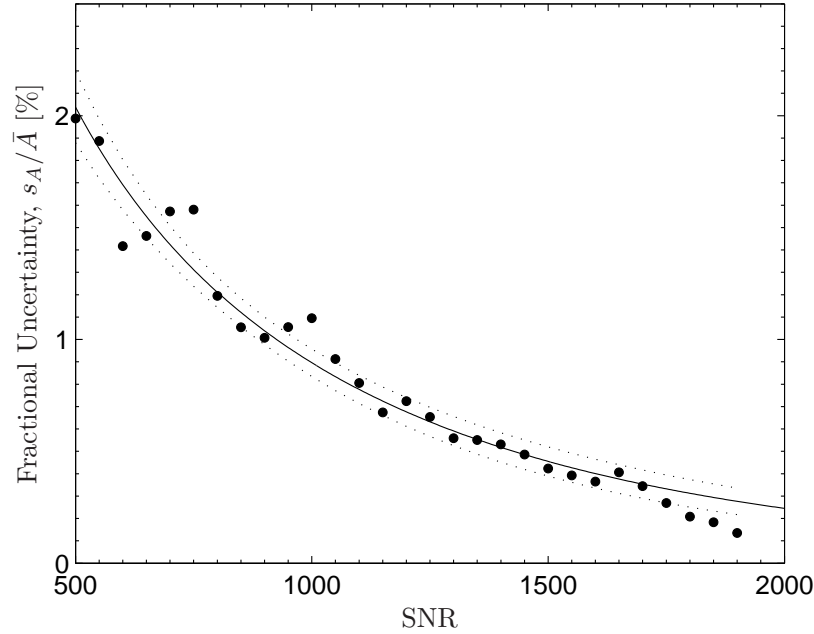
Figure 5.5: Fractional uncertainty in $\bar{A}$ as a function of SNR (from Hallway-III data). Dotted lines show the 99% confidence interval for the fit line.

5.2 Background Subtraction

As previously mentioned, scattered solar background can potentially corrupt the data because it is not slowly varying. The background with the most noticeable effect on the data was plain blue sky at Edwards AFB. The spectrometer was situated looking uphill at the QTH lamp with blue sky behind the lamp. Figure 3.7 shows a sample of the data with this sort of background.

As a first attempt, a simple background subtraction was used to adjust the Edwards hillside data. Spectra were acquired with the lamp on and lamp off, with no other changes to the scene. There were also thin cirrus clouds moving through the background during this process, so the background scene was not static. The difference between the two spectra is taken to be the lamp spectrum, and $\bar{A}$ is computed from that difference spectrum. The results of this simple method are shown in Figure 5.6 along with FASCODE predicted values for reference.

Although scattered sunlight may be an issue at longer ranges, the background observed in the majority of the experimental data was too faint to be of any real use in
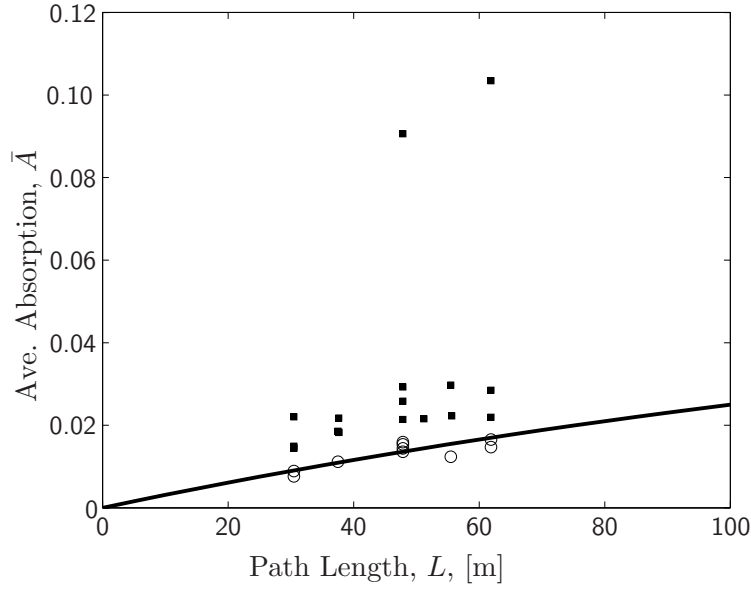
Figure 5.6: $\bar{A}$ as a function of range curve for raw spectra (■) and with background subtracted (○). The results of background subtraction are well correlated with FASCODE predictions (—).

analysis. The combination of relatively dark background scenes and poor instrument sensitivity produced background spectra with very low SNR, so that background subtraction added noise without noticeable improvement in estimates of $\bar{A}$. The above discussion of background subtraction is meant as an indication of what might be possible for future applications rather than as development of a method central to the analysis presented in the rest of this paper. A more detailed investigation of this area is recommended.

5.3 Range Results from SRM Test

5.3.1 Range Estimation. Because this was a single event, there is no historical data to derive a metric curve. The next best source is to fit a curve to FASCODE data. FASCODE is again run at multiple ranges assuming a standard atmosphere, and $\bar{A}$ computed from each spectrum. Because the potassium emission doublet at the red end of the O_2 band will corrupt estimates of absorption in that region, averages are taken over the R-branch only (13,121-13,170 cm^{-1}), or $\bar{A}_R$. Equation (4.21) is

77
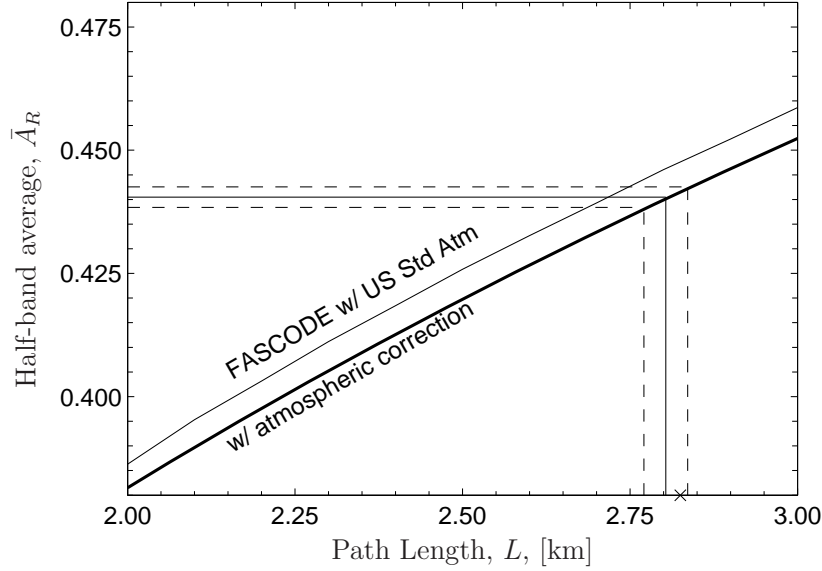
Figure 5.7:   Range estimation from SRM experiment. The ranges for
the metric curve are multiplied by the ratio of concentrations to create
the "w/ atmospheric correction" curve.

Table 5.3:   *SRM range estimation results.*

Method	Range	Error
GPS (actual range)	2.825 km	-
Cubic spline interpolation of FASCODE data	2.719 km	106 m
Spline + N'/N correction	2.805 km	20 m
Eqn 4.21 fit to FASCODE data	2.724 km	101 m
Fit + N'/N correction	2.811 km	14 m

then fit to these model points to compose a metric curve. This range is then scaled by

the ratio of concentrations, as discussed above in section 3.2.3. Background subtrac-

tion was not necessary, as the rocket motor was hundreds of times brighter than the

background and nearly filled the FOV. The results of this range estimation are shown

in Table 5.3. Note that the range error is once again comparable to the uncertainty

in the "known" range.

Although the Hallway range estimation results appeared to indicate a 5% sys-

tematic error when using FASCODE, that is not evident here. One possible explana-

78

tion is that some error source is additive rather than multiplicative (*i.e.*, about 2 m of error, not 5%), or that the error lies in the P-branch, which is not used here.

Range extraction was also attempted using the $v'' = 0 \rightarrow v' = 1$ band around 14,500 cm^{-1}. The band limits were taken to be 14,410-14,560 cm^{-1}. This does not include all the rotational lines of the band. The red end of the band overlaps a weak H$_2$O band, so some of the high J lines were truncated to avoid this. The regions from 14,000-14,200 and 14,600-14,900 cm^{-1} were used for the out-of-band data to estimate baseline. A second order polynomial is a good estimate of baseline in this region, as well. Range estimated using this metric was 2.89±0.07 km (without corrections). This band appears to be suitable, although further study of the H$_2$O band is needed before extending this to long range.

5.3.2 Noise Behavior. The standard deviation in $\bar{A}_R$ over the eight samples was 0.0021, which gives a range uncertainty of 33 m. Based on Figures 5.5 and 3.10, a value of $s_A/\bar{A}_R \simeq 2.5\%$ is expected. In this data set, however, the fractional uncertainty in $\bar{A}_R$ is only 0.5%. The difference may be because the data in this experiment is at lower spectral resolution than the data from which the s_A vs SNR relationship was derived, or the standard deviation in $\bar{A}_R$ may not follow the same relationship as the whole-band metric. With only eight samples, however, it is difficult to even be sure that the two cases really are different in any significant way.

Note that in calculating the SNR for this data, it was necessary to exclude the data from 12,814-12,819 cm^{-1} to avoid a small emission line (believed to be the rubidium $^2S_{1/2} \rightarrow {}^2P_{3/2}$ line), shown in Figure 5.8. Recall that SNR is computed from the error between the out-of-band data and the computed baseline. In this data set, the emission line contributed nearly 2/3 of the total "error". With that small region left out, the noise is a better measure of the *random* variations.

In section 2.4.1, the band limits used in computing the baseline were given as a somewhat arbitrary choice. Factors such as this emission line and other absorption

79
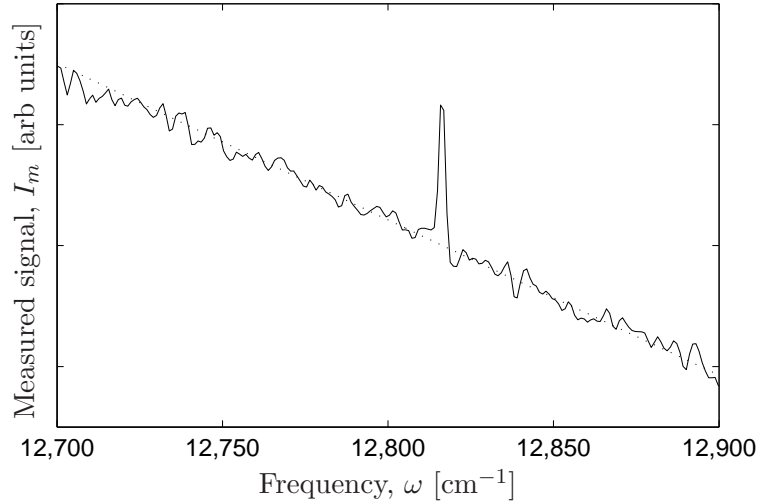
Figure 5.8:   Raw spectrum (—) and estimated baseline value (---)
from SRM test.

bands are the main limit to this. From Figure 3.9, it is apparent that CO_2 and H_2O
bands constrain the choice of band limits.

5.4   Summary

The results presented in this chapter demonstrate the validity of the new range
estimation technique proposed in Chapter II. Experimental results show the new
modified random band model proposed in Chapter IV can be used to estimate range
within 1% accuracy. In hallway experiments, use of this model reduced range error
by almost than 60% compared to the Beer's Law methods of previous work. Chapter
VI will now discuss how these short-range results can be extrapolated to predict
performance at operationally significant ranges.

VI. Sensitivity and Error Analysis

W hile the experimental demonstrations with errors below 1% are very encouraging, the real question is how the technique might work at long ranges. To answer that question, it is necessary to examine what limits the range accuracy. Sections 6.1 and 6.2 begin by examining analytic derivatives of the band model equation, equation (4.21), to understand how range error depends on a few sources of experimental error. This analysis is then applied to some example scenarios in sections 6.3 and 6.4. Lastly, section 6.5 examines the effect of the potassium emission line.

6.1 Range Error due to Measurement Error

To begin, suppose the same error in $\bar{A}$ can be achieved at longer range. A quick look at the shape of the metric curves shows that range error will still increase because the slope of the curve changes. For regions where the plot of $\bar{A}$ vs L are nearly flat, a very small error in $\bar{A}$ will translate into a very large error in range.

In other words,

$$\Delta L = \left| \frac{dL}{d\bar{A}} \right| \Delta \bar{A} = \left| \frac{dA}{dL} \right|^{-1} \Delta \bar{A}, \tag{6.1}$$

so begin by taking derivatives of $\bar{A}$. Recall that the band model is

$$\bar{A} = 1 - \exp\left\{ C\,\mathrm{erf}\left[y\mathcal{L}(\eta\Lambda) \right] \right\},$$

$$\Lambda = \int\limits_{0}^{L} \exp\left[-\frac{1}{H}\left(z_o + \ell\cos\theta + \ell^2 \frac{\sin^2\theta}{2R_e} \right) \right] d\ell. \tag{4.21}$$

where $y = \pi^{3/2}\alpha/\delta$ and $\eta = SN_o/2\pi\alpha$. The new parameter, η, is equivalent to the fit coefficient, c_1, but the new notation is introduced to differentiate this number from the optimized value. Note that the product $\eta\Lambda$ is equal to u, which is also equivalent to $\tau/2$ at line center.

Before attempting to differentiate this equation, it will be helpful to look at derivatives of some of the component functions. By Leibnitz Rule, the derivative of

the error function is

$$\frac{d}{d\xi}\mathrm{erf}(\xi) = \frac{d}{d\xi}\left(\frac{2}{\sqrt{\pi}}\int_0^{\xi}\exp(-x^2)dx\right) = \frac{2}{\sqrt{\pi}}\exp(-\xi^2). \qquad (6.2)$$

Leibnitz Rule also gives

$$\frac{d\Lambda}{dL} = \exp\left[-\frac{1}{H}\left(z_o + L\cos\theta + L^2\frac{\sin^2\theta}{2R_e}\right)\right] = \exp\left(-z(L)/H\right). \qquad (6.3)$$

Derivatives of the Ladenburg-Reiche function are a bit more complicated:

$$\begin{aligned}
\frac{d}{d\xi}\mathcal{L}(\xi) &= \frac{d}{d\xi}\left[\xi e^{-\xi}(\mathrm{I}_0(\xi) + \mathrm{I}_1(\xi))\right] \qquad\qquad (6.4)\\
&= e^{-\xi}\left\{(1-\xi)\left[\mathrm{I}_0(\xi) + \mathrm{I}_1(\xi)\right] + \xi\frac{d}{d\xi}\left[\mathrm{I}_0(\xi) + \mathrm{I}_1(\xi)\right]\right\}\\
&= e^{-\xi}\left\{(1-\xi)\left[\mathrm{I}_0(\xi) + \mathrm{I}_1(\xi)\right] + \xi\left[\tfrac{1}{2}\mathrm{I}_0(\xi) + \mathrm{I}_1(\xi) + \tfrac{1}{2}\mathrm{I}_2(\xi)\right]\right\}\\
&= e^{-\xi}\left[\left(1-\frac{\xi}{2}\right)\mathrm{I}_0(\xi) + \mathrm{I}_1(\xi) + \frac{\xi}{2}\mathrm{I}_2(\xi)\right] \equiv e^{-\xi}\mathcal{B}(\xi).
\end{aligned}$$

For convenience, the function $\mathcal{B}(u)$ has been defined as the quantity within the square brackets above.

With that, the derivative can now be written as

$$\begin{aligned}
\frac{d\bar{A}}{d\Lambda} &= \exp\left\{-C\mathrm{erf}[y\mathcal{L}(\eta\Lambda)]\right\}\frac{d}{d\Lambda}\left(C\mathrm{erf}[y\mathcal{L}(\eta\Lambda)]\right) \qquad (6.5)\\
&= C(1+\bar{A})\exp\left[-\left(y\mathcal{L}(\eta\Lambda)\right)^2\right]\frac{d}{d\Lambda}\left(y\mathcal{L}(\eta\Lambda)\right)\\
&= C\eta y(1+\bar{A})\exp\left[-\eta\Lambda - y^2\mathcal{L}^2(\eta\Lambda)\right]\mathcal{B}(\eta\Lambda).
\end{aligned}$$

By the chain rule, equations (6.3) and (6.5) can be combined to find the slope of the metric curve,

$$\frac{d\bar{A}}{dL} = \frac{d\bar{A}}{d\Lambda}\frac{d\Lambda}{dL} = C\eta y(1+\bar{A})\mathcal{B}(\eta\Lambda)\exp\left[-\eta\Lambda - y^2\mathcal{L}^2(\eta\Lambda) - \frac{z(L)}{H}\right]. \qquad (6.6)$$

82

To keep range uncertainty small, $d\bar{A}/dL$ should be large. A few things can be concluded directly from examining the form of this equation. First, the $\exp(-z(L)/H)$ term indicates range accuracy is better against targets low in the atmosphere, as expected. Also, notice that the quantity $\eta\Lambda$ is proportional to concentration length, so is always increasing with path length. For large arguments, $\mathcal{B}$ increases exponentially, but this increase is offset by the exponential decay term, $\exp[-\eta\Lambda - y^2\mathcal{L}^2(\eta\Lambda)]$ with the result that the product is monotonically decreasing. As a result, range accuracy will be best for lower values of $\eta\Lambda$. Typical values of $\eta\Lambda$ for cases of operational interest range from about 10 to 100, and are indirectly proportional to θ.

Figure 6.1 shows computed values of the inverse slope, $dL/d\bar{A}$ for a few representative cases. This plot shows that even if high-SNR measurements can be obtained at long range, the range error will still be orders of magnitude higher, simply due to the slope.

For example, suppose measurement accuracy of 1% (*i.e.*, $s_A/\bar{A} = 0.01$) is achieved, similar to the short range results. From Figure 5.5, this is equivalent to a SNR of about 900. Figure 6.2 shows the resulting range error for the same cases used for Figure 6.1, assuming 1% measurement error in $\bar{A}$.

Examination of Figure 6.1 confirms the intuitive statement that range estimates will be poor where the metric curve is nearly flat. This, in turn, means that absorption-based techniques like MPR work best when the target is in denser portions of the atmosphere so that concentration length is a strong function of distance [13,31] and the slope $d\bar{A}/dL$ is large. Figure 6.3 shows range error plotted as a function of the concentration at the target (normalized by the concentration at the sensor) as another way to look at this issue. When plotted on these axes, it is clear (at least for up-looking cases) that the concentration at the target is the most important factor in determining range error caused by measurement error in $\bar{A}$.

83
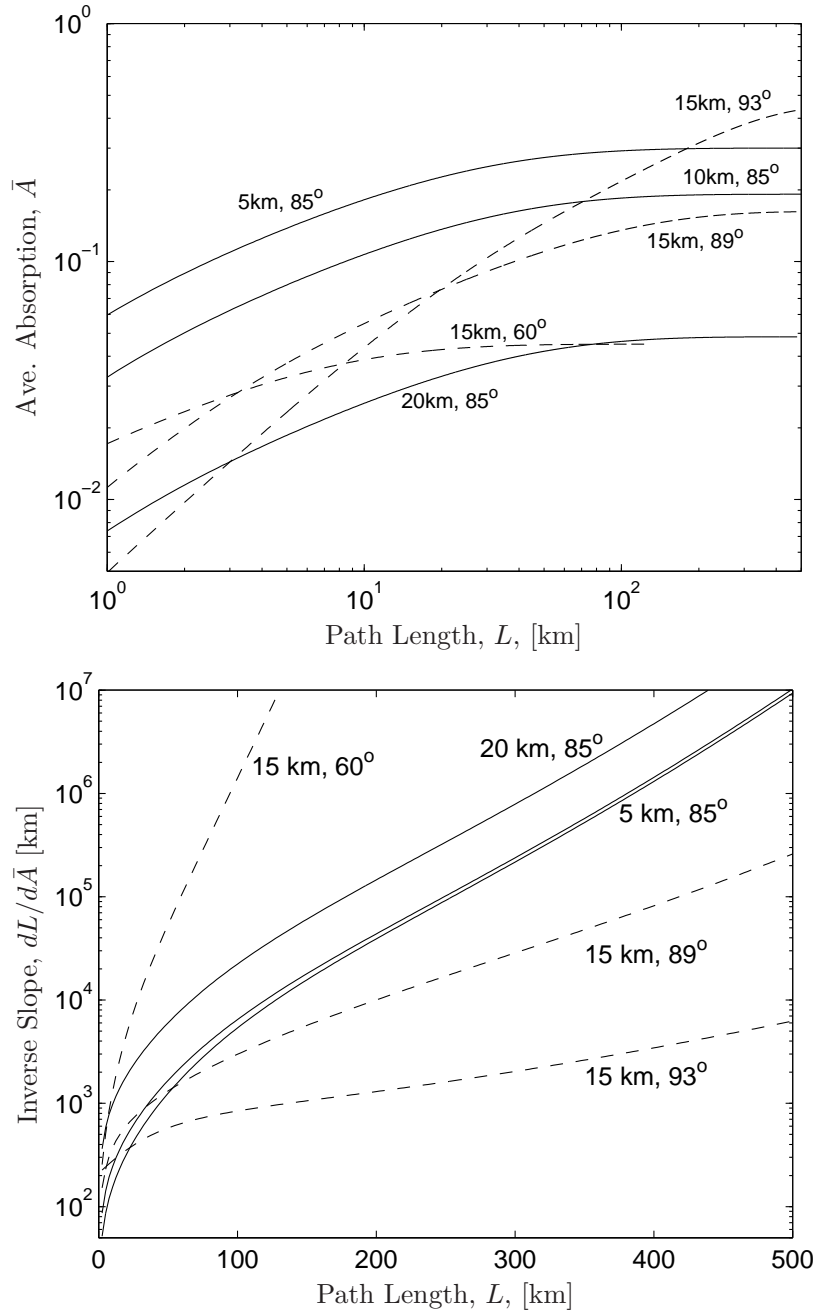
Figure 6.1: *Top* : plots of $\bar{A}$ as a function of L for a few representative cases. $\bar{A}$ is computed from equation (4.21) using the coefficients from Figure 4.12. *Bottom* : The inverse slope, $dL/d\bar{A}$, for the same cases. Labels represent the sensor altitude and zenith angle for each case. Solid lines (–) compare cases with different altitudes for the same zenith angle, dashed lines (- -) compare constant altitude for different zenith angles.

84
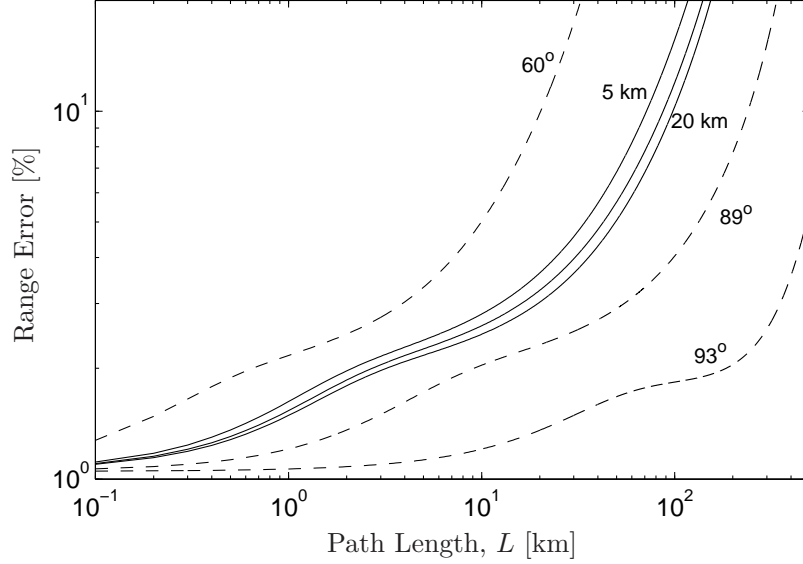
Figure 6.2:   Range error (in %) caused by measurement error, assuming $s_A/\bar{A} = 1\%$. As in Figure 6.1, solid lines (–) compare cases with the same zenith angle (85°) but different altitudes, dashed lines (--) compare different zenith angles for altitude=15 km.

6.2   Other Sources of Range Error

The previous discussion assumed that the dominant source of error would be errors in estimating $\bar{A}$. Other factors of course will contribute to the total error.

6.2.1   Pointing Error.   There will be some uncertainty in knowledge of the zenith angle, θ, due to either jitter, body flexure, or actual errors in the aircraft attitude sensor. The zenith angle is used to compute the metric curve, so pointing error essentially leads to computing the wrong curve. The resulting range error will be

$$\Delta L = \left|\frac{dL}{d\theta}\right| \Delta\theta = \left|\frac{dL}{d\Lambda}\right| \left|\frac{d\Lambda}{d\theta}\right| \Delta\theta = \frac{|d\Lambda/d\theta|}{|d\Lambda/dL|} \Delta\theta. \tag{6.7}$$

Equation (6.3) already showed that $d\Lambda/dL$ depends only on the altitude of the target. The derivative with respect to θ will be simpler with the alternate form of Λ from equation (4.13),

85
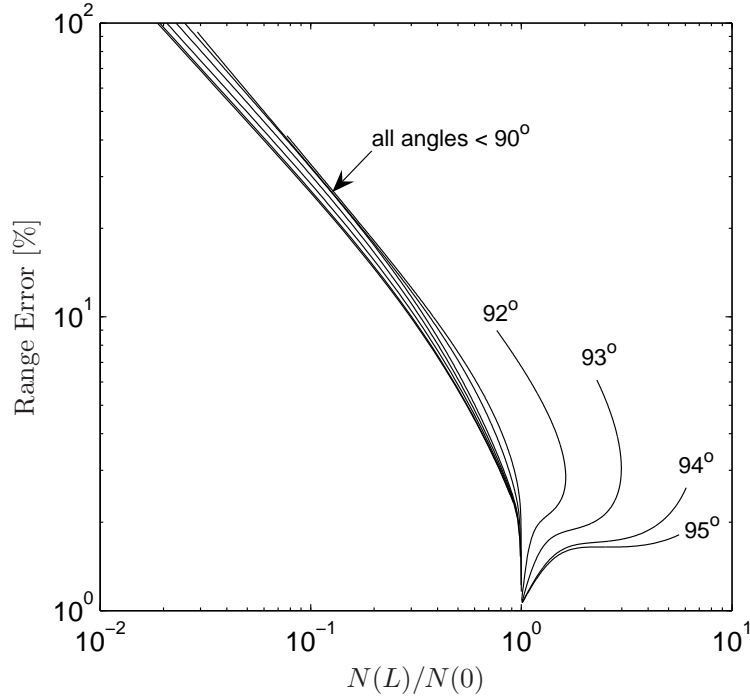
Figure 6.3: Range Error (in %) assuming $s_A/\bar{A} = 1\%$. All up-looking cases are very tightly grouped on this plot regardless of sensor altitude or zenith angle. Down-looking cases are more complex; curves shown are for altitude of 15 km.

$$\Lambda = e^{-z_o/H} \sum_{k=0}^{\infty} \left[\frac{(-1)^k}{k!} \frac{a^{2k}}{b^{2k+1}} \gamma(2k+1, bL) \right].$$

[4.13]

The constants a and b both depend upon θ.

As before, it will help to look at derivatives of some parts of this equation before the whole. The incomplete gamma function, γ, is once again handled with the Leibnitz Rule:

$$\frac{d}{dx} \left(\gamma(k, x) \right) \;=\; \frac{d}{dx} \left[\int_0^x e^{-\xi} \xi^{k-1} d\xi \right] = e^{-x} x^{k-1},$$

(6.8)

so

$$\frac{d}{d\theta} \gamma(2k+1, bL) = \frac{d\gamma}{dx} \frac{dx}{d\theta} = e^{-bL}(bL)^{2k} \left(-\frac{L \sin\theta}{H} \right).$$

(6.9)

86

The derivative of the ratio of constants is

$$\frac{d}{d\theta}\left[\frac{a^{2k}}{b^{2k+1}}\right] = 2ka^{2k-1}b^{-(2k+1)}\frac{da}{d\theta} - (2k+1)a^{2k}b^{-2k-2}\frac{db}{d\theta} \qquad (6.10)$$

$$= \frac{a^{2k}}{b^{2k+1}}\left[\frac{2k}{a}\frac{\cos\theta}{\sqrt{2HR_e}} + \frac{(2k+1)}{b}\frac{\sin\theta}{H}\right]$$

$$= \frac{a^{2k}}{b^{2k+1}}\left[2k\cot\theta + (2k+1)\tan\theta\right].$$

The derivative of Λ with respect to θ is, therefore,

$$\frac{d\Lambda}{d\theta} = e^{-z_o/H}\sum_k\frac{(-1)^k}{k!}\left[\frac{a^{2k}}{b^{2k+1}}\frac{d\gamma}{d\theta} + \gamma(2k+1,bL)\frac{d}{d\theta}\left(\frac{a^{2k}}{b^{2k+1}}\right)\right]$$

$$= e^{-z_o/H}\sum_k\frac{(-1)^k}{k!}\frac{a^{2k}}{b^{2k+1}}\left\{\gamma(2k+1,bL)\left[2k\cot\theta + (2k+1)\tan\theta\right] \qquad (6.11)\right.$$

$$\left. -bL\cot\theta e^{-bL}(bL)^{2k}\right\}.$$

Multiplying this by $d\Lambda/dL$ from equation (6.3) gives total range error as a function of pointing errors. Figure 6.4 shows plots of the range error caused by pointing error. This error is quite small (on the order of a few meters or less) for most cases of interest to this problem.

6.2.2 *Concentration.* If the metric curve is derived from historical data, there will be differences in the atmosphere when the new data is acquired. Optimizing c_1 effectively determines the value of N that best describes the data. But for the new day and new conditions, a different curve (with a different value of c_1) would be a better match to new observations. Errors in concentration are, therefore, assumed to affect the range through the value of c_1, or η.

This might seem spurious at first glance. Changes in concentration will, of course, affect the concentration length, m, which has been approximated by the product $m = N_o\Lambda$. The equivalent path, Λ, was computed assuming an exponential atmosphere. It is not meant to reflect actual variations along the path, but is simply a reference length based on a useful approximations. All concentration errors

87
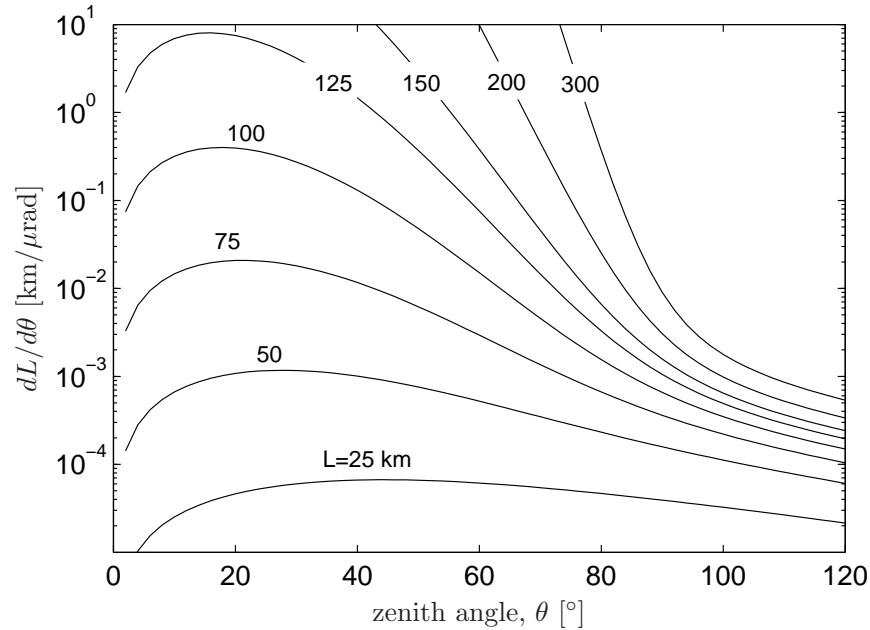
Figure 6.4: Range errors caused by pointing errors, in km/μrad. The numbers annotate the path length, L, of each curve.

on the path must, therefore, be corrected by choosing appropriate values of N_o, the sea-level concentration. Theoretically, this is the sea-level value of concentration. In practice however, fitting c_1 finds an effective value that accounts for deviations from the exponential atmosphere model. The concept of using a single value of concentration to represent an inhomogeneous path is not new. The standard texts on the subject [17, 22, 33] suggest using either the midpoint of the path or the mean of the values at the two endpoints, but these values will not generally be known for the applications discussed here.

It should also be noted that this issue can be avoided entirely for applications that allow time for post-processing of the data. FASCODE can predict the absorption (and the metric curve) given accurate information about the structure of the atmosphere at that time. The most accurate atmospheric profiles can be obtained from the Air Force Combat Climatology Center (AFCCC), but not in real-time. The AFCCC computes detailed and accurate profiles for arbitrary paths. For maximum accuracy, the models make use of all available meteorology observations worldwide,

88

but this data can be delayed by as much as 24 hours from some remote stations . For tactical and other near-real time applications, the differences between the actual and model atmospheres cannot be avoided and will lead to errors in range.

As usual, estimating this error begins with derivatives:

$$\Delta L = \left| \frac{dL}{dN} \right| \Delta N = \left| \frac{dL}{d\bar{A}} \right| \left| \frac{d\bar{A}}{d\eta} \right| \left| \frac{d\eta}{d\bar{N}} \right| \Delta N. \tag{6.12}$$

Recall $d\bar{A}/dL$ was already found to be

$$\frac{d\bar{A}}{dL} = \frac{d\bar{A}}{d\Lambda} \frac{d\Lambda}{dL}. \tag{6.13}$$

Notice also that

$$\frac{d\bar{A}}{d\eta} = \frac{d\bar{A}}{d\Lambda} \frac{\Lambda}{\eta}, \tag{6.14}$$

which gives

$$\frac{dL}{d\bar{A}} \frac{d\bar{A}}{d\eta} = \frac{\Lambda}{\eta} \frac{dL}{d\Lambda}. \tag{6.15}$$

With this, equation (6.12) can be simplified as

$$
\begin{aligned}
\Delta L &= \frac{\Lambda}{\eta} \left| \frac{dL}{d\Lambda} \right| \left| \frac{d\eta}{d\bar{N}} \right| \Delta N \\
&= \frac{S\Lambda}{2\pi\alpha\eta} \exp\left(-\frac{z(L)}{H} \right) \Delta N \\
&= \Lambda \exp\left(-\frac{z(L)}{H} \right) \frac{\Delta N}{N} = \Lambda \exp\left(-\frac{z(L)}{H} \right) \frac{\Delta\eta}{\eta}.
\end{aligned}
\tag{6.16}
$$

This is plotted in Figure 6.5. This error is very small except for very long ranges and zenith angles greater than 90°.

6.2.3 Fit Errors.   Some error will also be introduced by the fact that the band model (equation (4.21)) does not perfectly match the data. For this error, analytic derivatives cannot be computed to establish error estimates: the band model is already the best effort at an analytic equation to describe the curve. The value for this error will not only vary on a case-by-case basis, but it will also depend on the

89
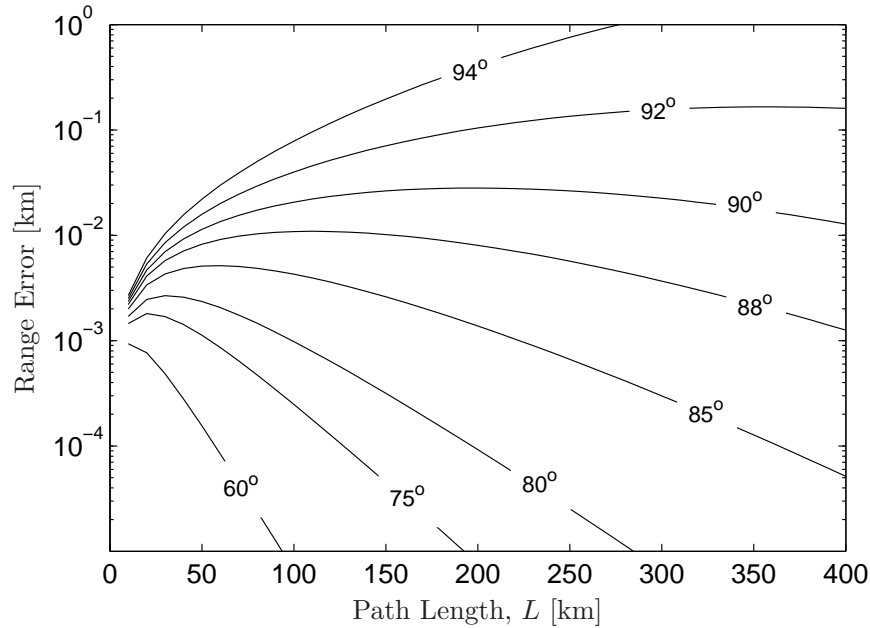
Figure 6.5: Range errors caused by 1% differences in concentration. Numbers indicate the zenith angle. Values in this plot can be multiplied by the fractional error (in %) in either c_1 or N to find range error in km.

number of FASCODE runs used, the ranges chosen for FASCODE, etc. This error is best estimated on a case-by-case basis using the MSE values reported in Chapter IV (e.g., Fig 4.9).

In practice, this error can be made quite small by only fitting to ranges of actual interest to the problem at hand. The fitting errors reported in Chapter IV are largely a result of the difficulty of describing both short and long range behavior simultaneously. The fit quality is lowest for angles around 91-95°. In these regions, (or more generally any time the root-mean-square (RMS) error between the FASCODE data and the best fit line exceeds about 10^{-3}), it is better to simply interpolate the FASCODE points and skip fitting.

6.2.3.1 Fit Error Example. To illustrate how the fit curve can affect range accuracy, range was estimated using three different curves fit to the same FASCODE simulated data. The curves were based on Beer's Law, the random band model (equation (4.19)), and the modified random band model (equation (4.21)).

90

The same $\bar{A}$ values used to define these curves were then treated as the "observed" values, and the curves were used to find three range estimates.

An example of this process, for $z_o = 10$ km and $\theta = 90°$, is shown in Figure 6.6. In this example, use of the band models reduced the rms range error by more than an order of magnitude compared to Beer's Law, and adding information about the structure of the atmosphere (by using eqn (4.21)) reduces rms range error by another 26% compared to the random band model.

This process was repeated for all ranges and cases used in Figure 4.9. Points where the observed value of $\bar{A}$ was greater than the maximum value of any curve were rejected. Since there is no intersection of the observed value with the curve in these cases, alternate methods to estimate range would be needed. The rms average range error over all cases was three times greater when using Beer's Law compared to the random band model (eqn (4.21)). When averaged in this way, the two band models perform almost equally, which is somewhat deceptive–the long range cases that are rejected tend to favor eqn (4.21).

6.3 Example 1: Airborne Laser

Because of the complexity of error equations above, it may be more enlightening to look at specific cases of interest. For the first example, take the Airborne Laser (ABL) System. This airframe is considered a high-value asset that would normally only operate in controlled airspace. This means that the ABL is expected to be 100s of km from the missiles it needs to be able to defeat. The mission and the size of the airframe allow for a fairly advanced sensor system with large collecting apertures, high-precision pointing, and high spectral resolution.

The ABL is currently designed with an Active Ranging System (ARS). As a concept for study, lets suppose a passive ranging sensor used in place of the ARS. The ARS does not use the large beam-director telescope, but has a smaller aperture that is meant to be rapidly slewed to interrogate multiple tracks before nominating a target for the main beam.

91
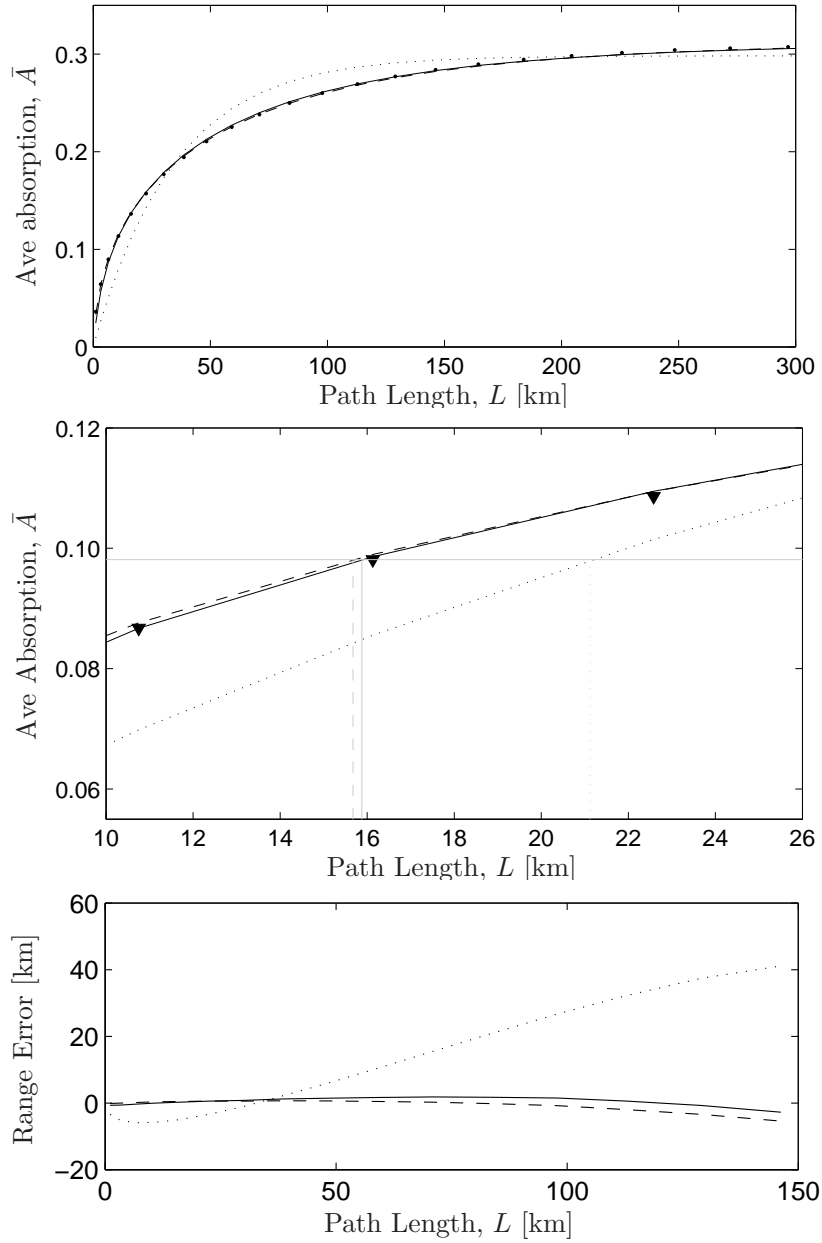
Figure 6.6: Example of range estimation using three different fit functions. Top: The three metric curves. The dots (·) show FASCODE model points. Middle: Closeup view to show range extraction for one value of $\bar{A}$. Black lines indicate metric curves and gray lines to indicate the range estimates from each curve. Bottom: Range error for each FASCODE model point. In each plot, dotted lines (···) show fit curve for Beer's Law; dashed lines (- - -) for eqn (4.19); and solid lines (—) for the modified band model (4.21).

Suppose the ABL is operating at an altitude of 12.5km, and a TBM is launched from a site 300 km away (ground range and slant range are almost equal for this shallow angle). Assuming the launch azimuth is perpendicular to the line of sight, the range will be nearly constant throughout the engagement. The other assumptions are listed in Table 6.1.

Table 6.1:   *Assumptions in ABL Scenario.*

Sensor:		Missile:	
altitude	12.5km	Spectral Intensity	75 W/str cm^{-1}
FOV (full angle)	500 μrad	Altitude at burnout	50 km
Aperture diam.	8 inch	**Scenario:**	
Optical sys. throughput	30%	Range	300 km
Detector quantum eff.	80%	Sky radiance	
Photon-noise limited	-	*max*	2.6E-7 W/cm^{2}str cm^{-1}
Spectral Resolution	8 cm^{-1}	*min*	2.2E-8 W/cm^{2}str cm^{-1}
Temporal Resolution	0.1 sec		

For this scenario, the trajectory of the missile as viewed from the sensor will go through zenith angles from about 94° at launch to about 84° at burnout. The launch point is near the limb of the Earth, so the sensor will see a sky background shortly after launch. The sky radiance varies by more than an order of magnitude over this range of angles, and is brightest as the rocket comes above the Earth limb. The values shown in the table are the average level around 13,200 cm^{-1} as computed by MODTRAN (via the PLEXUS user interface). The actual values will depend on time of day, season, azimuth angle and sensor latitude, but for this project, these estimates (for a sensor in Dayton, OH looking at an azimuth of 30°, at 10:00am local time) will be sufficient to get an appreciation for the problem.

Given these assumptions, the target is about twice as bright as the background at launch (in terms of the received irradiance, which will depend on range, FOV, etc.). To compute SNR, the background photons are included in the total signal level used to compute the variance (noise counts), but not in the signal. It is assume that background subtraction techniques will be applied and that the background is static. Since measurements of the background are also noisy, the photon noise of the

93

background measurement is also added into the total noise. With this, the SNR varies from about 2,100 shortly after launch to over 3,500 at burnout. If the scaling rule of Figure 5.5 is assumed to apply here, expected values of fractional measurement error $(d\bar{A}/\bar{A})$ range from 0.21% at launch to 0.04% at burnout.

Figure 6.7 shows the resulting range error caused by this measurement error for two cases: one with the above background and one without, representing a night launch. Also shown are the range errors resulting from a pointing error of 50 μradians and a 5% error in concentration. The total error here is computed by assuming the fitting error is negligible and the other error sources are independent.

With the background (day), measurement error is the dominant source of range error, although the concentration error does contribute slightly at low target altitudes. At night, with no background, all error sources contribute in different regions.

The measurement error is generally worse when looking up, although in this scenario, the background complicates matters near the limb of the Earth, as well. The best performance in this scenario is just below horizontal (90-92°). The range error in this region is less than 1% (day). As the rocket gets higher (and θ lower), performance drops rapidly. Errors exceed 5% at $\theta \simeq 85.5°$ and are near 25% by burnout. For the night cases, the same overall trend persists, but performance is much better. The total error in the absence of background is better than 1% from 87 to 92°, and remains below 10% until burnout.

This analysis was also repeated at a ranges of 200 and 400 km, also shown in Figure 6.7. At a shorter range, performance is of course much better. Here the signal from the rocket is much brighter than the background, so the difference between day and night cases is smaller. Even with background, range errors remain below 2% for the entire boost phase, and accuracy is better than 1 km for most of the trajectory. At 400km range, there is still a small region where performance is acceptable, even with background. Errors are below 5% near horizontal (91-93°), and at night, can be better than 1%. Early detection of the launch is critical at long ranges, where the region of best performance is both lower and narrower in altitude.

94
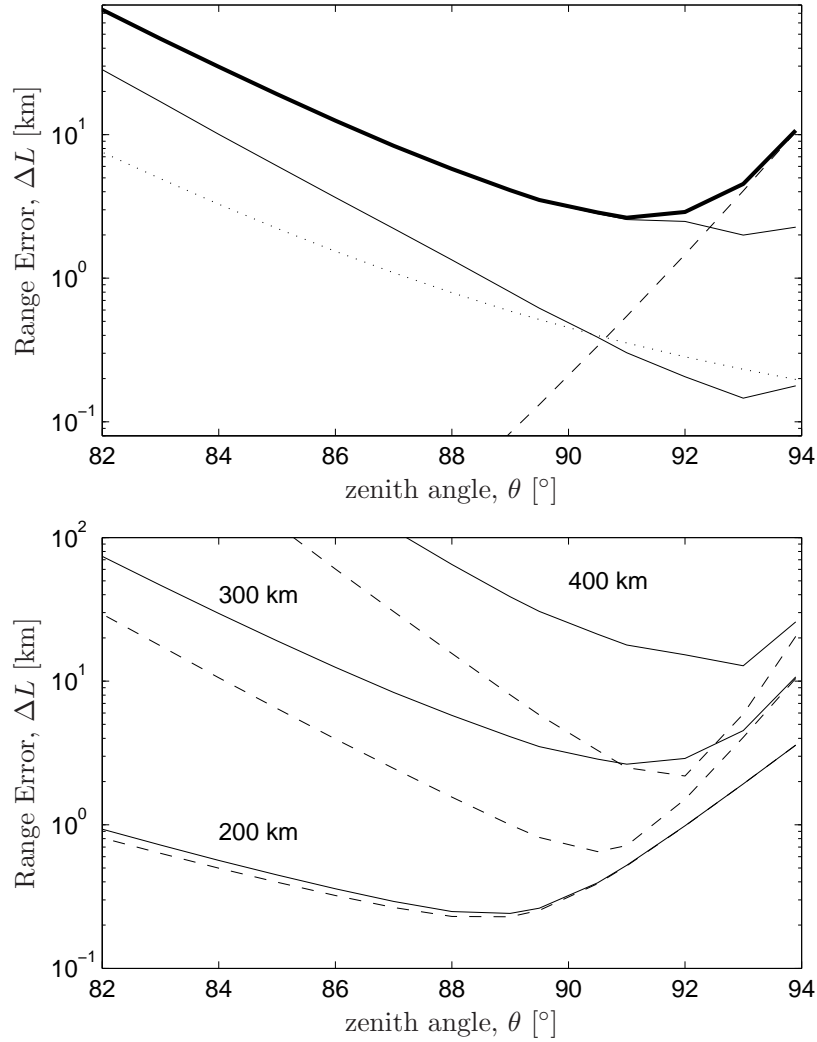
Figure 6.7:   Range Errors for ABL scenario.
Top: Errors at 300 km range. The heavy line (—) is the total error. The two solid lines (—) represent contribution from noise with and without background; dotted line (⋯) is the range error caused by a 50 μrad pointing error; dashed line (- - -) is the range error from a 5% error in concentration. *Bottom* : Comparison of total range error at 200, 300 and 400 km. Solid lines (—) are with background, dashed (- - -) are without background (night).

95

6.4   Example 2: Tactical Missile Warning Sensor

A ranging sensor could be used to augment aircraft defensive systems by providing an estimate of time-to-impact of approaching surface-to-air (SAM) or air-to-air (AAM) missiles.

It would be unrealistic to suppose a large, sophisticated spectrometer for this role. Volume and weight on tactical aircraft is precious, so the sensor must be small, and most likely very low cost, if the entire fleet is to be equipped. On the other hand, the sensor is not required to operate at long ranges. The accuracy requirements may be lower as well. For this application, bandpass filters would most likely be used in place of a spectrometer, and a staring focal plane in place of a steerable optic. Before analyzing the errors for this case, a closer look at how a filter-based system might perform is in order.

6.4.1   Estimating Range from Filter Bands.   Since the metric selected for the project is an average over the entire band, high spectral resolution may not be needed (or even helpful, for that matter). The main driver is the need to estimate the baseline from out-of-band data. A minimum of two out-of band measurements are required, although three or more would be preferred in order to use the second-order polynomial baseline as has been computed from the spectra.

Equipment difficulties prevented experimental verification of this idea, but digital filters can be applied to measured spectra as an example of the technique. To make this "simulated experiment" as realistic as possible, the measured transmission of three off-the-shelf filters (from ThorLabs) were digitally applied to actual data from the Bomem instrument. The filters are 10 nm bandpass, centered at 750, 760 and 780 nm. The 760 nm filter function is shifted toward the red by about 4 nm compared to the measured values to better match the oxygen band. This could be done experimentally by tilting the filter slightly, or a custom filter centered about 764 nm could be used. Figure 6.8 shows a sample data spectrum with these filter functions overlayed.
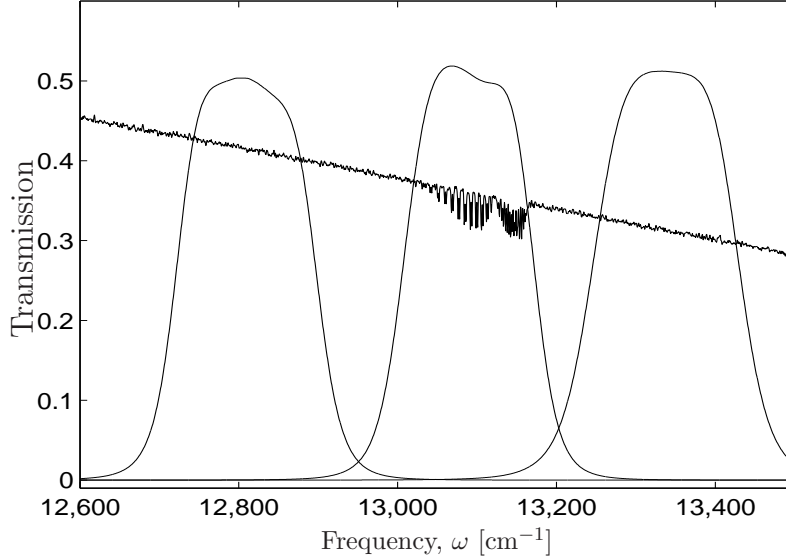
Figure 6.8: Measured spectrum (normalized to unit maximum) with filter functions overlayed. The vertical scale represents transmission, T, for the filters, or normalized intensity for the spectrum.

Applying these filter functions to the measured spectra reduces the spectrum to 3 data points, designated I_1, I_2, and I_3, for the 750, 764 and 780 nm filters, respectively. The two out-of-band filters, I_1 and I_3 are used to estimate a baseline value, I_b, at 764 nm by simply interpolating,

$$I_b = I_1 + \frac{\lambda_2 - \lambda_1}{\lambda_3 - \lambda_1}(I_3 - I_1). \tag{6.17}$$

The estimate for the band-average absorption is then

$$\bar{A} = 1 - \bar{T} = 1 - \frac{I_2}{I_b}. \tag{6.18}$$

Figure 6.9 shows the results of computing this metric from actual data and from FASCODE transmission spectra. The data are well correlated, but offset from the FASCODE predictions. This is due, at least in part, to the fact that the baseline in the data is curved, but in FASCODE, it is flat. With two out-of-band filters, there is not enough information to match the curvature of the baseline in the data, which

97
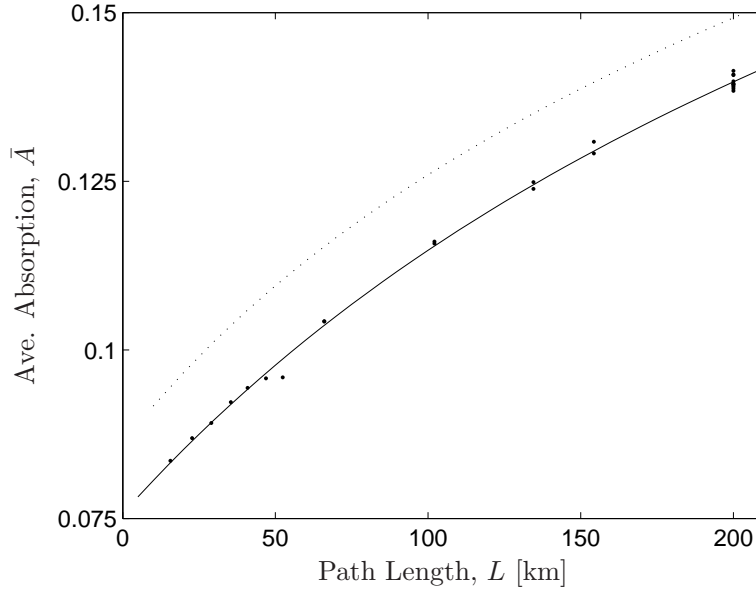
Figure 6.9: Band-average absorption estimated using the three filters shown in fig 6.8. Shows the value of absorption computed from data (·), from FASCODE spectra (···), and the best fit through the data (—). The fit function is a modified version of eqn 4.21 to account for the non-zero intercept.

introduces a systematic error. If the source, instrument and aerosol spectra are nearly constant (as they are in the data from Wright-Patterson AFB), then this offset is also nearly constant. These points can, therefore, be used to compute a calibration curve from which range can be extracted as before. This results in a range estimate (without correction for instrument path length or concentration) of 36.26±0.67 m, compared to the actual range of 36.6 m. Error is less than 1% for this simulated 3-filter instrument, although a fourth filter would be needed to attempt range extraction from FASCODE alone without historical data.

6.4.2   Missile Warning Scenario.   With these basics established, the errors for a filter-based missile warning sensor scenario can now be analyzed. For a sample engagement, assume an aircraft at an altitude of 3.5 km and a small shoulder-fired SAM launched from a site 3 km away (ground range). The slant range is about 4.5 km. Because the missile is tracking the aircraft, the zenith angle to the target is assumed

constant ($\theta = 130°$) and only the range changes throughout the engagement. Table 6.2 shows some of the other assumptions in this scenario.

Table 6.2: *Assumptions in SAM Scenario.*

Sensor:		Missile:	
altitude	3.5 km	Spectral Intensity	100 mW/str nm
FOV (full angle)	90°		
Detector array	1 Mpixel		
Aperture diam.	1 in	Scenario:	
Optical sys. throughput	60%	Ground Range	3 km
Detector quantum efficiency	70%	Max slant Range	4.5 km
Photon-noise limited	-	Background radiance	
Spectral Resolution	10 nm	mean	8 μW/cm^{2}str nm
Temporal Resolution	30 Hz		

Typical background scene radiance, according to the IR Handbook [43], is approximately 8 μW/cm^2 str nm. With this, the missile signature at launch is much less than the background, so the ranging sensor would need to be cued by a separate missile launch detector (operating in a different band). Even with background subtraction, the missile signature might be indistinguishable from random fluctuations in the background scene. In cases like this, the signal-to-background ratio (SBR) is as important as the SNR in determining overall performance. Figure 6.10 shows the SBR as a function of range for the source and background radiances given in Table 6.2. When SBR is greater than 1, detection is relatively straightforward. When SBR falls below 1, background subtraction will be necessary and detection probability cannot be estimated without some knowledge of the scene-to-scene variation in the background. More research on spectral background subtraction techniques would be required. For simplicity, the remainder of this discussion is limited to nighttime scenarios in which the background can be neglected.

Some assumptions must also be made to address other error sources. For this scenario, the pointing accuracy would be much worse than in the ABL example above. The accuracy could be no better than the sensor IFOV (the FOV seen by a single sensor in the focal plane array). In addition, there will be errors in the platform

99
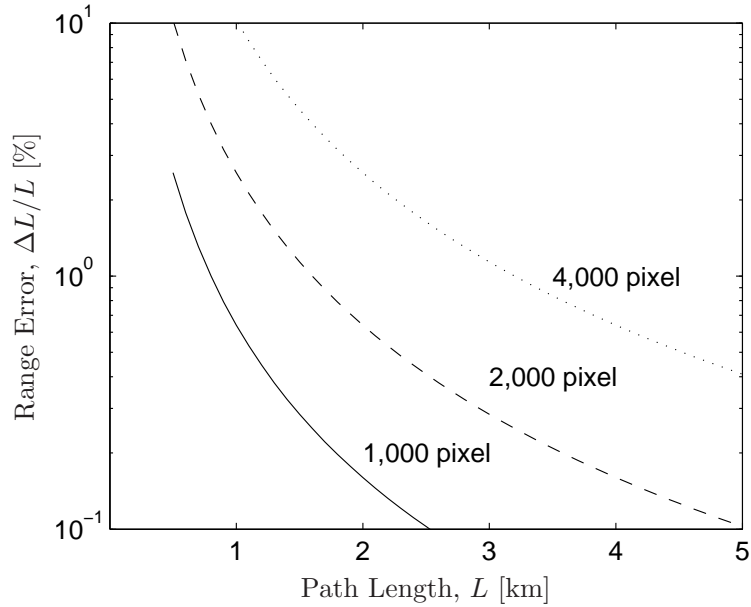
Figure 6.10:   Signal-to-background ratio for the values given in Table 6.2. Labels indicate the number of pixels (detector elements) across each dimension of the detector array. Light from the missile plume is assumed to be imaged onto a single pixel in all cases.

attitude sensors, and body flexure means the pointing angle of the sensor relative to the platform is not constant. On the other hand, the concentration errors might be much better. The aircraft will have pressure sensors on board, and variations over the short path should be minimal. Pointing error of 15 mrad and concentration error of 1% are therefore assumed.

Figure 6.11 shows the resulting overall range error. In the absence of background, accuracy better than 2% is predicted. Even for photon-noise limited detection and no background, the measurement error is still the dominant term for ranges beyond about 3 km. At short ranges, concentration errors dominate. Pointing error is inconsequential at all ranges in this scenario.

6.5   Errors Caused by Potassium Emission

In addition to the errors discussed above, there is another source of error that is only relevant when the R-branch average, $\bar{A}_R$, is used (as discussed in §4.4). Section 5.3 showed that use of $\bar{A}_R$ effectively eliminated the potassium emission from the

100
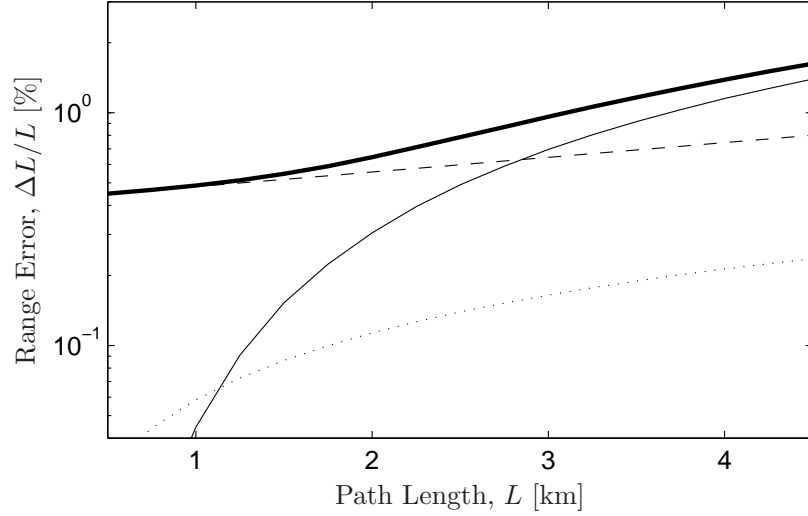
Figure 6.11:   Range Errors for SAM scenario. The heavy line (—)
is the total error; solid line (—) is contribution from noise (without
background); dotted line (···) is the error caused by a 15 mrad pointing
error; dashed line (- - -) is the error from a 1% error in concentration.

average absorption metric. This was possible because of the relatively high spectral
resolution of the data. This section will discuss the requirements for estimating range
in the presence of potassium emissions.

High spectral resolution is important for two reasons. First, it is important
to use frequencies that are far away from the potassium line. "Far" in this sense
means that the convolution of the potassium emission lineshape with the instrument
lineshape $f_I(\omega - \omega_o)$ must be near zero for all frequencies used in the average. The
potassium line closest to the R-branch peaks at about 13,044 cm^{-1}. The lower end of
the band used in $\bar{A}_R$ is 13,120.9 cm^{-1}, the band origin (the energy difference between
the J=0 levels of the two states), so the instrument response must go to zero within
75 cm^{-1}, or about 5 nm, from the peak. If filters are used in place of a spectrometer,
the same idea applies to the filter cut-off; the transmission must be near zero at
13,044 cm^{-1}. It may be helpful to add a cold potassium cell to ensure that the
transmission of the system at the potassium lines is as low as possible.

Secondly, high spectral resolution will minimize "cross-talk" between the R and
P branches. The PP(J=1) line peaks less than 3 cm^{-1} away from the integration

101
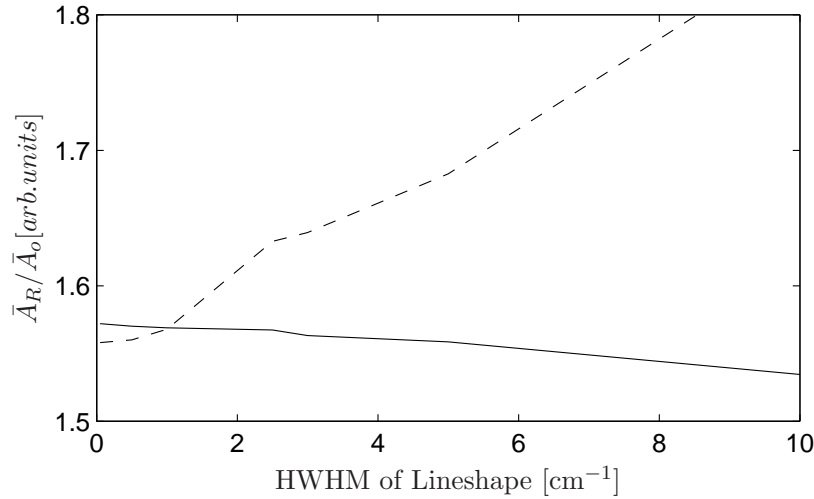
Figure 6.12: The fraction of total absorption observed in the R-branch as a function of HWHM of the instrument lineshape. The solid line (——) is for a triangular lineshape; dashed line (- - -) is for a sinc^2 lineshape. The numerical value of this ratio depends on the choice of bounds for each integral, so only the relative trend is significant.

band cutoff of 13,120.9 cm^{-1}. Unless the instrument lineshape is negligible 3 cm^{-1} (or about 0.2 nm) away from line center, some of the P-branch absorption, when convolved by the instrument lineshape, will fall within the bounds of the integral. Likewise, some of the absorption from the R-branches will fall outside the integration band. Because the lines are much closer together in the R-branch, the loss from R will be greater than the gain from P. This effect will be included in the model results only if the instrument lineshape function used by FASCODE (the spectrum is computed monochromatically then convolved by a lineshape) is a good match to the actual instrument lineshape. This effect is demonstrated in Figure 6.12. This plot shows the fraction of the total band absorption that is observed in the R branch as a function of resolution for two different lineshapes. The triangle function has finite support, meaning all the energy is contained within a finite band. The sinc^2 function never truly goes to zero, so the branch cross-talk effect is much stronger. This effect will be very difficult to remove with filters, but with sharp cutoff filters and proper calibration, the effects may be manageable.

102

While these resolution issues can be an important design consideration, the preceding sections of this chapter showed that measurement error is often the main source of range error. For applications where the target is not expected to contain potassium, maximizing SNR and minimizing background will be the primary factors in design. With these factors in mind, the best estimates based on actual short-range performance, theory and modelling indicate that range errors can be kept small at long range.

6.6 Summary

This chapter shows passive ranging has potential for use in real operational applications. For example, range error is projected to remain below 5% at ranges up to 400 km against TBM targets. This chapter also establishes relationships for the sensitivity of range error to SNR, range error to errors in $\bar{A}$, and range error to range. These relationships can be used to predict the performance of any sensor, not just the Bomem instrument used in this project. In so doing, this chapter also presents a conceptual filter system that could be small, light, and inexpensive with only minor performance penalties compared to large, complex spectrometers.

VII. Conclusion

The relationship between atmospheric transmission and range is well known and documented, yet previous attempts to exploit this for passive ranging have been unable to produce consistently accurate results. By monitoring absorption in a different band and applying different analysis techniques than previous works, this project has demonstrated the feasibility of passive sensors for measuring range to an emissive target, with experimental range error below 1%.

This research has shown that measurements of absorption in the oxygen band near 762 nm offer a robust metric from which range can be accurately estimated. This band is spectrally isolated from other absorbing species. Section 2.4.1 shows that this isolation enables direct estimation of oxygen absorption. When the molecular absorption is averaged over the entire band, the average value, $\bar{A}$, is independent of the rotational distribution of absorbing states. Experimental results confirm this metric is also independent of source and instrument spectral characteristics. Analysis also indicates the results should also be independent of aerosol scattering, although this hypothesis could not be confirmed experimentally over the short distances available.

Chapter V demonstrates range can be estimated by comparing observed values of $\bar{A}$ to metric curves, ($\bar{A}$ as a function of range). These curves are prepared by fitting an equation to either historical data or model-predicted transmission spectra, where the fit equation is derived from established band models. This is the first time a non-Beer's Law method has been applied to range estimation, and Chapter VI shows this approach reduces range errors by about a factor of three on average. Over 30 different band models (and Beer's Law) are compared numerically, and the Random Band Model (equation (4.21)) is found to most accurately represent the O_2 (X→b) band.

The band models, as expressed in the literature, relate average absorption to concentration length. This paper presents a unique extension to these models which allows absorption to be computed as a function of range, even for an inhomogeneous

104

path. Chapter IV shows that use of this technique allows the band models to more closely describe the behavior of curves of $\bar{A}$ as a function of range (in experimental data and in results computed by FASCODE), which in turn improves range accuracy. This improvement reduces range error by 60% in short-range experiments.

Range accuracy better than 1% has been demonstrated in short-range (under 3 km) field experiments with a representative target. Logistics limited field experiments to ranges under 3 km. The metric curve for this experiment was based on FASCODE predictions for a standard atmosphere. A simple correction was developed to adjust for conditions without requiring detailed atmospheric profiles. The limiting factor in accuracy of field experiments appeared to be measurement error, although a small systematic error was also evident when a large number of trials were averaged.

Chapter VI uses theory and modelling to project expected accuracy at longer ranges. Measurement error and background radiance (scattered sunlight) remain the limiting factors in many cases simulated. Analysis indicates 5% accuracy is possible at ranges exceeding 400 km. In the absence of background (e.g. at night) or at shorter ranges, accuracy can be much better. Accuracy is expected to be best when air pressure at the target is high. Errors in pointing and measurements of air concentration can also be factors.

Chapter VI also presents an instrument concept based on band-pass filters that offers a significant reduction in size, weight and cost compared to a conventional spectrometer, with a minimal loss in accuracy. In the lamp experiments, for example, range error was actually lower in estimates based on digitally applying filters to measured spectra.

7.1 Design Recommendations

Two notional instrument concepts (for two very different applications) are put forth as examples in Chapter VI. Because the metric of choice is the average over the entire absorption band, resolution is not a primary consideration for instrument

105

selection. For many applications, noise and/or background radiance are the limiting factors in range accuracy. For these cases, instruments should be selected for high throughput, low noise, high quantum efficiency and narrow field of view.

The one caveat to this rule is for applications in which the target can be expected to contain potassium (such as solid rocket motors and many types of explosives). The potassium emission line at the red end of the absorption band can be spectrally isolated if the instrument has sufficient resolution. Specifically, the instrument lineshape must be negligible for frequencies more than 75 cm^{-1} (or about 5 nm) away from the peak.

7.2 Future Work

There are several areas that merit further research. First, a closer examination of bandpass filters (as discussed in section 6.4) for ranging should be conducted. This project should include investigation of alternate analysis techniques and/or use of more filters; selection of filter bands (which will be particularly important for applications with potassium emission from the source); and experimental verification.

Second, a more detailed analysis of scattered sunlight (path radiance) and spectral background subtraction techniques should be conducted. For example, there are other spectral features (outside the O_2 band) that might enable independent estimation of the contribution from sunlight. Also, the solar background has an apparent range. By studying how that apparent range varies with regard to factors like time and azimuth, it may be possible to predict the background contribution and apply a simple correction. Methods for dealing with sky and surface backgrounds may differ enough to merit separate research efforts.

Third, the $(v'' = 0) \rightarrow (v' = 1)$ band offers some advantages not fully explored here. The 0→0 band was the primary choice because source signatures are brighter in that region. On the other hand, the 0→1 band does not suffer from potassium emission. Many spectrometers can easily measure both bands simultaneously, so the

106

use of both bands together may enable more accurate range estimation than either band alone.

This project focused on estimation of range from a single observation. An investigation of more sophisticated methods may be worthwhile. For example, real missiles follow trajectories that are constrained by the laws of mechanics. Perhaps a Bayesian estimation approach or Kalman filters could make use of this *a priori* information to produce a better estimate than the simple average used here.

A more detailed analysis of how variations in concentration along the path affect the result may allow some refinements in the technique presented here. Use of a single concentration value to represent an average or effective concentration is a useful and valid approximation. A more exact approach may improve accuracy for long range applications.

Lastly, development of a real-time or near-real time algorithm may be desirable for some applications, such as missile warning. One possible method to speed processing in this technique is to predict the metric curves from the engagement geometry without any use of historical data or FASCODE at all. The best fit parameters for the fitting function are smooth and predictable functions of zenith angle and sensor altitude, and they also depend weakly on atmospheric conditions. This approach should be explored further to assess the loss in accuracy.

Appendix A. Band Model Derivations

$\mathcal{S}$everal band models were presented and compared in chapter IV. This chapter provides more detail on the derivation of a few key models that are either important to the results presented in the main text or for which the derivations are enlightening.

The derivations begin as before by defining the following:

$$x = \frac{\omega}{\delta} \qquad y = \frac{\alpha}{\delta} \qquad u = \frac{Sm}{2\pi\alpha}, \qquad \text{[2.22]}$$

where α is the linewidth, δ is the line spacing, S is the peak linestrength and m is the concentration length, $m = \int_0^L N(\ell)d\ell$.

A.1 Elsasser Band Model

The Elsasser band model [11,17,43] is derived by treating the band as a uniformly-spaced array of equal strength Lorentzian lines.

For a single Lorentzian line, the absorption cross-section is

$$\sigma(\omega) = Sf(\omega - \omega_o) = \frac{4\pi S\alpha}{\omega^2 + \alpha^2}. \qquad (A.1)$$

For real transitions, S is subject to the constraint $\int Sf(\omega)d\omega = h\nu B_{ij}/c$, where B is the Einstein coefficient. For the Elsasser model, the strength of the lines in the equivalent uniform array of lines will be treated as a free parameter that will be fit to the data.

For a uniform array of Lorentzian lines the monochromatic cross-section is then

$$\sigma_\omega = \sum_{k=-\infty}^{\infty} S\frac{4\pi\alpha}{(\omega - k\delta)^2 + \alpha^2} \qquad (A.2)$$

or

$$m\sigma_x = \sum_{k=-\infty}^{\infty} \frac{2uy^2}{(x-k)^2 + y^2} = 2uy^2 \sum_{k=-\infty}^{\infty} f(k). \qquad (A.3)$$

108

According to the Poisson Sum Rule, $f(k)$ can be replace with its Fourier transform, $F(\kappa)$, because

$$\sum_{k=-\infty}^{\infty} f(k) = \sum_{\kappa=-\infty}^{\infty} F(\kappa). \tag{A.4}$$

The transform of f is

$$F(\kappa) = \frac{\pi}{y} \exp\left[2\pi \left(ix\kappa - y|\kappa|\right)\right], \tag{A.5}$$

so

$$\begin{aligned}
m\sigma_x &= 2\pi uy \left[\sum_{\kappa=-\infty}^{-1} e^{2\pi\kappa(ix+y)} + 1 + \sum_{\kappa=1}^{\infty} e^{2\pi\kappa(ix-y)}\right] \tag{A.6} \\
&= 2\pi uy \left[1 + 2\sum_{\kappa=1}^{\infty} e^{-2\pi\kappa y} \cos(2\pi\kappa x)\right].
\end{aligned}$$

This can be simplified with the following identity from Gradshteyn and Ryzhik [18],

$$1 + 2\sum_{k=1}^{\infty} e^{-kt} \cos(kx) = \frac{\sinh t}{\cosh t - \cos x}, \tag{A.7}$$

which gives

$$m\sigma_x = 2\pi uy \frac{\sinh(2\pi y)}{\cosh(2\pi y) - \cos(2\pi x)}. \tag{A.8}$$

So the absorption, averaged over some finite bandwidth centered about ω is,

$$\begin{aligned}
\overline{A}(\omega) &\equiv 1 - \overline{T}(\omega) = \frac{1}{\delta} \int_{-\infty}^{\infty} 1 - \exp(-\sigma_\omega m) d\omega = 1 - \int_{-\frac{1}{2}}^{\frac{1}{2}} \exp(-\sigma_x m) dx \\
&= 1 - E(u, y) = 1 - \int_{-\frac{1}{2}}^{\frac{1}{2}} \exp\left(\frac{-2\pi uy \sinh(2\pi y)}{\cosh(2\pi y) - \cos(2\pi x)}\right) dx. \tag{A.9}
\end{aligned}$$

Here, $E(u, y)$ is known as the Elsasser function. The assumed periodicity has been used to change the bounds of integration; the average over all frequencies will be the same as the average over one period of the array.

Notice that in the limit of completely overlapping lines, the linewidth is much greater than the line spacing ($y \gg 1$). For large y, $\sinh(2\pi y)$ and $\cosh(2\pi y)$ approach

109

infinity, so

$$\lim_{y\to\infty} E(u,y) = \int_{-1/2}^{+1/2} \exp(-2\pi uy)dx = \exp(-2\pi uy) = \exp(-Sm/\delta). \qquad (A.10)$$

Under these circumstances, where the lines completely overlap, the cross-section is now slowly varying and the band-average transmission behaves like a simple exponential, as predicted by Beer's Law.

This raises an interesting question about the use of Beer's Law to describe the filter-band ratios in MPR. To assess this, the HITRAN database [40,41] was examined for lines in the vicinity of the filters defined by Jeffrey [23]. In a region ± 2 cm^{-1} about the first filter wavelength, HITRAN has 879 lines (only 454 of which are CO_2 lines) for an average spacing of 0.0045 cm^{-1}. At sea-level, the average linewidth is 0.076 cm^{-1}, for $y = 15$. This would probably be sufficient for Beer's Law to apply. However, most of these lines in the database are for absorption from states that are not thermally populated. If only lines with a lower state energy $< 3kT$ are used, the number of lines drops to 142 (only 12 of which are CO_2). Furthermore, for the altitudes discussed in that paper the average linewidth drops to less than 0.01 cm^{-1}. Under these conditions, $y < 1$. Results for the other filter band are similar.

A.1.1 Non-Overlapping Line Limit. There is some disagreement in the literature over the correct form for this limit, as well as the conditions under which it applies. This section discusses the solution presented by Goody & Yung [17]. Alternate equations are also available in references [22,35,43].

For lines that are well separated, the mean spacing, δ, will be much greater than the width, α, so $y \ll 1$. In this case,

$$\sinh 2\pi y \simeq 2\pi y \qquad \cosh 2\pi y \simeq 1. \qquad (A.11)$$

110

In the strong-line limit ($u \gg 1$) this allows the Elsasser function to be written [17] as

$$E(u, y) = 1 - \frac{2}{\sqrt{\pi}} \int_0^{\pi y \sqrt{2u}} \exp(-\xi^2) d\xi. \tag{A.12}$$

So

$$\bar{A} = \mathrm{erf}\left[\pi y \sqrt{2u}\right]. \tag{A.13}$$

Two things are apparent in the limit as $y \to 0$ (spacing $\gg$ width). First, the argument of the error function above must also be very small. Series expansion of erf can be used to write the inverse function for small arguments,

$$\mathrm{erf}^{-1} \bar{A} \simeq \frac{\sqrt{\pi}}{2} \bar{A}. \tag{A.14}$$

Secondly, as $y \to 0$, an Elsasser band must approach an isolated Lorentzian as given by equation 2.23. Putting these together gives

$$\mathrm{erf}^{-1} \bar{A} = \pi^{3/2} y \mathcal{L}(u), \tag{A.15}$$

or

$$\bar{A} = \mathrm{erf}\left[\pi^{3/2} y \mathcal{L}(u)\right]. \tag{A.16}$$

This development makes some assumptions that are not obviously valid. Primarily, this uses of the strong line limit to introduce the error function and then assumes that $\bar{A}$ must be small in order to invert the erf, even though strong-line implies that $\bar{A}$ is not small. In spite of this, the approximation matches the exact solution quite well, as was seen in section 4.3.1. For the small values of y found in atmospheric oxygen ($y < 0.05$), this approximation is accurate (compared to equation 2.26) to better than 1%.

A.2   Random Models

For a line centered at some frequency ω_i, the transmission at frequency ω is

$$T_\omega = \exp\left(-m\sigma(\omega_i)\right), \tag{A.17}$$

If this line is randomly located anywhere in a band of width δ with equal probability, then a probability distribution function can be used to describe the probability of finding a line at frequency ω, or

$$P(\omega) = \begin{cases} 1/\delta, & |\omega| < \delta/2; \\ 0, & \text{otherwise.} \end{cases} \tag{A.18}$$

The probability of finding the line within a given interval of width $d\omega$ is, therefore, $d\omega/\delta$. The expectation value of transmission for that band is then

$$[T] = \frac{\int_\delta P(\omega)T_\omega d\omega}{\int_\delta P(\omega)d\omega} = \frac{1}{\delta}\int_\delta T_\omega d\omega = \bar{T} \tag{A.19}$$

which is equivalent to the band average transmission for a single line at the center of the band.

For a collection of n lines randomly located within a band of width $n\delta$, the probability of finding any one line on an interval $d\omega$ is still $d\omega/\delta$. The transmission of the collection is simply the product of the transmissions from each individual line, so all lines are assumed independent, equal strength and uniformly distributed, then

$$\begin{aligned} \bar{T} &= \frac{\prod_{i=1}^n \int_{n\delta}(1/\delta)T_\omega d\omega}{\prod_{i=1}^n \int_{n\delta}(1/\delta)d\omega} \\ &= \left[\frac{1}{n\delta}\int_{n\delta}\exp(-m\sigma_\omega)d\omega\right]^n \\ &= \left\{1 - \frac{1}{n\delta}\int_{n\delta}1 - \exp(-m\sigma_\omega)d\omega\right\}^n. \end{aligned} \tag{A.20}$$

112

Recall that for large n,

$$\lim_{n \to \infty} [1 - (x/n)]^n = e^{-x}. \qquad (A.21)$$

Which means that for a sufficiently large number of lines,

$$\bar{T} = \exp\left[-\frac{1}{\delta} \int_{-\infty}^{\infty} 1 - \exp(-m\sigma_\omega) d\omega\right] = \exp\left[1 - \bar{T}(\text{single line})\right]. \qquad (A.22)$$

And the absorption is then

$$\bar{A} = 1 - \bar{T} = 1 - \exp(\bar{A}(\text{single line})). \qquad (A.23)$$

The derivation for a random collection of uniform (Elsasser) bands proceeds along similar lines. Let $\bar{T}(n)$ denote the average transmission for a collection n uniform bands and $\bar{T}_i$ the average transmission of the ith band alone. If all bands are constrained to have the same strength and average spacing (*i.e.* only the relative position of each array is random), then

$$\bar{T}(n) = \prod \bar{T}_i = \left[1 - \bar{A}\right]^n. \qquad (A.24)$$

In the limit of large n, this produces the same result as before, and for $n=1$ this is simply the Elsasser band.

This generalized model is valid for any value of n. Examination of the structure of the $O_2(b \leftarrow X)$ band suggests using $n = 4$ (for the PP, QP, RR and QR branches discussed in section 2.1, or possibly $n = 8$ to include the isotope lines. Fits were attempted letting n be an adjustable fit parameter to test this idea. Optimal values of n ranged from 1 to 40 and, like all the other parameters, depended most strongly on θ.

113

Appendix B. Computing Oxygen Content from Meteorology Data

To use estimate absorption, one must first know the number of absorbers in the path. The basis for this is the Ideal Gas Law, where pressure and temperature can be obtained from meteorological observations. This data is available from a variety of sources, including the Air Force Weather Agency (afweather.afwa.af.mil), the National Center for Atmospheric Research (www.rap.ucar.edu/weather/surface/), and the Air Force Combat Climatology Center (www.afccc.af.mil). Meteorology data is most often presented in METAR format. A sample observation is shown below in Table B.1

Table B.1:   *METAR Data Sample*

KFFO 162259Z 12002KT 7SM FEW040 SCT120 OVC260 25/20 A2995 RMK SLP139		
Field	**Meaning**	**Value in this example**
1	Station ID Code	KFFO = Wright-Patterson (Area C)
2	Date/Time	162259Z $\Rightarrow$ 16th day of the month 2259 Zulu Time (=6:59pm EST)
3	Wind Speed/Dir.	12002KT = wind speed of 2 knots from compass heading of 120°
4	Visibility	7SM = 7 statute miles
5-7	Cloud Data	note: uses a variable number of fields (all fields between visibility and temperature)
8	Temp./Dew Point	25/20 $\Rightarrow$ Temp = 25^oC, DewPoint=20^oC
9	Altimeter	A2995 = 29.95 inches of Hg
10	Remarks	in this case remarks are used to give sea-level pressure SLP139 = 1013.9hPa (=1013.9mbar)

B.1   Pressure

Here, pressure is presented in two different formats: altimeter and sea-level pressure. Both are estimates of an equivalent sea-level pressure calculated from the observed or station pressure. The difference between the two numbers lies in the calculation process and the assumptions about how pressure scales with altitude. Sea-level pressure is a more sophisticated estimate, but for this project, altimeter will be more straightforward to use with no loss in accuracy. Altimeter is calculated

114

from station pressure and elevation assuming the pressure scales according the US Standard Atmosphere rules discussed in section 2.2.

For the altitudes of interest here, a simple exponential scaling is an adequate approximation of the detailed scaling rules in §2.2. Station pressure at altitude z is then

$$P(z) = P_o \exp\left[-\frac{a_o z}{t_{\text{std}}}\right] \tag{B.1}$$

where P_o is the sea-level pressure (Altimeter value) and a_o=34.18 K/km. Rather than using observed temperature in Equation B.1, the standard temperature at elevation z, which is given by

$$t_{\text{std}}(z) = t_o + \varphi z = 288K - (6.5K/km)z., \tag{B.2}$$

is used.

Experiments are often conducted at a different location than the meteorology observations, so the station pressure is used to find the conditions at the experiment site. For an experiment at elevation z and meteorology data taken at elevation z_m, the local pressure is,

$$P(z) = P(z_m) \exp\left[-a_o\left(\frac{z}{t_{\text{std}}(z)} - \frac{z_m}{t_{\text{std}}(z_m)}\right)\right], \tag{B.3}$$

where Equation B.2 can be used to estimate $t(z)$.

B.2 Water Content

The mixing fraction of O_2 is well known and constant at about 20.95%, but this is a fraction of the *dry* air. Observations must first be corrected for the water content before applying the mixing fraction.

First, the vapor pressure of water, p, (in units of Pascals) is given by

$$\log_{10} p = -7.90298(\tau - 1) + 5.02808\log_{10}\tau - 1.3816 \times 10^{-7}\left(10^{11.344(1-1/\tau)} - 1\right)$$
$$+ 8.1328 \times 10^{-3}\left(10^{-3.4915(\tau-1)} - 1\right) + 5.00571, \tag{B.4}$$

where

$$\tau = \frac{373.16K}{\text{Dew Point [in K]}}. \tag{B.5}$$

The vapor pressure can then be used to find the specific humidity, q and a virtual temperature t_v.

$$q = \frac{0.622p}{P - 0.378p} \tag{B.6}$$
$$t_v = (1 + 0.61q)t, \tag{B.7}$$

where pressure, P must again be in Pascals. The virtual temperature is used in the Ideal Gas Law to find the number density of air molecules.

$$n_{\text{air}} \equiv \frac{N_{\text{air}}}{V} = \frac{P}{kt_v}, \tag{B.8}$$

where N is a number of molecules and n is number density. The number density of *dry* air is then

$$n_{\text{dry}} = n_{\text{air}}(1 - q). \tag{B.9}$$

So the number density of Oxygen molecules is

$$n_{\text{O2}} = 0.2095n_{\text{dry}} = 0.2095n_{\text{air}}(1 - q) \tag{B.10}$$
$$= 00295\frac{P}{kt_v}(1 - q).$$

116

Bibliography

1. Anderson, Gail P. "Lambert's Law", Nov 2004. Private Conversation.

2. Babcock, Harold D. and Luise Herzberg. "Fine Structure of the red system of atmospheric oxygen bands". *Astrophysical Journal*, 108:167–190, May 1948.

3. Baker, William. "Incomplete Gamma Function", Jun 2005. Private Conversation.

4. Barniv, Y. "Passive ranging using image expansion". *IEEE Transactions on Aerospace and Electronic Systems*, 31, no.1:358–374, Jan 1995.

5. Bronson, Richard. *Schaum's Outline of Theory and Problems of Differential Equations, 2ed.* McGraw-Hill, New York, 1994.

6. Bulychev, Y. G., S. E. Gordeev, and A. P. Manin. "Estimating the motion parameters of a target on the basis of incomplete measurements". *Radio and Communications Technology*, 5, no.12:17–24, 2000.

7. Burch, Darrell E., David A. Gryvnak, and Dudley Williams. "Total Absorptance of Carbon Dioxide in the Infrared". *Applied Optics*, 1, no.6:759–765, Nov 1962.

8. Chuang, C. K., M. R. Wohlers, J.S. Draper, H. Evans, R. Cody, and D. Sene. "MPR Error Budger Analysis for Air or Space-borne Missile Surveillance". *IRIS MD-SEA*. Jan 1999.

9. Draper, James S., Sumner Perlman, C. K. Chuang, Matt Hanson, Larry Lillard, Brian Hibbeln, and Darren Sene. "Tracking and Identification of Distant Missiles by Remote Sounding". *IEEE Aerospace Applications Conference; Proceedings of*, 333–341, vol.4. 6-13 Mar 1999.

10. Dubin, Maurice, Arnold R. Hull, and K. S. W. Champion (editors). *U.S. Standard Atmosphere, 1976.* National Oceanographic and Atmospheric Adminsitration (NOAA), Washington D.C., 1976.

11. Elsasser, Walter M. "Mean absorption and equivalent absorption coefficient of a band spectrum". *Physical Review*, 54:126, Jul 1938.

12. Evans, Howard E. and Brian A. Hibbeln. "The Theory of Single Sensor Altitude Determination". *IEEE Aerospace Applications Conference; Proceedings of, vol 4*, 53–65, vol.3. 6-13 Mar 1996.

13. Gat, N., K. Lee, and G. R. Scriven. *Advanced Monocular Passive Ranging.* Contract AFRL-PR-ED-TR-2003-0001, Air Force Research lab, Lexington, Massachusetts, TBD 2003.

14. Gibson, D M, J D Allen, and A Kuyper. "Range Estimation by Differential Atmospheric Refraction (REDAR)". *MSS MD-SEA Conference Proceedings*. Nov 2003.

15. Goldfain, E. "Curvature Sensing from a single defocused image in partially coherent light". *Proceedings of the SPIE, vol 3430*, 114–125. Jul 1998.

16. Goody, R.M. "A note on the regular model of an absorption band". *Quarterly Journal of the Royal Meteorological Society*, 87:428–430, 1961.

17. Goody, R.M. and Y.L. Yung. *Atmospheric Radiation: Theoretical Basis, 2ed.* Oxford University Press, New York, 1989.

18. Gradshteyn, I.S. and I.M. Ryzhik. *Tables of Integrals, Series and Products, 5ed.* Academic Press, Inc., Boston, 1994.

19. Gregoris, Dennis J. "Passive ranging technique for infrared search and track (IRST) systems". United States Patent, Jan 1994. U.S. Patent No. 5,282,013.

20. Hasson, Victor H. and Christopher R. Dupuis. "Passive ranging through the Earth's atmosphere". *Proceedings of the SPIE, Vol 4538*, 49–56. 2002.

21. Herzberg, Gerhard. *Molecular Spectra and Molecular Structure, vol I: Spectra of Diatomic Molecules.* Van Nostrand Reinhold, New York, 1998.

22. Jamieson, John J., Raymond H. McFee, Gilbert N. Plass, Robert H. Grube, and Robert G. Richards. *Infrared Physics and Engineering.* McGraw-Hill Book Company, Inc., New York, 1963.

23. Jeffrey, William, James S. Draper, and Richard Gobel. "Monocular Passive Ranging". *IRIS Targets, Backgrounds and Discrimination*, 113–130. 5-7 Apr 1994.

24. Jursa, Adolph S. (editor). *Handbook of Geophysics and the Space Environment.* Air Force Geophysics Laboratory, Hanscom, MA, 1985.

25. Kayaalp, A. E. and J. L. Eckman. "A pipeline architecture for near real-time stereo range detection". *Proceedings of the SPIE*, 279–286. Nov 1989.

26. Kirbarajan, T., Y. Bar-Shalom, and Y. Wang. "Passive ranging of a low observable ballistic missie in a gravitational field". *IEEE Transactions on Aerospace and Electronic Systems*, 37, no.2:481–494, Apr 2001.

27. Kneizys, F.X., G.P.Andersen, E.P. Shettle, W.O. Gallery, L.W. Abreu, J.E.A. Selby, J.H. Chetwynd, and S.A. Clough. *Users Guide to LOWTRAN 7.* Research Papers AFGL-TR-88-0177, Air Force Geophysics lab, Hanscom AFB, Massachusetts, Aug 1988.

28. Ladenburg, R. and F. Reiche. "Über selektive Absorption". *Ann. Physik*, 42, no 181, 1911.

29. Leonpacher, Norman K. *Passive Infrared Ranging.* Master's thesis, Graduate School of Engineering, Air Force Institute of Technology, Wright-Patterson AFB OH, December 1983. AFIT/GEP/PH/83D-5.

30. Mckay, D L, R Wohlers, C K Chuang, J S Draper, and J Walker. "Tracking and identification of distant missiles by remote sounding". *Proceedings of the SPIE, vol 3698*, 491–500. 5-9 Apr 1999.

118

31. McKay, Dennis L., Ronald Wohlers, James S. Draper, Joseph Shanks, and James Walker. "Monocular Passive Ranging Validation with HALO/IRIS Data". *MSS MD-SEA; Proceedings of*, 171–189. Jan 2000.

32. Perlman, Sumner, C.K. Chuang, James S. Draper, E.M. Powers, D.S. Frankel, Howard E. Evans, Larry Lilliard, and Brian A. Hibbeln. "Passive Ranging for Detection, Identification, Tracking and Launch Location of Boost-Phase TBMs". *IRIS Passive Sensors Conference*, 281–299. 12-14 Mar 1996.

33. Petty, Grant W. *A Firts Course in Atmospheric Radiation*. Sundog Publishing, Madison, WI, 2004.

34. Pieper, R. J., A. W. Cooper, and G. Pelegris. "Passive range estimation using dual-baseline triangulation". *Optical Engineering*, 35, no.5:685–692, Mar 1996.

35. Plass, Gilbert N. "Models for Spectral Band Absorption". *Journal of the Optical Society of America*, 58:690–703, Nov 1958.

36. Plass, Gilbert N. "Useful representations for measurements of spectral band absorption". *Journal of the Optical Society of America*, 50, no.9:868, Sep 1960.

37. Pope, Robert S. *Collisional effects in the absorption spectra of the oxygen A band and nitric oxide fundamental band*. Ph.D. thesis, Graduate School of Engineering, Air Force Institute of Technology, Wright-Patterson AFB OH, December 1998. AFIT/DS/ENP/98-03.

38. Qian, Z. "Passive ranging method for IRST systems". *Journal of Infrared and Millimeter Waves*, 20, no.4:311–314, Aug 2001.

39. Restorff, J. B. *Passive Ranging Using Multi-Color Infrared Detectors*. Technical Report NSWC-TR-81-401, Naval Surface Weapons Center, Dahlgren, VA, Oct.

40. Rothman, L. S. and et al. "The HITRAN Molecular Spectroscopic Database and HAWKS (HITRAN Atmospheric Workstation): 1996 Edition". *J. Quant. Spectrosc. Radiat. Transfer*, 60, no.5:665–710, Mar 1998.

41. Rothman, L. S. and et al. "The HITRAN 2004 molecular spectroscopic database". *J. Quant. Spectrosc. Radiat. Transfer*, 96, no.2:139–204, Dec 2005.

42. Snell, H. E., W. O. Gallery, J.L.Moncet, and C.P. Sarkisian. *FASCODE For the Environment, Scientific Report No 3*. Contract AFRL-VS-TR-2001-1603, Air Force Research lab, Lexington, Massachusetts, Nov 2000.

43. Wolfe, William L. and George J. Zissis (editors). *The Infrared Handbook*. Office of Naval Research, Department of the Navy, Washington D.C., 1978.

REPORT DOCUMENTATION PAGE

Form Approved
OMB No. 0704–0188

1. REPORT DATE *(DD–MM–YYYY)*	2. REPORT TYPE	3. DATES COVERED *(From — To)*
19-01-2006	Doctoral Dissertation	Sept 2003— Jan 2006

4. TITLE AND SUBTITLE

Passive Ranging Using Atmospheric
Oxygen Absorption Spectra

5a. CONTRACT NUMBER

5b. GRANT NUMBER

5c. PROGRAM ELEMENT NUMBER

6. AUTHOR(S)

HAWKS, Michael R., Major, USAF

5d. PROJECT NUMBER

5e. TASK NUMBER

5f. WORK UNIT NUMBER

7. PERFORMING ORGANIZATION NAME(S) AND ADDRESS(ES)

Air Force Institute of Technology
Graduate School of Engineering and Management
2950 Hobson Way
WPAFB OH 45433-7765

8. PERFORMING ORGANIZATION REPORT NUMBER

AFIT/DS/ENP/06-02

9. SPONSORING / MONITORING AGENCY NAME(S) AND ADDRESS(ES)

John Florio
NASIC/DEM
4180 Watson Way
Wright-Patterson Air Force Base, OH 45433

10. SPONSOR/MONITOR'S ACRONYM(S)

11. SPONSOR/MONITOR'S REPORT NUMBER(S)

12. DISTRIBUTION / AVAILABILITY STATEMENT

Approved for public release; distribution is unlimited.

13. SUPPLEMENTARY NOTES

14. ABSTRACT

The depth of absorption bands in observed spectra of distant, bright sources can be used to estimate range to the source. A novel approach is presented and demonstrated using observations of the oxygen absorption band near 762 nm. Range is estimated by comparing observed values of band-average absorption against curves derived from either historical data or model predictions. Curves are based on fitting a random band model to the data, which reduces average range error by 67% compared to the Beer's Law model used in previous work. A new modification to existing band models for long, inhomogeneous paths is presented and shown to reduces error 50% in short-range experiments. A static rocket motor test was observed using a Fourier transform spectrometer at a range of 2.8 km. The range estimated from this data was accurate to within 0.5% (14 m). Similar accuracy was also achieved at shorter ranges using a lamp as a surrogate target. Long-range performance is predicted by using FASCODE and theoretical models to extrapolate observed short-range performance. Range error of 5% or less is predicted at ranges up to 400 km for a representative target.

15. SUBJECT TERMS

passive sensors, atmospheric absorption, oxygen spectroscopy, remote sensing, applied spectroscopy, band model

16. SECURITY CLASSIFICATION OF:

a. REPORT	b. ABSTRACT	c. THIS PAGE	17. LIMITATION OF ABSTRACT	18. NUMBER OF PAGES	19a. NAME OF RESPONSIBLE PERSON
U	U	U	UU	135	Dr. Glen P. Perram

19b. TELEPHONE NUMBER *(include area code)*
(937) 255-3636, ext 4504

Standard Form 298 (Rev. 8–98)
Prescribed by ANSI Std. Z39.18